AN AUTOMATED SHRINKAGE COMPENSATION METHOD FOR THE HOLES FABRICATED VIA FFF PROCESS

A THESIS SUBMITTED TO
THE GRADUATE SCHOOL OF NATURAL AND APPLIED SCIENCES
OF
MIDDLE EAST TECHNICAL UNIVERSITY

BY

SARDAR VAYGHANNEZHAD

IN PARTIAL FULFILLMENT OF THE REQUIREMENTS
FOR
THE DEGREE OF MASTER OF SCIENCE
IN
MECHANICAL ENGINEERING

SEPTEMBER 2019

Approval of the thesis:

AN AUTOMATED SHRINKAGE COMPENSATION METHOD FOR THE HOLES FABRICATED VIA FFF PROCESS

submitted by **SARDAR VAYGHANNEZHAD** in partial fulfillment of the requirements for the degree of **Master of Science in Mechanical Engineering Department, Middle East Technical University** by,

Prof. Dr. Halil Kalıpçılar
Dean, Graduate School of **Natural and Applied Sciences** _____

Prof. Dr. M. A. Sahir Arıkan
Head of Department, **Mechanical Engineering** _____

Assist. Prof. Dr. Ulaş Yaman
Supervisor, **Mechanical Engineering, METU** _____

Examining Committee Members:

Assoc. Prof. Dr. Merve Erdal Erdoğmuş
Mechanical Engineering, METU _____

Assist. Prof. Dr. Ulaş Yaman
Mechanical Engineering, METU _____

Assoc. Prof. Dr. Melik Dölen
Mechanical Engineering, METU _____

Assist. Prof. Dr. Orkun Özşahin
Mechanical Engineering, METU _____

Assist. Prof. Dr. Recep Muhammet Görgülüarslan
Mechanical Engineering, TOBB ETU _____

Date:

I hereby declare that all information in this document has been obtained and presented in accordance with academic rules and ethical conduct. I also declare that, as required by these rules and conduct, I have fully cited and referenced all material and results that are not original to this work.

Name, Surname: Sardar Vayghannezhad

Signature :

ABSTRACT

AN AUTOMATED SHRINKAGE COMPENSATION METHOD FOR THE HOLES FABRICATED VIA FFF PROCESS

Sardar Vayghannezhad,
M.S., Department of Mechanical Engineering
Supervisor: Assist. Prof. Dr. Ulaş Yaman

September 2019, 115 pages

This thesis presents an automated shrinkage compensation algorithm for 2.5D specimens to be fabricated via Fused Filament Fabrication process. The algorithm operates on a closed curve representing the hole of a 2.5D specimen, and generates a corresponding compensation structure regardless of the hole's geometric characteristics. Accordingly, this thesis initiates with introducing a viscoelastic model that would reproduce the behavior of the PLA filament from the time of extrusion onto the build plate until it is cooled down to room temperature. Based on the viscoelastic model and corresponding mathematical equations, a final strain associated with a 2.5D structure having a central hole is calculated. Finally, to empirically verify the theory behind this work, three types of tests are designed and conducted. Two of these tests are seek to check the validity of the strain rate already obtained, on specimens without bridge lines. The third test setting, however, brings into play the positive effect that bridge lines have on the shrinkage of the central opening.

Keywords: Shrinkage Compensation Method, Additive Manufacturing, Fused Filament Fabrication, Viscoelastic Model, Zener Model, Stress Relaxation.

ÖZ

ERİYİK YIĞMA MODELLEME İŞLEMİ İLE ÜRETİLEN DELİKLERİN KÜÇÜLMESİNİ OTOMATİK OLARAK ENGELLEYEN BİR YÖNTEM

Sardar Vayghannezhad,
Yüksek Lisans, Makina Mühendisliği Bölümü
Tez Yöneticisi: Dr. Ör. Üyesi Ulaş Yaman

Eylül 2019 , 115 sayfa

Bu çalışma Eriyik Yığma Modelleme işleminde çekmeyi önleyen otomatik bir yöntem sunmaktadır. Yöntem, 2.5 boyutlu bir parçada bulunan deliğin kapalı eğrisi üzerinde çalışır. İç deliğin geometrik özelliklerinden bağımsız olarak çekmeyi önleyen geometriye sahip olan yeni bir 2.5 boyutlu katı modeli oluşturur. Çalışma, kullanılan filamentin (PLA'dan üretilen) baskı tablası üzerine ekstrüde edilmesinden oda sıcaklığına kadar soğuması arasında geçen zamandaki davranışını tanımlayan bir viskoelastik modelin tanıtılmasıyla başlamaktadır. Bu viskoelastik model ile düz bir PLA çubuğunun toplam gerinimi elde edilebilir. Gerinim hızı parçanın deliği üzerinde uygulanarak çekmeyi telafi eden 2.5 boyutlu model elde edilir. Son olarak, önerilen yöntemde kullanılan ve çekmenin telafisinden sorumlu olan çekme köprülerinin etkisi incelenmiştir.

Anahtar Kelimeler: Çekme Telafi Yöntemi, Eklemeli İmalat, Eriyik Yığma Modelleme, Viskoelastik Model, Zener Modeli, Gerilim Gevşemesi

ACKNOWLEDGMENTS

Hereby, I would like to express my deepest appreciation to my supervisor, Assist. Prof. Dr. Ulaş Yaman, for his consistent support and attention throughout my research work. The completion of this thesis would not be viable without his patient guidance, selfless time and encouragement.

I would also like to extend my sincere appreciation to my parents for their warm support and assurance throughout my studies.

Special thanks go also to my brother, Salar, who, despite his busy time, helped me overcome the shortcomings that came up my way in experiments. I am also indebted to him for his sincere assistance with my questions here and there. I am also thankful to my dear friends, Vahid Haseltalab, Hamid Majidi Balanji and Sasan Karimi for their unfailing assistance with my latex work and experiments.

Super-special thanks go to my faithful friend, Maryam Parsian, for her outstanding and sincere assistance with my minor corrections.

I also appreciate my fortune to have beside me my brother and his wife, Sara Razzaghi Asl, for all their kindness and warmth throughout my tough times.

TABLE OF CONTENTS

LIST OF TABLES

TABLES

LIST OF FIGURES

FIGURES

LIST OF SYMBOLS

$\dot{T}_1$	Polymer cooling rate from nozzle temperature to glass transition temperature
$\dot{T}_2$	Polymer cooling rate from glass transition temperature to room temperature
$\dot{T}_s$	Temperature increase rate for printer build tray
τ, τ_f	Relaxation time
E_s	Elastic modulus of build plate
E_{ge}	Modulus of elastic spring below glass transition temperature
E_{mf}	Mean modulus of viscous spring above glass transition temperature
f	Shrunk curve's distance from initial original curve
h_p	Polymer thickness
k	Stiffness coefficient of spring
l	Bridge line length
l_c	Compensated length of cord
l_{fc}	Required length of bridge lines for full compensation
t	Time
T'	Reference temperature in cross-WLF equation
T_0	Nozzle temperature
T_g	Glass transition temperature
T_r	Room temperature
Δl	Shrinkage of bridge lines
α_p	Coefficient of thermal expansion of polymer

α_s	Coefficient of thermal expansion of build tray
ε_0	Initial strain in the creep phenomenon
ε_0	Part of polymer residual strain, caused by nozzle speed
ε_s	Strain of the build plate
ε_η	Damper strain in the Zener model
ε_{pe}	Elastic strain of polymer; symbol used for both above and below glass transition temperature, represented by elastic spring
ε_{pf}	Part of polymer residual strain, caused by temperature decline, and represented by displacement of viscous spring
η	Viscosity
η_m	Mean viscosity of damper/viscous spring above glass transition temperature
σ_0	Initial stress in the stress relaxation phenomenon
σ_d	Stress on the damper in the Zener model
σ_e	Stress on the elastic spring in the Zener model
σ_f	Stress on the viscous spring in the Zener model
σ_p	Stress on polymer filament
σ_s	Build plate stress
σ_η	Stress on the damper in the Zener model

LIST OF ABBREVIATIONS

2.5D	2.5 Dimensional
3D	3 Dimensional
3DP	3D (3-Dimensional) Printing
ABS	Acrylonitrile Butadiene Styrene
AM	Additive Manufacturing
ANN	Artificial Neural Network
ANOVA	Analysis of Variance
BJ	Binder Jetting
CAD	Computer Aided Design
CAE	Computer Aided Engineering
CMM	Coordinate Measuring Machine
CPE	Co-Polyester
CTE	Coefficient of Thermal Expansion
DDM	Direct Digital Manufacturing
DED	Directed Energy Deposition
DLP	Digital Light Processing
DOE	Design of Experiments
FDM	Fused Deposition Modelling
FFF	Fused Filament Fabrication
GA	Genetic Algorithm
HBS	Heat Balance Support
IT	International Tolerances

LMD	Liquid Additive Manufacturing
LOM	Laminated Object Manufacturing
MJM	Multi-Jet Modelling
ND	Nominal Dimensions
PBF	Power Bed Fusion
PLA	Poly-Lactic Acid
PVA	Polyvinyl Alcohol
RP	Rapid Prototyping
RPBPS	Rapid Pattern Based Powder Sintering
SC	Shrinkage Compensation
SCF	Shrinkage Compensation Factor
SDL	Selective Deposition Lamination
SLA	Stereolithography
SLS	Selective Laser Sintering
SLS	Standard Linear Solid
STL	Standard Tessellation Language

CHAPTER 1

INTRODUCTION

1.1 Motivation

Additive Manufacturing (AM) is an all-covering title given to the technologies that are used to create 3D objects through adding material in a layer-by-layer fashion. From the viewpoint of production technique, additive technologies of manufacturing stand in contrast to such traditional approaches as milling and casting, wherein subtraction of material instead of addition is operated on an initially existing body of material. AM technologies emerged as a potential alternative for traditional, subtractive manufacturing techniques since early 1990s, and have received increasing reception over the decades[1].

From a practical standpoint, enhancing the precision of AM technologies seems as a cornerstone for these technologies to be incorporated in industries. Previous investigations have bordered on finding the sources of, and solutions to the shrinkage problem of AM technologies in general. However, a comparative look at different AM technologies suggests that Fused Filament Fabrication (FFF) suffers most from accuracy-related concerns.

Among different types of additive technologies, FFF, alternatively known as Fused Deposition Modelling (FDM), counts as the most typical one applied on plastic materials. For FFF, to find its place in industrial practice, precision appears to have remained a serious challenge. With regard to its temperature-based nature, FFF printing technology tends to be susceptible to accuracy-related concerns. Such concerns arise, in essence, from the temperature decline of the printed substance immediately after deposition occurs. Decrease of the printed part temperature leads, in its turn, to

dimensional shrinkage of the printed model.

Part of the work required to enhance FFF precision needs to deal with accuracy of such interior structures as holes, gaps, slots and other similar empty spaces widely used in engineering mechanisms. This is because these are typically points where mechanical components are joined together. Hence, there is a need for more attention to improve their fabrication precision. The test cases fabricated in this thesis and portrayed in Chapter 5 represent such mechanical components. However, the central hole is not capped because of measurement purposes.

As an approach to minimize the shrinkage amount of a hole located at the center of a 2.5-dimensional structure, shrinkage compensation (SC) method has been considered in this thesis. As the main contribution of the present work, a fully automatic algorithm is developed that can take a closed curve as the central hole of a 2.5D structure, and produce, based on SC method, bridge lines stretching perpendicular to the central hole perimeter. Worth a mention is that, a mathematical model has been used to predict the shrinkage behavior of the central hole and that of the bridge lines. The interplay between these two sets a platform to control the central hole print precision.

1.2 Outline of the Thesis

To take a broad look at the factors which AM accuracy depends on, some approaches and conclusions previously drawn up to tackle the precision problem are explored in Chapter 2. The mechanism used in this dissertation via which shrinkage is alleviated is the focus of Chapter 3. Chapter 4 includes the algorithmic model that deals with the geometry of the central hole to provide a structure suitable for the shrinkage compensation method. Subsequently, breakdown of measurements of printed parts is presented in Chapter 5 to be compared with the software modelling results. Chapter 6 aims to present a recapitulation of the thesis and future works that can be pursued along the lines of the present work.

CHAPTER 2

BACKGROUND

2.1 Introduction

To approach the problem of AM precision, a basal introduction to AM procedure and its advantages are outlined in Section 2.2. Earlier schemes carried out to achieve an understanding of how printing accuracy is governed is the focus of Section 2.4. Finally the computer software used in the thesis is briefly explained in Section 2.6.

2.2 Review of Additive Manufacturing

The term AM is an umbrella name for all such terminologies as 3D Printing, Direct Digital Manufacturing (DDM), Rapid Prototyping (RP), each of which either emphasizing a specific aspect of AM, or referring to a specific stage in the evolution of AM. Although the very beginning days of AM had started with Rapid Prototyping as a method to produce experimental models, later on, AM was used for fabricating final specimens of an object design intended for use in aerospace, medicine, automobile industry, fashion industry and the like. Different additive technologies and stages commonly shared by those are outlined in the next section.

2.2.1 AM Subtypes and Stages

All additive manufacturing technologies can be categorized in a variety of fashions. As one such classification, based on ASTM F2792, all AM families can be categorized as follows [2]:

a) VAT Polymerization, also known as SLA (Stereolithography) or DLP (Digital Light Processing) could be described as solidifying of photopolymer resin in a vat via selective exposure to ultraviolet light cast from a laser or a projector (Figure 2.1).

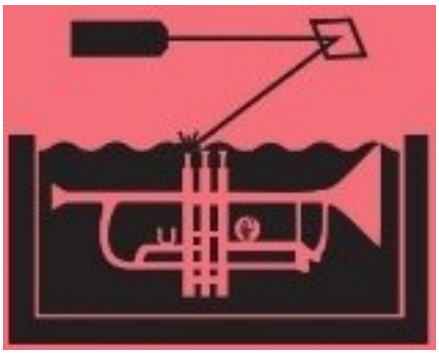

Figure 2.1: VAT polymerization [2]

b) Powder Bed Fusion also known as SLS (Selective Laser Sintering), could be described as a process where material in the form of powder is melted via electron beam or laser beam in a selective fashion (Figure 2.2).

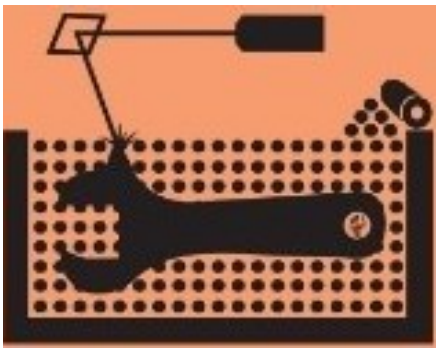

Figure 2.2: Powder Bed Fusion [2]

c) Binder Jetting, also known as 3D Printing (or 3DP, for short) can be defined as a technique where liquid bonding agents are selectively applied onto thin layers of powdered material to build up parts layer by layer. The binders include organic and inorganic materials. Metal or ceramic powdered parts are typically fired in a furnace after they are printed (Figure 2.3).

Figure 2.3: Binder Jetting [2]

d) Material Jetting also known as Polyjet or MJM (Multi-Jet Modelling) is a procedure where material is deposited in droplets to fabricate a final part. Among a variety of material jetting techniques, some common ones are jetting of a photo-curable resin to be solidified under UV light, and thermal jetting of melted materials which cure afterwards in room temperature (Figure 2.4).

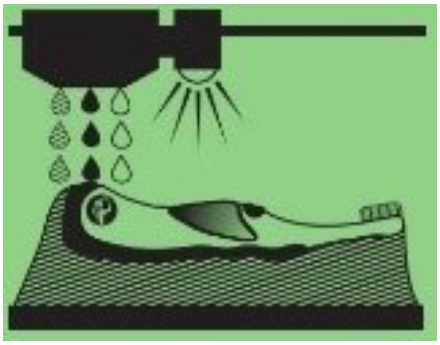

Figure 2.4: Material Jetting [2]

e) Sheet Lamination, also known as SDL (Selective Deposition Lamination) or LOM (Laminated Object Manufacture) can be described as a method wherein material is piled and laminated together. This is followed by cutting out unwanted parts of the model after the object is built. Lamination can be done via adhesives, chemicals, or through ultrasonic welding (Figure 2.5).

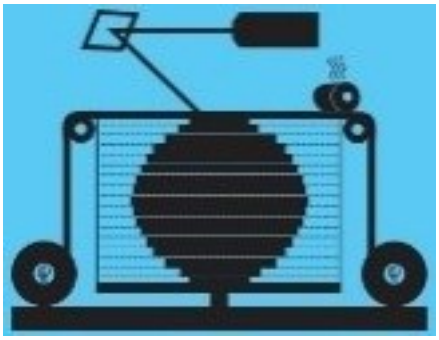

Figure 2.5: Sheet Lamination [2]

f) Material Extrusion, also known as FDM (Fused Deposition Modelling) or FFF (Fused Filament Fabrication) is a process where material is extruded through a nozzle in form of filament melted beads to form a layer. All the layers are thus attached to form multi-layer product (Figure 2.6).

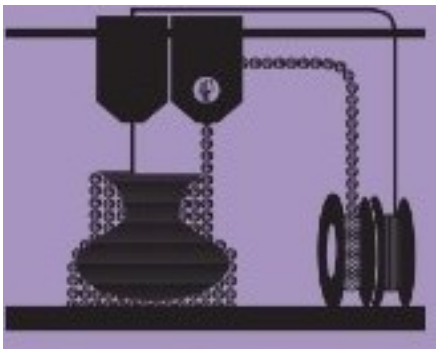

Figure 2.6: Material Extrusion [2]

g) Directed Energy Deposition (DED), also known as LMD (Laser Metal Deposition), operates based on feeding of wire or powder into a melt layer of material on the part body. The body is exposed to an energy source like a laser beam. The layer then solidifies on the previous layers (Figure 2.7).

Figure 2.7: Directed Energy Deposition [2]

h) Hybrid, also known as AMBIT, can be defined as a process wherein AM and traditional subtractive processes are brought together. Hence, merits of both technologies are tapped into a single station. The additive process of the Hybrid AM technology usually comes in the form of laser material deposition, which in its turn counts as a DED technology.

Regardless of the variety of AM subtypes, all the manufacturing processes used in any type of an AM technique have in common a handful of elements as follows [51]:

a) preparing a digital blueprint of the 3D model using CAD (computer-aided design) software.

b) converting the CAD file to an STL (or other format) file; An STL file makes use of tessellation to define and describe model surfaces. In other words, the STL file stores information of the models surface coordinates, in terms of geometric shape(s), and does so in an optimized way, so that no mutual lapping is there between two geometrical shapes.

c) After the STL file is produced, a distinctive point between conventional and additive manufacturing arises with importing the STL file into slicing software. The slicing computer software counts as a medium that enables a 3D printer to interpret information it receives from the computer.

d) Running the printing machine.

e) Post-print operations, if need be.

A summary of these steps is shown in Table 2.1.

Table 2.1: Design and fabrication steps commonly shared by various types of additive manufacturing technologies [3]

1	2	3	4	5
CAD-based model	.STL file	Sliced Layer	AM system	Post-processing

2.3 Advantages of the AM Technology

Owing to the AM technology, engineers are enabled to manufacture sophisticated parts used in aerospace and machinery (See Figure 2.8). Manufacturing these parts via traditional technologies requires, in comparison, a greater deal of time and cost dedicated for such manufacturing processes as forging, slotting and sculpting. It is said that, in actuality, 3D printing a structure as simple as a cube is more time-consuming than a much more sophisticated model.

Figure 2.8: Yellow blades of gas turbine are fabricated by Mitsubishi-Hitachi Power Systems Americas, owing to additive manufacturing[86].

Apart from time- and cost- related merits, need for diversification is fulfilled more conveniently via AM. Because, different from the conventional manufacturing where even small iterations in the model would require tooling on a production line to be changed out, AM admits such modifications on the model, merely by introducing changes in the CAD model, or material distribution throughout the model structure. As a result, diversified model of alike designs are easily attainable. This benefit can be even more pronounced considering the fact that usually a high percentage of designs ready for conventional tooling, undergo modifications and design alterations in the course of production.

Reduction in waste generation is another major benefit that AM offers. Traditional manufacturing involves working on a block that is initially larger than the ultimate product. Hence, it entails generating waste material which has been subtracted from the original block and is not ready for immediate re-use [3, 4]. Figure 2.9 shows in a schematic fashion the difference these two fabrication technologies have in terms of their waste generation.

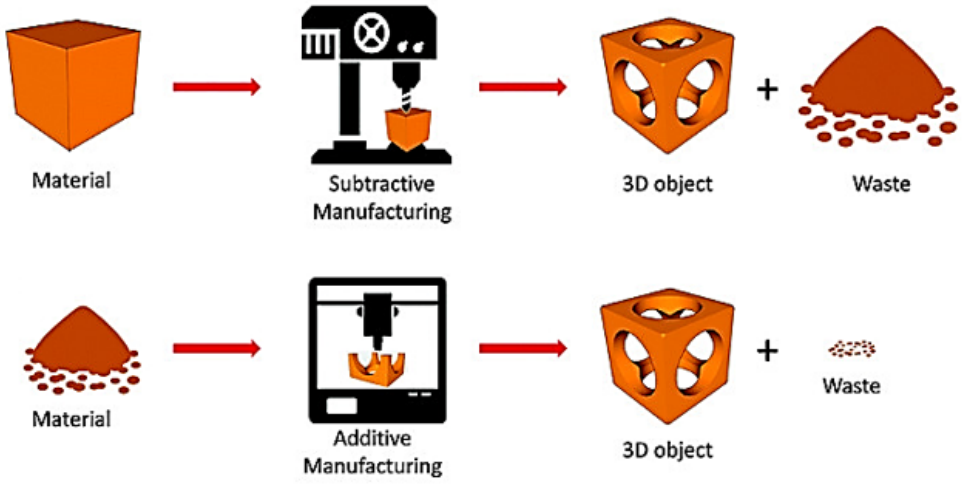

Figure 2.9: Additive vs. subtractive manufacturing compared; More waste is generated in subtractive fabrication [4].

2.4 Precision Problems in Sight of Previous Literature

A wide spectrum of research has been conducted to date to investigate the shrinkage of AM processes. In the sections to come, studies concerned with AM precision have been cited and reviewed based on the types of AM processes. However, since some terminologies have been commonly used in the previous literature, a brief review of these technical vocabulary is presented below.

a) Benchmarks are CAD models that contain a collection of geometrical features of various size, location and orientation. Benchmarks are meant to help evaluate generally the performance, and particularly the precision of an AM technology. Thus, the purpose of benchmarks is both to assess the operation quality of an individual AM technique and to compare as well as to contrast different AM technologies.

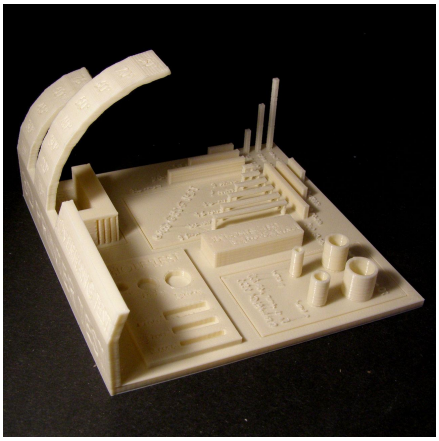

Figure 2.10: A benchmark with various geometrical features to test print functionality [5]

b) Very commonly, practical experiments involve numerous parameters of influence in precision of printed parts. Therefore, exploring the effect of all the combinations of existing parameters can be a demanding task. The Taguchi Method proposes a guideline to optimally choose those parameters that give minimal number of tests with maximum volume of information. The Taguchi Method observes design to be more critical than the manufacturing procedure in quality control and attempts to remove discrepancies in production before they can take place. In AM arena, the Taguchi Method is usually employed as an optimization method to examine how the involved parameters affect the mean and variance of a process performance characteristic; i.e the characteristic that defines how well the process is functioning. As such, the Taguchi Method is to optimize the parameters involved in the manufacturing process, so that the minimal deviation from the CAD model is resulted.

   The experimental arrangement offered by Taguchi deals with using orthogonal arrays to systematize parameters of influence in the process and the range of variation within which they should be manipulated. Instead of having to assess all possible combinations of parameters, despite the factorial design, the Taguchi method tests pairs of combinations. This enables the collection of the primary data that the most affect product quality, and does so with a minimum number of experiments, therefore saving time and resources.

Like stated in Chapter 1, as AM applications expanded, they came closer to the fabrication of ready-to-use products. However, dimensional inaccuracy of AM-produced parts seems to persist as a central issue in AM manufacturing field. As a result, wider adoption of the AM processes in current manufacturing industries, in many instances, requires a post-processing phase that can improve product surface finish and dimensional precision. For instance, the dimensional precision of AM is crucial for products fabricated in bio-medicine, because among the merits exclusive to AM, is fabricating customizable products that can individually suit each patients body. As a second example, technical requirements of reverse engineering, too, calls for higher dimensional accuracy of a dismantled mechanism to flawlessly fit in the engineering mechanism at hand. Along the same lines, turbine blades require utmost dimensional accuracy to operate on the most efficient energy level and to be invulnerable to wear and tear arising from vibration. The poor resolution of some AM technologies also hampers their adoption in electronics that demand meticulous design patterns or miniature part dimensions. All these examples and many more bring to the forefront the necessity of enhancing AM processes dimensional accuracy, before they can be truly integrated into the present-day manufacturing industries. To tackle this problem, extended studies have been done to date, some of which are outlined below, categorized based on their research field.

2.4.1 Studies on Precision Benchmarks

Over the past years, AM technologies have experienced unprecedented development, leading to a point where various AM procedures with different working principles, need to be compared and contrasted for their functionality. Thus, the need for a strict criterion that could juxtapose strengths and weaknesses of each AM process made itself felt. To this end, designing and fabricating benchmarks, i.e. 3D volumes having key geometrical features, has been considered in the literature studies.

One such research was conducted by Mahesh et al.[6]. They studied and modelled benchmarks before being fabricated via four AM processes, namely FDM, SLA (Stereolithography), SLS (Powder Bed Fusion) and LOM (Laminated Object Manufacturing). Results show that while SLA has optimum performance in comparison

with the other three processes, Fused Filament Fabrication suffers the most from dimensional accuracy.

According to Mahesh et al.[48], another categorization of benchmarks based on their purposes offers three classes; viz. geometrical benchmarks, mechanical benchmarks and process benchmarks. The first group is intended to examine process performance from such geometrical viewpoints as repeatability, surface roughness and dimensional accuracy. The second group comprises of benchmarks for comparing AM processes for parts mechanical properties like strength and warping. The third class aims to set a series of process parameters such as speed, orientation, etc. for all AM processes.

An outline of available benchmarks as well as some rules of thumb for benchmark design according to the geometries of real-life industrial objects have been offered in a study carried out by Rebaioli and Fassi[7]. The conclusion they draw categorizes guidelines for benchmark fabrications under four categorizations; that is, overall dimensions, feature geometry, feature dimensions and feature position and orientation.

Dimensional accuracy is defined as the level of conformity of the fabricated part geometry to that of the digital design. Dimensional accuracy, as such, is usually assessed via statistical approaches [1]. Dimensional errors in AM processes stand out mainly in the form of either shrinkage, which is induced from temperature variations over time, or warpage, which results from internal stresses caused by heat gradient across the printed part [8]. In its either form, dimensional imperfections of AM products appears to be a major challenge to additive manufacturers today.

Sources of geometrical inaccuracy and corresponding solutions related to only those AM processes where a layer addition is the basis to the manufacturing procedure, have been considered also by Umaras and Tsuzuki [87]. Based on their work, dimensional inaccuracies in different AM technologies can stem from design/software induced inaccuracies, process associated inaccuracies and material induced inaccuracies.

2.4.2 Studies on SLA Precision

Among various AM processes, the SLA process has received good deal of attention in the literature for its accuracy. Campanelli et al.[9] for instance, probed this problem

from a statistical stance. A benchmark was developed and a generic error index was calculated to assess the general distortion factor of the print according to the benchmark features. They adopted the Taguchi methodology to optimize the array of process parameters, namely layer thickness, hatch over-cure, border over-cure and hatch spacing involved in the stereolithographic accuracy. Results suggest that an optimal value can be assigned to each of the involved parameters to address SLA precision problem. The same values for the best set of process parameters also represented a final product that would not need to be post processed, due to having completely solidified layers.

In a similar fashion, a statistical method was conducted by Chryssolouris et al. [10, 11] to evolve a specimen, fabricated via stereolithography, to identify the chief process parameters that influence precision in each direction. They attained a view as to what extent each parameter can affect print accuracy in a given direction. Their work is valuable also in that any combination of process parameters can be predicted for the dimensional precision that it may yield. Therefore, the optimum set of parameters, giving the most accurate part print, is achievable with the method presented in that study.

Another statistical approach was taken up by Khorasani and Baseri[12] in a study that adopted an artificial neural network (ANN) to uncover the correlation of three distinct process parameters on dimensional accuracy of SLA parts with H shapes. Thus, they looked into layer thickness, hatch over-cure and hatch spacing as influential parameters. The ANN was then introduced to two optimization algorithms to yield the best numbers for the parameters. The neural network approach was found to be capable of predicting both shrinkage and distortion of the SLA artefacts of an H shape. Using H-shaped specimens to evaluate SLA accuracy was also employed as an approach in other studies. For instance, the accuracy of SLA-printed H-4 prototypes was found by Huang and Lan [15, 16] to be adversely affected by volumetric shrinkage and curl distortion. These effects were shown to be specially pronounced when the part to be printed is hollow, or after the support material is removed. To counteract against this drawback, Huang and Lan introduced CAE to rapid prototyping, and thus a dynamic finite element simulation code was used. Upon this code, photopolymerization, and likewise the curling pattern of H-4 prototype was simulated. Once the distorted outline

of the part is determined, a reverse compensation approach is employed to create a new CAD model in prior to build-up fabrication. Another study on SLA accuracy was taken up by Taft et al.[19]. The study deals with the precision of SLA fabricated craniofacial prototypes. A contact probe was used to contrast the actual model dimensions with those of the CAD model. They found that the accuracy suffered the most in the Z direction of the model.

2.4.3 Studies on Binder Jetting Precision

As the case with Stereolithography, numerous researches have also been done to explore binder jetting, alternatively known as 3D printing, accuracy. Dimitrov et al. [20] carried out experiments on a series of materials in powder form to work out binder jetting accuracy mechanism. Prototypes of specific geometrical features were fabricated with various powders. CMM was used to measure inaccuracies, before a statistical approach was carried out to evaluate geometrical and dimensional inaccuracies. To secure consistency of interpretations, a globally accepted measurement standard, called International Tolerances (IT) grades, was employed. Results show that three concrete factors are of significant effect on 3DP dimensional accuracy. These were said to be the material in powder form, nominal dimensions (ND) of the part to be printed, and the 3D printer axis along which printing is performed. It was shown that powder material has more profound influence though. Likewise, plaster powder materials lead to less dimensional inaccuracies than their starch-based counterparts, although both types of powders result in the enlargement of the model compared to the CAD design. Despite their attempt to provide benchmarks with powder materials, the method presented in their study can be used in only a limited number of printing machines.

Gaytan et al.[17] implemented shrinkage compensation method to make up for accuracy issues observed in the binder jetting (3DP) of barium titanate BaTiO3. Shrinkage was found to show itself more in parts sintered at higher temperatures, while the axis of manufacture was shown to have its part to play in shrinkage anisotropy. The least rates of shrinkage were observed at temperatures around 1260 ^{0}C for the three main axial directions. The higher rises the sintering temperature from this figure, the more

shrinkage is found in three dimensional axes, x, y and z, with the z axis suffering the most inaccuracy of around 30 percent.

Lee et al.[21] looked into the reason behind low accuracy in the Z direction in the 3DP process. Results suggested that a compile of layers exposed to compressive loads, end up being displaced in the downward direction. Such loads can result from the weight of layer stacks compiled together, for example. A model was developed to predict layered powder beds displacement. The experimental work they carried out helped achieve an optimal size for the powder ($23\mu m$) to attain higher precision.

Vaezi and Chua [22] looked into the parameters influential in the strength and surface finish of binder jetting produced parts. Utilizing some prototypes, it was revealed that the thicker the binder is, the less quality the surface finish tends to be, and the more tensile and flexural strengths improve. Increase in layer thickness, on the other hand, results in the bettering of surface finish and in the deteriorating of tensile and flexural strength.

Stopp et al. [23] acquired a novel 3DP approach and found that dimensional precision relies on the positions and directions of spots being processed, with the former having more influence in print accuracy. To enhance dimensional accuracy, a preparatory configuration is suggested via which the known imperfections of the printer are counterbalanced. This is much alike to the shrinkage compensation factor used in some other studies, except that the preliminary configurations in this study was carried out using a piece of software, to give a deformed virtual prototype. This deformed prototype was then printed to yield the most accurate result.

2.4.4 Studies on SLS Precision

Y. Tang et al. [19] studied the SLS process for its accuracy. The laser, particularly, the laser scanning system, was decided as the source of dimensional imperfections from a hardware viewpoint. It was concluded that the software-hardware interrelation plays an effective role in dimensional inaccuracy of the SLS process. A piece of software was developed thus to address the errors induced by laser scanning system. A calibration method was also employed in the form of a shrinkage compound compensation to deal

with the imperfections arising from material shrinkage and laser beam offset. Along the same lines, using a neural network and genetic algorithms (GA), Wang et al. [25] explored the possibility of enhancing an array of nonlinear parameters at play in the SLS process aiming for the minimum shrinkage rate.

An innovation was also brought forth by Zhou and He [28] to minimize SLS inaccuracies. Their method, called Rapid Pattern Based Powder Sintering (RPBPS), is founded on the integration of powder sintering, 3DP and lost-wax casting and employing proper binder kind and binder proportion in smaller temperature spectrum in the process. They could attain a maximum linear shrinkage of 3.5 percent for products manufactured via rapid pattern based powder sintering.

Zakaria et al. [27] used indirect metal selective laser sintering (IMSLS) to explore the inaccuracies stemming from distortion of the fabricated part. To minimize distortion, the authors emphasized that accessibility of liquid in initial stages of the process is indispensable for ensuring less distortion rates. They also point out that the stress the part experiences in the sintering or sintering infiltration phase considerably determines the deformation rates. Effect of substrate temperature was also studied by Chung et al. [26] to show its influence in SLS produced models warpage.

Liu et al. [24] accomplished an algorithm of integrating heat balance support (HBS) to tackle the problem of heat unevenness in the SLS chamber, hence enhance dimensional precision of the process.

2.4.5 Studies on FFF (Fused Filament Fabrication) Precision

In a research work by AnHua et al. [51], the interrelation between process parameters and their final effect on the FFF printing precision has been examined. Different sources of inaccuracies like shaped errors, poor surface qualities and dimensional errors were looked into and some general countermeasures were offered. According to their findings, stair stepping, for example, occurs because of slicing of the part model in a vertical direction due to which information related to the space between two consecutive layers becomes missing. To remedy this drawback, it is suggested in their approach that the part be sliced according to its geometrical specifications

(i.e. adaptive slicing). A second remedy is an approach called in the paper as sloping slicing. According to this approach, slicing orientation need be adaptable to always stay perpendicular to the normal vector on the part surface.

Employing a self-compensating method to account for FFF shrinkage is the focus of a study carried out by Yaman [74] which is also the partial basis for the thesis in hand. To elaborate, 2.5D artefacts with interior holes were printed. Surrounding the interior hole, however, were printed an array of line segments that connected to the central hole wall on one end. It was demonstrated that the shrinkage of line segments can be utilized to compensate for undesired shrinkage of the interior hole or slot. In fact, the peripheral lines, themselves, shrink towards the perimeter of the model, and thus stretch out the hole, counterbalancing the hole shrinkage. Put simply, this method operates on the shrinkage of the lines to outweigh the shrinkage of the interior structure, hence is given the name self-compensating method. Experiments performed, CMM measurements and numerical analyses suggested this method is capable of achieving 80 percent of shrinkage compensation in circular voids, and considerably improve dimensional contraction in rectangular slots.

Along with the same study line and working on similar artefact structure, Dilberoglu et al. [36], simulated the shrinkage behavior of the printed samples to compare and contrast results with the outcomes obtained via CMM measurements of ABS filament. Among the conclusions was that part accuracy worsens in the upper layers. This was attributed to the fact that heat transmitting from lower layers augments as the height of the prototype increases. The counter-shrinkage impact that auxiliary lines showed itself in the minimal displacement of the perimeter of the holes. The peripheral lines height, their distance from the center of the geometry and color of the model each was found to have its share in the final shrinkage rate.

Introducing some design software for AM systems is a typical way that enables the use of a shrinkage compensation factor (SCF) to account for the shrinkage phenomenon. Some studies have proposed a process for enhancing this setting in design software for a given specimen [29, 30]. As found by Turner and Gold [1], the thermo-mechanical behavior of AM models is not anticipated to be isotropic, rather, it has been expected that shrinkage amount be dependent on the part orientation and design. This casts

doubt on the efficiency of the SCF approach as a one-fits-all method [48].

A critical review of the existing literature was held by Turner Gold [1]. It is stated that both resolution and dimensional precision are dependent finally on the extent to which print material extrusion can be properly controlled. Controlling the rate at which filament is fed to the liquefier is thus a factor worth concern. Authors maintain that this sort of filament control needs to find its way to enhanced control algorithms, process monitoring capabilities and feedstock characteristics. They also hold the idea that shrinkage compensation factor would not properly tackle the problem of anisotropic shrinkage or thermal changes that occur in the course of print, especially for larger print specimens where occurrence of larger thermal gradients is common.

Other investigations are available which deal with optimizing of process parameters involved in FFF procedure. The research undertaken by Chang et al. [46] is a case in point that sees print inaccuracy in the two forms of extrusion vacancy and profile error. They used an image measurement approach to assess profile errors and extruding apertures. A spiral 2-D curve with 19 cylinders were printed on the curve. The actual centers of these 19 cylinders were compared with the corresponding points in the CAD model. The discrepancies of the two, obtained this way, was taken as the groundwork for calculating the profile error. Since the part surface cannot be evenly filled up extruding apertures are taken in their study as a second critical quality factor to be considered. Their investigation looked into influence of such elements as contour width, part raster width and contour depth on specimens profile error and extrusion aperture using Taguchi method. They concluded that from the three elements mentioned above, contour width had the most effect on extrusion vacancies and profile errors.

Optimizing process parameters was also the focus of another paper authored by Abu Bakar et al. [31]. In their study, the most necessary processing parameters to look into were determined as the raster angle, slice thickness, tool path, deposition speed and build orientation. These parameters were then brought to optimum after being examined for values that would give the best dimensional precision and surface finish. Conclusions they came up with suggest that FFF fabrication of circular specimens is more susceptible to inaccuracies due to restrains in the nozzle head. They also

offer a lower limit of thickness for each feature of a benchmark to be fabricated in all directions x, y and z that would result in the best accuracy conditions.

Another statistical approach to FFF accuracy, from an optimization viewpoint, was taken up in the study made by Sood et al. [32]. They attained, owing to the Taguchi method and an artificial neural network (ANN), an optimized array of parameters including layer thickness, raster angle, and part orientation, so that minimum deviation from the CAD model dimensions was achieved in all the three axes of x, y and z, simultaneously.

Apart from common process parameters involved in FFF, the influence of support base in the distortion of the part in the Z direction, i.e. the direction along which fabrication progresses, was examined by Volpato et al. [37]. They used two support configurations, as well as the default one. Based on their findings improving the support base on which the very first layer of the product is deposited leads primarily in the enhancement of the parts bottom layer. This, in its turn, shows to mitigate the dimensional error along the Z-axis up to 50 percent.

Other standpoints have been taken towards FFF precision too. Saqib et al. fabricated an FFF benchmark with both thick and thin walls [47]. Looking for the specimens three distinct geometric attributes, namely flatness, perpendicularity and cylindricity, they found that the specimen accuracy comes mainly down to the flatness and perpendicularity of its geometrical features. Another conclusion they pointed out was that geometrical characteristics have a greater share in FFF dimensional accuracy than processing parameters.

Another such viewpoint involves volumetric shrinkage of FFF, induced by curling of manufactured ABS parts. This was looked at in an analysis conducted by Pavan Kumar Gurrala et al.[34]. Design of experiments (DOE) was used to find the least defining number of equations that can explain volumetric equations, in conjunction with ANOVA (analysis of variance) which is used to draw the equations having influence in volumetric shrinkage. The approach they offer anticipates the parts curling behavior and accordingly estimate its effect on the volumetric shrinkage. The authors attempted to test the influence of three machine setting parameters in the volume shrinkage and the part curl pattern, viz. model interior infill, horizontal

direction, (along the x-y plane of the machine) and vertical direction (along the y-z plane of the machine). By horizontal direction authors refer to the configuration wherein the nozzle moves along with the length of the specimen, fabricating more layers with each single layer having less filament deposition. What vertical direction stands for is, contrarily, the experimental setting wherein more filament is molten in a single layer and consequently fewer layers are deposited on top of one another. Results the authors drew indicate that volumetric shrinkage has the tendency to prevail in horizontal and vertical direction configurations more than it is dependent on the interior infill of the part.

As another form of AM deformation, warpage is commonly held as a reasonable criterion for assessing the quality of an FFF-printed model, and is believed to come down to factors like setup of manufacturing parameters, filament characteristics, geometrical arrangement of the CAD model and toolpath configuration [33]. In general, warp deformation can be considered as the accumulation of inter-layer and intra-layer (side-by-side) deformations of printed fibers. These deformations, in turn, are resulted from internal stresses within the printed part. These stresses seem an inevitable consequence of layers cooling down from T_g to the build environment temperature. Generation of internal stresses can be safely simplified to the procedure of cooling down from T_g to room temperatures; i.e. such stresses are not significantly produced when the part temperature is over the glass transition temperature [40]. If not adequately pliable in temperatures above T_g, the lower layers can undergo delamination in extreme cases.

More in-depth investigation into sources of warpage, as one of many forms of imperfections FFF process sees to itself, is carried out by Anhua et al., and solutions are offered [51]. Uneven distribution of temperature is said to be due to the fact that a bead being extruded from the nozzle loses its thermal energy to the previously deposited layers below. This causes the lower roads of material to rise in temperature to above glass transition temperature (T_g) [39].

Optimizing the toolpath can also offer a partial solution to warpage arising from thermal gradients. By implementing this solution, the time between deposing of two adjacent roads of melt reduces, hence the reduction in thermal gradient [8, 33].

The effect of the thermal gradient is also alleviated in manufacture systems by controlling the temperature of the fabrication environment in an oven. Lack of such temperature control system, such as those based on the RepRap design [41], is presumed to restrict smaller systems to using of specific polymers of lower melting temperatures (e.g. ABS) and to manufacturing of comparatively small part sizes. Convective cooling of the newly deposited material is facilitated via air flow passing across the layers. Figures for convective heat transfer coefficient are estimated by Bellini [42]. The rate of air flow is said to be well dependent on the position and orientation of the part in the build environment. As a result, the heat transfer coefficient value is simply expected to vary across different areas in the fabrication environment. Apart from heat transfer coefficient in the build chamber, part size shape and parts distribution too have shown to have their influence in warpage of the part [39].

In one analysis [8], the thermal expansion coefficient of FFF- manufactured ABS specimens was found to be about an order of magnitude smaller than the corresponding figure for bulk ABS material. This discrepancy was attributed to the expanding of the extruded material and thus filling up the void spaces in the test specimen, with a subtle reliance on the density of the voids in a given orientation of the part [43]. This, at least partly, gives a reason for the observed difference in thermal expansion coefficients. Controlled introducing of voids to manipulate the thermal expansion of extruded roads has been looked into in studies carried out by Sigmund et al. [44, 45], and Bertoldi et al. [43]. Nonetheless, orientation was found to have minimal impact on the expansion, and no theoretical relationship was achieved [1]. A second cause for the mentioned difference can be due to polymer chains tending to line up more orderly after extrusion than in the feed filament. Shrinkage of a printed segment of ABS was found, by Rodriguez et al. [29], to be much less than that of a feedstock ABS filament upon thermal annealing.

The very procedure of data translation from various formats of CAD files to the command file was inspected in detail by Fadel and Kirschman [40]. They determined some significant factors that can induce errors, and attempted to propose ways of controlling those deviations.

Miscellaneous studies on CAD Files are also available that call in question the validity

of the currently used STL transfer format for producing a precise enough an outcome. One such investigation was done by Lemu and Kurtovic [49] to find that the STL, in comparison with VRML format, is somewhat archaic for accuracy concerns, and thus maintain the idea that a novel kind of CAD standards need to be brought forth.

A comparison among printing machines of FFF, Polyjet and SLA was examined in a research undertaken by Brajlih et al. [50]. As a methodology, they set a schematic that is said to be based on the prototypes characteristics and hence secures fair comparison among different AM machines regardless of the machine properties. The conclusion they draw reveals that the polyjet apparatus can keep an accuracy range of 0.0 to 0.8 and thus is the first on the list as far as printing precision is considered.

2.5 3D Printer Used in This Study

The 3D printer used in this dissertation is the FFF-type Ultimaker 3 Extended brand. Ultimaker is a 3D printer machines manufacturing company located in the Netherlands, with assembly lines and offices in the United States. They manufacture 3D printers of FFF type, develop software for 3D printing, and sell 3D printing materials. The Ultimaker 3 Extended brand is actually one member of the Ultimaker 3D printer family. Other members include Ultimaker 3, Ultimaker 2, Ultimaker S5 and Ultimaker Original+. Products of the company have applications in industries such as automotive manufacturing, small scale manufacturing, architecture, education, etc. UM3 Extended can use as its print material such filaments as PLA, ABS, PVA and exotics. One feature of the UM3 Extended that makes it distinct from Ultimaker 3 and other products of the company is that the print tray has vertical motion range, not the nozzle. The printer enjoys a heatable print platform, ability of dual extrusion and printing resolution of 20 microns and maximum print speed of 300mm/s. Other distinctive features to the machine is its bed levelling ability, on-board camera and Wi-Fi connection facility. Figure 2.11 depicts different hardware parts of the machine.

Below, a number of features of the machine are elaborated on[53]:

a) One of the major advantages of the Ultimaker 3 Extended version is the printers capability to have dual extrusion which refers to extruding materials either in

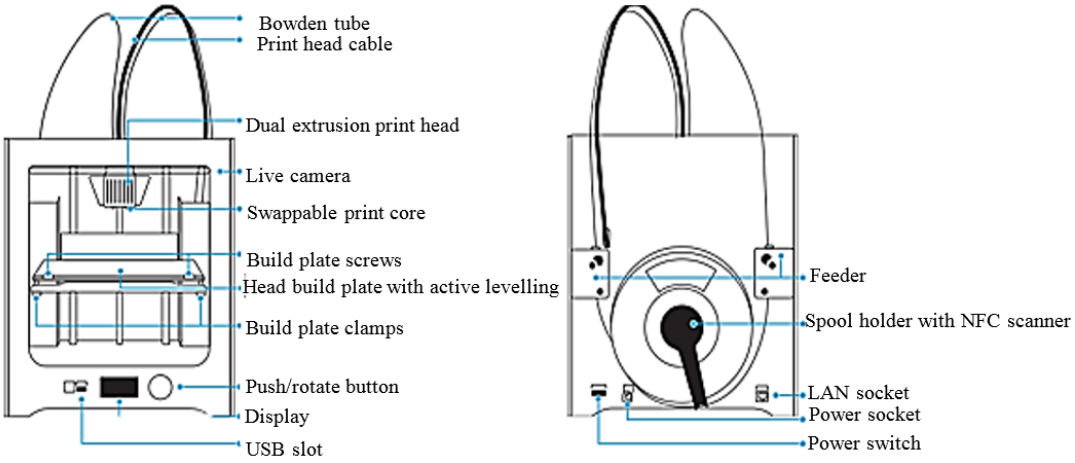

Figure 2.11: Ultimaker 3 Extended hardware parts[52]

two colors or in the form of a build and support material.

b) Another strength that places the machine among professional 3D printers is a material detection system. According to this feature, the embedded spool is automatically detected for its specifications, and printer adjustments are tuned accordingly. This is done via an NFC scanner.

   The glass build plate can range in temperature from 20 C to 100 C, allowing more varied options for materials.

c) Ultimaker 3 Extended also benefits from an auto-levelling feature (active levelling) on its printing tray. Owing to this feature, the distance between the nozzle and the build plate is fine-tuned so as to avoid tilted extrusions and ensure plate calibration and improved adhesion. Although this asset is not meant to fully accommodate for the print level, it results in higher quality production.

d) The support material is PVA (polyvinyl alcohol) material which is water-soluble, and hence enables complex geometrical product designs.

e) Internet connection is another positive point to the UM3. According to this feature, the printing scheme can be sent to the printer via Wi-Fi or LAN connection. The printer also supports USB connection. The Wi-Fi connection also provides users with a live camera monitoring advantage.

A summary of printer specifications are listed in Table 2.2

Table 2.2: Ultimaker Extended 3D printer specifications

Ultimaker 3 Specs and Properties	
Assembly type	Pre-assembled
Layer resolution	0.25 mm nozzle : 150 - 60 micron 0.4 mm nozzle: 200 - 20 micron 0.8 mm nozzle: 600 - 20 micron
Build plate	20^0C to 100^0C heated glass build plate
Build plate leveling	Active leveling
Print technology	Fused Filament Fabrication (FFF)
Print head	Dual extrusion print head
Print core replacement	Swappable print cores
Build speed	< 24 mm^3/s
Print head travel speed	30 to 300 mm/s
Feeder type	Dual geared feeder
XYZ resolution	12.5, 12.5, 2.5 micron
Nozzle diameter	0.25 mm, 0.4 mm, 0.8 mm
Nozzle temperature	180^0C to 280^0C
Nozzle heat-up time	< 2 minutes
Build plate heat-up time	< 4 minutes
Operating sound	50 dBA

2.6 Computer Software Used in This Study

Grasshopper 3D, the software used in this work, was first designed and published by Robert Mc Neel and Associates in 2009 as a programming language primarily for, non-programmers. Grasshopper is a visual environment in the sense that it uses components with nodes, i.e. input(s) and output(s), as its programming elements. As opposed to coding languages, Grasshopper 3D is a visual programming environment devised as a free plug-in for Rhinoceros 3D, the digital modelling software. A canvas, as well as component palette, comprises the software interface on which components can be dragged, dropped and connected to one another. This interface, therefore, works as a platform for node-based algorithm of interconnected components.

The most common terminology related to Grasshopper 3D is listed below:

a) **Component**: a building-block that executes a particular action.

b) **Parameter**: a component of special performance that holds data (values) rather than performing an action.

c) **Slider**: a component that enables the user to determine numeric values for a components input.

d) **Panel**: a utility that enables the user to display numeric values or text. A panel can also be used like a slider, for determining values too, with the difference that, instead of a range of values, a discreet value can be assigned to a panel.

e) **Algorithm (Definition)**: A grasshopper definition is comprised of a network of components interconnected via connections and using sliders, wherever necessary, as numerical inputs. Data from one component is transferred to the other via wires that connect an output of one to the input of the other. The outcome of a definition is displayed on Rhino interface. As a plug-in to the Rhino, data required for a component can either be imported directly from the Rhino environment or picked from another components output on the Grasshopper canvas.

   As samples of components interface, a number of Grasshopper 3D elements are depicted in Figure 2.12.

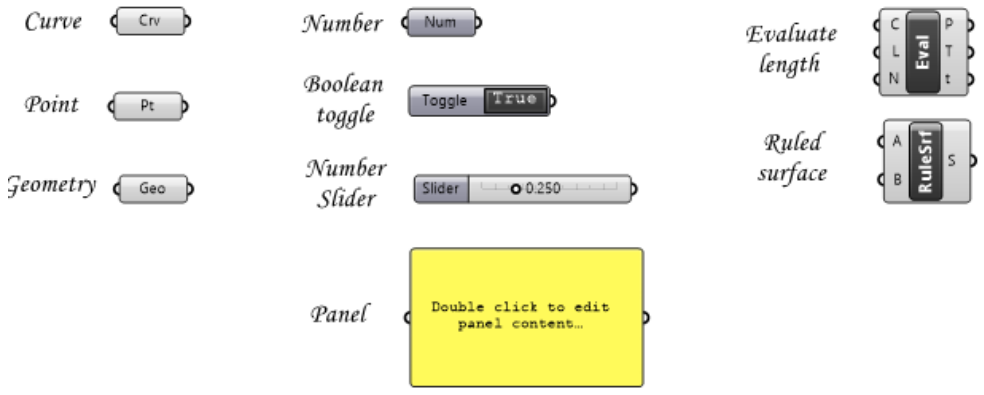

Figure 2.12: Grasshopper 3D sample elements

2.7 Closure

For AM processes to find their true place in the manufacturing industry, the issue of production precision needs to be overcome. Despite the initial stages of AM development when accuracy was not a primary question, over the past two decades the need for improvement in this area has been increasingly felt. To that end, various studies have been conducted on geometrical benchmarking of AM processes, both to compare different AM technologies and to weigh out strengths and weaknesses of each process.

Some elemental information about the dissertation in hand, such as the software used and the printing machine applied, as well as the related literature were briefly discussed in this chapter. Focus in this thesis is on the FFF process precision, a process which does not have a top position on the accuracy of various AM technologies. Shrinkage rate of specimens has been calculated via a mathematical model and shrinkage compensation method has been accordingly applied using the Grasshopper 3D software.

CHAPTER 3

SHRINKAGE COMPENSATION APPROACH

3.1 Introduction

This chapter deals with the underlying method used to overcome shrinkage in the FFF process. While in Section 3.2 of this Chapter, the core method to mitigate shrinkage is introduced from a geometrical standpoint, Section 3.3 is dedicated to the introduction of viscoelasticity, and choosing a proper viscoelastic model that would be capable of explaining the shrinkage behavior of filament. Discussion is then followed with a qualitative review in Section 3.5, as to how the chosen viscoelastic model operates in the course of print.

3.2 Geometrical Structure Used to Compensate Shrinkage

To test the shrinkage behavior of models, 2.5-dimensional parts with a hole positioned in their center are printed. A 2.5D body is a part whose one dimension is negligible compared to the other two dimensions. The perimeter of the hole is surrounded with a thin wall to separate the interior perforation from the surface around. Figure 3.1 illustrates, by way of example, two of many test cases printed.

For the central hole to undergo a minimal amount of shrinkage, linear 2.5D lines are printed, extending from the central hole perimeter to the outer surface wall. These line segments, which are henceforth referred to as *bridge lines*, are positioned perpendicular to the hole perimeter, as illustrated in Figure 3.1a.

These bridge lines, upon shrinkage, tend to shrink toward their center[74]. Likewise,

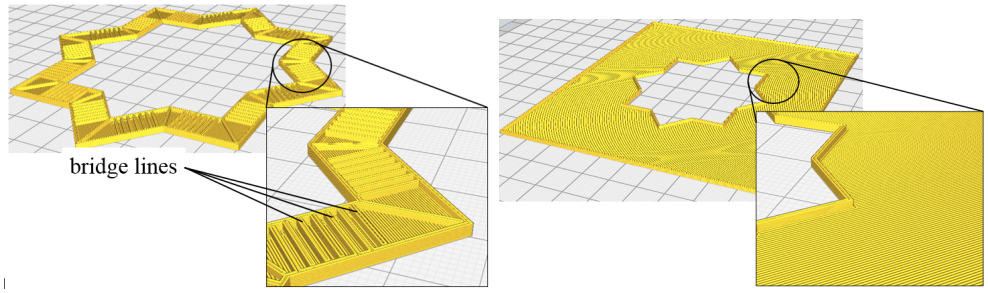

(a) (b)

Figure 3.1: Sample specimens; with (a), and without (b) bridge lines

the shrinkage of a closed curve, i.e the interior hole in our case, tends to occur towards center. As a result, it is anticipated that the shrinkage of these bridge line segments will cause the perimeter of the hole to stretch out, and thus counterbalance the shrinkage of the hole dimensions. As such, in this geometrical configuration, shrinkage itself is utilized to make up for the hole accuracy problem.

As should already be clear, the shrinkage of the bridge line segments can be used as a factor to determine that of the interior hole. Put differently, to control the hole shrinkage, an understanding of the surrounding line segments' shrinkage mechanism seems necessary. The fundamentals of this mechanism is modelled in the next section.

3.3 Modelling Shrinkage of PLA Line Strips; Concepts and Variables

In order for the model to be fully grasped, a series of essential terminologies are presented below. Additional to those, parameters and concepts of concern that are found in the mathematical equations are also introduced.

The necessity of looking at the FFF printing process as one with viscoelastic properties arises when considering the constantly changing nature of filament as it cools down from above-transient temperatures to room temperatures. Throughout a full range of material behavior under loading conditions, three distinct levels of (visco-)elasticity can be assigned to materials.

Ideally elastic materials are those that tend to preserve energy under displaced state, and to use it to return to their initial state after load is removed. As a result, these

materials are of reversible shape change.

On the opposite end of elasticity range are ideally viscous materials which tend to lose, in form of heat, all the energy they gain throughout the displacement process, and therefore, cannot return to their original state. This irreversibility of shape shows itself in the tendency of these materials to finally take the shape of their container.

Viscoelasticity, by definition, is the trait of materials that exhibit both viscous and elastic behaviors when undergoing deformation. Viscoelastic response to (un)loading, therefore, includes a time-involving behavior, representing viscous, as well as an instantaneous shape change representing the elastic properties of the material. In addition, after stress is removed, a permanent displacement still inheres in the material structure due to viscous properties of the material. Figure 3.2 shows response of elastic, viscous and viscoelastic materials to a constant stress.

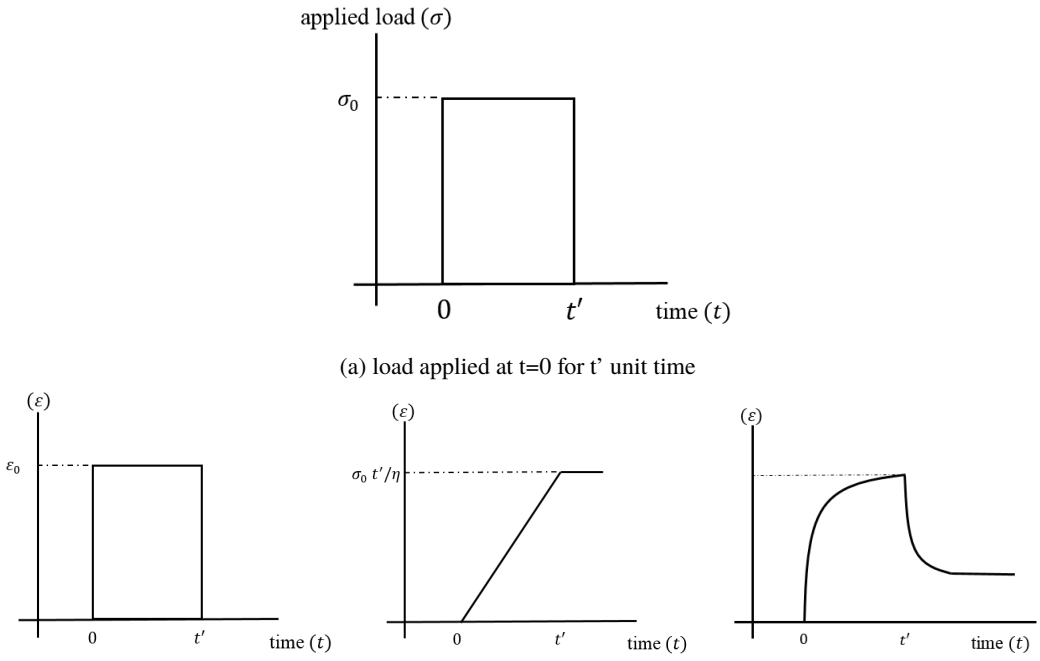

(a) load applied at t=0 for t' unit time

(b) ideally elastic (c) ideally viscous (d) viscoelastic

Figure 3.2: Response of different materials (a,b and c) to an instantaneous application of a stress at t=0 (a)

3.3.1 Creep and Stress Relaxation

The two most commonly discussed behaviors in viscoelastic materials are creep and stress relaxation. Creep occurs when stress is held constant, yet below the yield strength of the material, for extended period of time, leading to rise in strain over time. On a viscoelastic material, an external constant stress causes an initial instantaneous strain, a behavior that is characteristic of elastic solids. However, due to viscoelastic properties, the shape change is followed by additional strain if the load is maintained for a long enough time period (See Figure 3.3b).

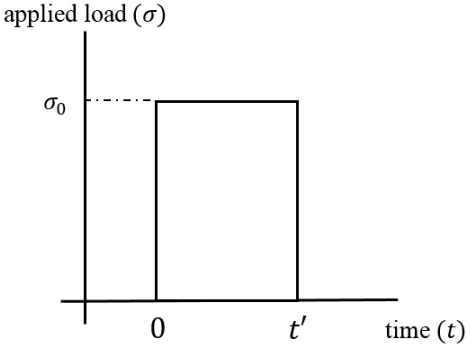

(a) load applied at t=0 for t' unit time

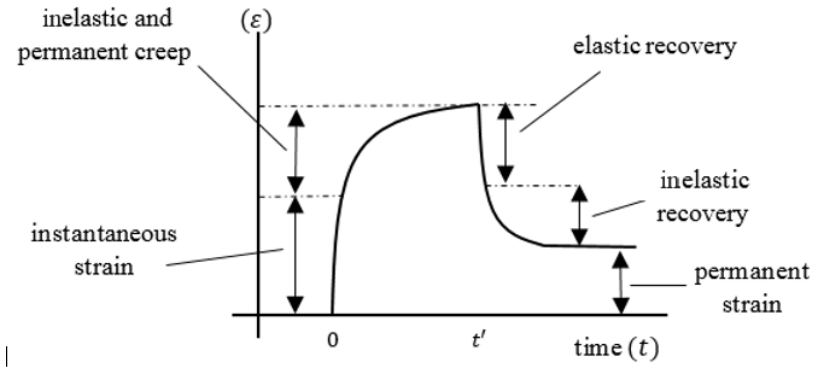

(b) viscoelastic response

Figure 3.3: Viscoelastic response to a constant load applied at $t = 0$ and removed at $t = t'$.

This time-dependent behavior whereby strain increases for a constant stress level is called creep. Under most practical conditions, although the strain increases, it does so with a decreasing rate. Upon unloading, part of the strain is also removed, as in elastic materials. The remaining goes for gradual recovery of strain, also known as anelastic, non-recovering or permanent strain.

The second phenomenon occurs if the strain is held constant for some long enough time span, leading to decline in stress levels with time. This phenomenon is called stress relaxation, as Figure 3.4b depicts. Another interpretation of this phenomenon can be seen in that the stress required for a viscoelastic solid to maintain constant strain decreases over time.

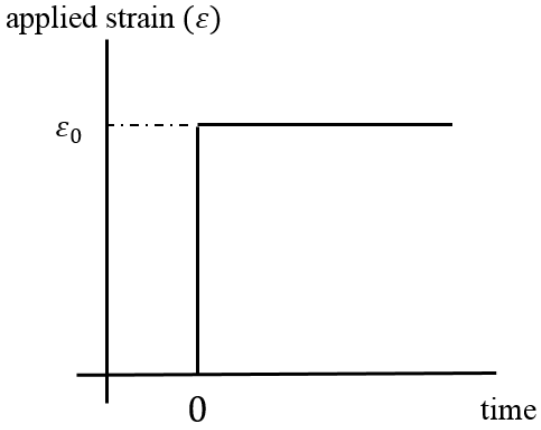

(a) constant strain applied

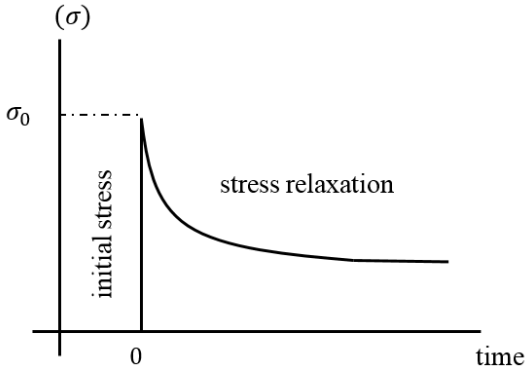

(b) stress relaxation, corresponding response to the constant strain ε_0

Figure 3.4: Viscoelastic response to a constant strain applied at $t = 0$

This should not be confused with creep, which is a constant state of stress with an increasing amount of strain.

3.4 Viscoelastic Models Relevant to This Thesis

As discussed before, ideally elastic materials do not resist shear loading, rather instantaneously deform when stretched, and thus their deformation is not time-dependent.

Contrarily, purely viscous materials resist shear forces and their response to stress is linear with time. As such, a purely elastic material would follow the Hooke's law:

$$\sigma = E\varepsilon \tag{3.1}$$

where E, with unit of $[Pa]$, is a material-specific constant called Young's modulus. However, a purely viscous material's strain would be time dependent:

$$\sigma = \eta \frac{d\varepsilon}{dt} \tag{3.2}$$

where η, with unit of $[Pa.s]$, is a material-specific constant called viscosity. Given Equations 3.1 and 3.2, an ideal elastic material can be represented by a spring, while an ideal viscous material may be reproduced by a dashpot.

Since a polymer material consists of molecular networks, it is necessary to consider their response to stresses as one with viscoelastic characteristics. In the FFF process, conditions are so that the polymer sticking to the platform is restrained by the print platform. In such a case, the polymer undergoes a phenomenon called stress relaxation. As the name implies, the stress generated this way in the polymer diminishes over time (Figure 3.4b).

As the mentioned figure suggests in a simplified fashion, a maximum amount of stress is seen on the material at the onset (t_0) of imposing the constant strain. As time goes on, however, the stress undergoes an exponential decline down to an equilibrium value, wherein the stress is no longer a considerable function of time.

Different forms of these two components can be used to account for viscoelastic materials' response. In order to describe the model used in this thesis, a few concepts need to be considered first.

3.4.1 The Maxwell Model; Concept of Stress Relaxation Time

A simple viscoelastic model is the Maxwell model (Figure 3.5), which combines in series a Hookean spring and a Newtonian dashpot. The spring component is in place to play the elastic or energetic part of the solid behavior, while the dashpot element

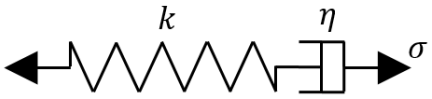

Figure 3.5: Maxwell Model

is to operate as the accommodating component. In any series arrangement like the Maxwell model, each element takes on a different strain, but similar stress amount. After a certain interval of time, the spring reaches its maximum amount. Strain and stress relationships governing the Maxwell model are thus presented in Equations 3.3 and 3.4 below.

$$\sigma = \sigma_s = \sigma_d \tag{3.3}$$

$$\varepsilon = \varepsilon_s + \varepsilon_d \tag{3.4}$$

To express the relationship in a single equation connecting the stress to the strain, from Equations 3.1, 3.2 and 3.4:

$$\dot{\varepsilon} = \dot{\varepsilon}_s + \dot{\varepsilon}_d = \frac{\dot{\sigma}}{E} + \frac{\sigma}{\eta} \tag{3.5}$$

which yields:

$$\sigma + \frac{\eta}{E}\dot{\sigma} = \eta\dot{\varepsilon} \tag{3.6}$$

Considering $\frac{\eta}{E} = \tau$, from Equation (3.6):

$$\frac{1}{\tau}\sigma + \dot{\sigma} = E\dot{\varepsilon} \tag{3.7}$$

For stress relaxation conditions wherein $\dot{\varepsilon} = 0$, Equation 3.7 will transform into

$$\dot{\sigma} = -\frac{1}{\tau}\sigma \tag{3.8}$$

Solving for σ yields:

$$\sigma(t) = \sigma_0 e^{-\frac{t}{\tau}} \tag{3.9}$$

Diagram corresponding to the Equation 3.9 is depicted in the Figure 3.4b shown earlier. The value $\tau = \frac{\eta}{E}$ is called stress relaxation time, with unit of $[s]$. As per Equation 3.9, the initial stress σ_0 will diminish to 0.367 its initial level at time τ; a benchmark feature used to determine stress relaxation time. Relaxation time is strongly dependent on temperature and other factors that affect the mobility of the material, and is roughly inverse to the rate of molecular motion.

To have a feel for the concept of relaxation time, for a constant stress, if τ is high, the material reaches its final strain status rapidly, and vice versa. It is also worth mentioning that above material glass transition temperature (T_g), τ is very short; below, it is longer.

In the FFF process, the PLA filament is primarily fused in the printer before being extruded from the nozzle onto the platform. The temperature variation of the polymer, therefore, ranges from above the polymer glass transition temperature down to room temperatures. As a result of this wide temperature variation, the filament sees different phases with various elasticity characteristics.

3.4.2 The Zener Model (Standard Linear Solid Model)

To account for the viscoelastic behavior of the printed filament under the thermal variations mentioned before, a three-element viscoelastic model, called the Zener model, or the Standard Linear Solid (SLS) model, is proposed (Refer to Figure 3.6).

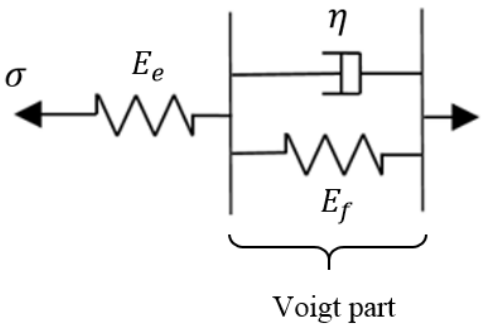

Figure 3.6: Zener Model

This model is comprised of the Voigt model, i.e. the parallel part, in conjunction with a spring put in series with it. The Voigt part is responsible for the viscous behavior

of the filament. This part of the model is in place because of the internal strains produced in the course of printing as a result of successive temperature alterations. In practice, repetitive cycles of cooling and heating that newly fabricated layers experience, generate internal stresses that can last for longer periods of time within the part, even after it is separated from the platform. This prolonged persistence of internal stresses is in large due to the fact that at temperatures lower than T_g, re-arrangement of polymer chains is not feasible. Contrarily, a purely elastic behavior, caused by loading or unloading of the printed body can be presented by a single spring placed in series with the other components.

From a mathematical viewpoint, equations pertaining to the Zener model will be discussed under Section 4.4.15 and its relevant subheadings. Prior to that, a qualitative analysis is offered in the next section.

3.5 Viscoelasticity of the FFF Print Phases; Qualitative Review

To cater the model for the FFF technology, it is worthy to note that the printed filament goes through three distinct phases of strain generation occurring from the onset of nozzle printing up to the point when the fabricated part is detached from the print tray, each with specific material characteristics. Figure 3.7 depicts these three phases in a general layout[60] (Please note that the three phases shown in the mentioned figure do not exactly represent temperature phases; For example, part of the viscoelastic changes occurring in temperature range between nozzle temperature, T_0, and filament glass transition temperature, T_g, is shown in Figure 3.7a, and part of it, in Figure 3.7b. For temperature-based classification of strains and stresses refer to Section 4.4.15.2.). In the mentioned figure, the matter of primary concern is the changes that the three components of the model, namely the elastic and viscous springs and the damper, experience throughout the printing process.

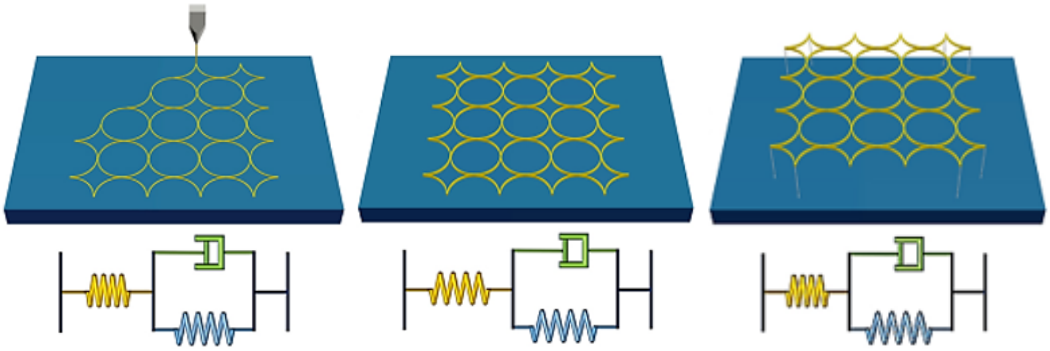

(a) Generation of internal strain due to nozzle travel speed

(b) Elastic and further internal strains are generated

(c) Elastic strain released due to detachment from the plate

Figure 3.7: Outline of viscoelastic changes involved in FFF[60]

Figure 3.7a pertains to the generation of internal strain as a result of nozzle speed only. Accordingly, the nozzle travelling with speed v causes a corresponding internal strain. This can be seen in the partial expansion of the viscoelastic spring, (E_f), positioned in parallel with the damper. The mentioned internal strain further augments as a result of temperature decline from nozzle temperature, T_0, down to T_g, as seen in more expansion of the parallel part in Figure 3.7b.

As for the elastic spring, it expands as a result of temperature decrease from T_0 to T_g, on the one hand, and from T_g to room temperature, T_r, on the other, (See Figure 3.7b).

As long as the viscoelastic portion of the model is considered, part of the thermal energy from newly deposited layers is transferred to the lower films of the printed body. Hence, more internal strain is generated within the part. All this is true for the circumstances wherein the model is still in temperatures higher than glass transition temperature, T_g. Once the printed body cools down to lower than T_g, further loss of temperature causes the printed part, which is still sticking to the print platform, to store elastic strain.

Figure 3.7c is associated with the detachment of the part from the print tray once the part has fully cooled down. The internal characteristics of the part remain intact during this stage, as clear from the parallel part, the dash-pot, η, and spring, E_f, having remained at the same energy level as that of the second phase. Yet, upon detachment, the printed body is freed from the platform restriction and thus releases

elastic energy in the form of instantaneous expansion of the part. This is represented in loss of energy seen in the elastic spring, E_e.

Like stated earlier, a qualitative analysis of the print process, as well as value assignments for parameters will be presented in Section 4.4.15.

3.6 Closure

In the light of the explanations given above, the Zener viscoelastic model is needed to account for the shrinkage phenomenon of FFF filament. Therefore, such a model, that serves as a platform to calculate the strain rate of PLA filament, will be presented in the next chapter. Moreover, the generation of a geometrical structure that suits shrinkage compensation scenario is also required. The process through which such a structure is automatically created is the focus of Chapter 4.

CHAPTER 4

ALGORITHMIC MODELLING

4.1 Introduction

Grasshopper 3D, the visual coding computer software developed for Rhinoceros 3D CAD software, is used to produce the geometrical structures to be printed based on the shrinkage compensation approach. The algorithm, developed via this software, can be considered as one with two distinct functions; on the one hand, a network of interconnected components that are in place to generate the final geometrical structure, suitable for shrinkage compensation approach, and on the other, a mathematical model that is to predict the strain associated with filament shrinkage.

The first part comprises of various groups of components interconnected to one another in a way that the final 2.5D model composes of the central hole, bridge lines connecting the hole to its offset, and the peripheral wall (See Figure 4.1). The model can adapt automatically, i.e. without manual interference, to various shapes designated to the interior hole. This is elaborated on in subheadings under Section 4.3.

As for the second part, the mathematical model is a series of equations representing the shrinkage rate of the interior line segments. As discussed earlier, these bridge lines serve to alleviate the shrinkage of the central opening (See figure 4.1). In tight connection with the mathematical model, is another series of components that form the basis for predicting shrinkage compensation outcomes (Full details can be found in Section 4.4.16).

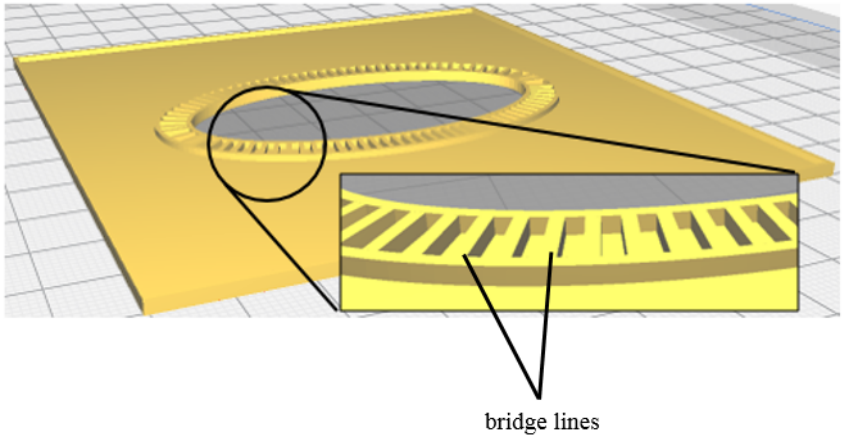

Figure 4.1: Internal hole and bridge lines

4.2 Development of the Model

From a general perspective, the algorithmic definition develops from identifying geometrically important points on the interior hole, to creating bridge lines, and to offsetting those lines, prior to extrusion. Alternatively, there can be considered four levels of geometrical elements present in the algorithm; namely, points, lines, surfaces (i.e. offsets) and volumes (extrusions). Each one is discussed below:

a) Points are categorized into three main types, that is, smooth edges, named *apexes*, sharp edges, named *vertices* and *regular points*. Points named apexes represent smooth turns of the central hole curve (See Figure 4.2). The second group are geometrical vertices. Regular points, in contrast, are those placed on the central hole curve at every certain distance and under defined set of conditions. The algorithm can immediately derive the first two sets from the curve geometry. Vertices and apexes are collectively referred to as *special points*.

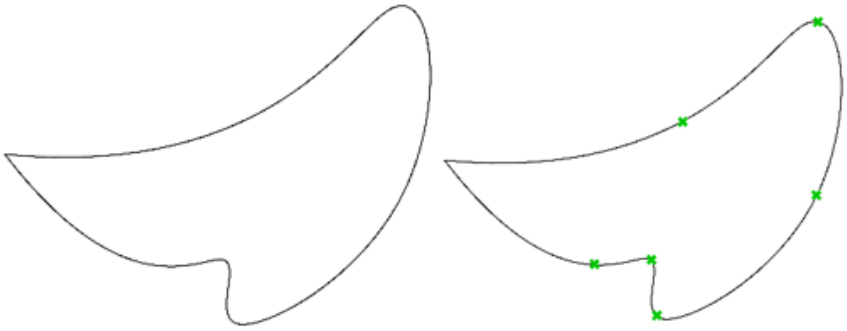

Figure 4.2: apexes of a sample curve (shown in green)

b) Corresponding to the three types of points introduced above, bridge lines from each type of points are defined in three categories, namely, lines from apexes, from vertices and from regular points. Therefore, *apex lines*, *vertex lines* and *regular lines* refer to lines running from apexes, vertices and regular points, respectively (See figure 4.3).

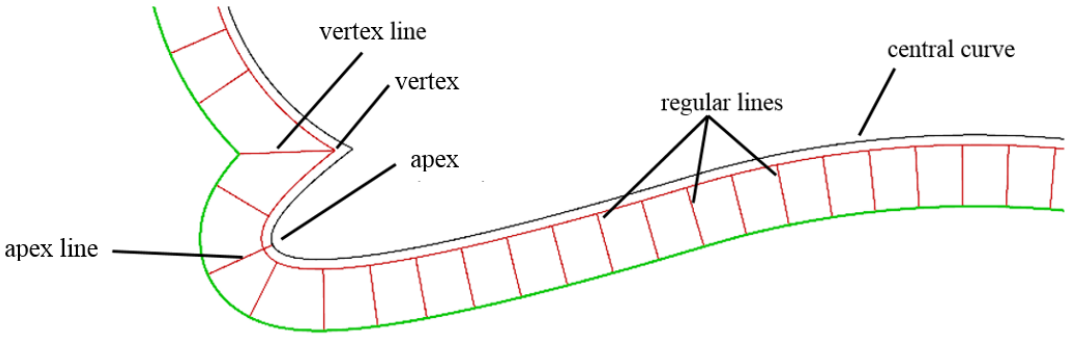

Figure 4.3: Different types of lines are named after the corresponding type of point.

c) Later in the algorithm, bridge lines are offset in order to create the base surface of bridge lines. Similar to the terminology mentioned above, three types of *vertex offsets*, *apex offsets* and *regular offsets* will be available, as depicted in Figure 4.4.

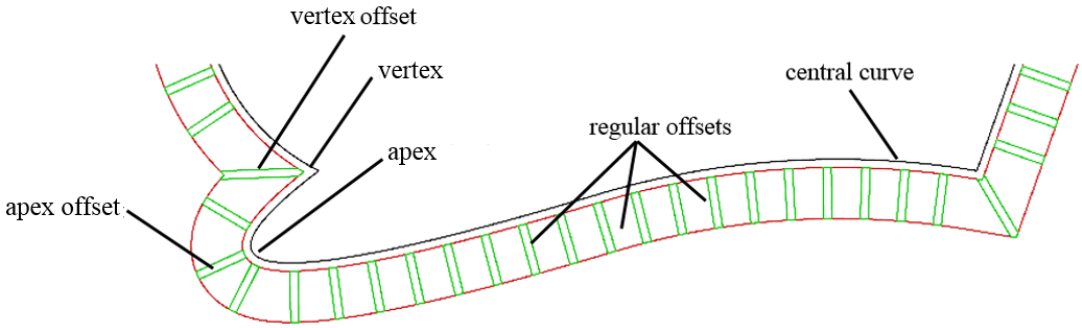

Figure 4.4: Different types of offsets are named after the corresponding type of point.

d) Obviously, *volumes* are 3-dimensional extrusions of the offset areas.

4.3 Arrangement of the Algorithm

As can be seen from Figure 4.5, the entire algorithm is divided into various groups of components based on the purpose each one serves.

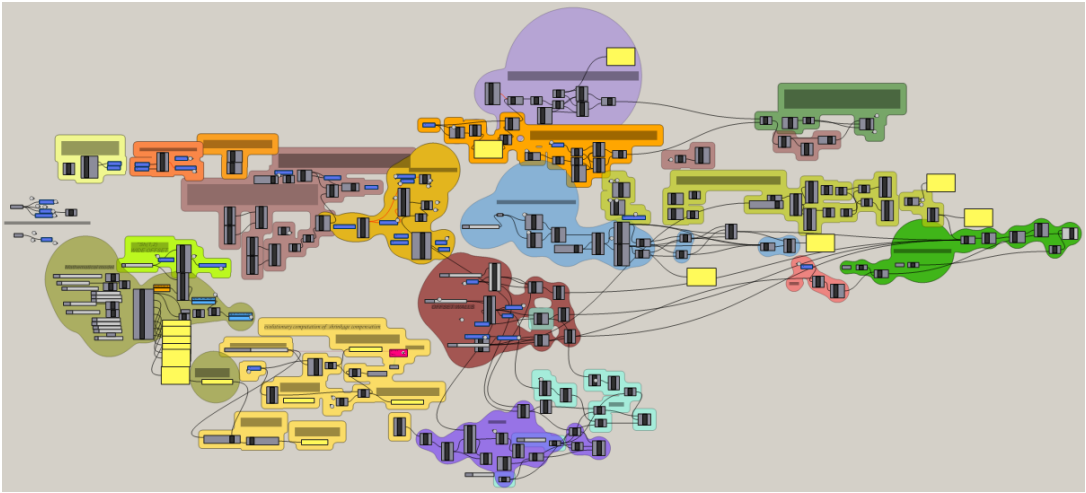

Figure 4.5: Algorithm map; The model is color-classified based on functionality.

Not all elements depicted in Figure 4.5 are individual components but are occasionally clusters of components. Clusters, in their own turn, include a number of components gathered together. Different groups of components are introduced below based on their function, input and output, and how each one contributes to the whole network

of connections.

For the reader to more easily comprehend the definition map, a few hints are listed in the following section.

4.3.1 Visual Hints on the Algorithm Map

Colors

In the visual definition represented in Figure 4.5, different groups are represented by different colors and are separated based on their functions. Some particular components have roles to play at more than one single group, hence share corresponding colors of both groups.

Codings

Codings are scripts mainly combined of letters and figures, assigned to each group of components (See Figure 4.6). The primary purpose of devising these scripts on each group is to readily indicate the type of ultimate output each group generates (i.e. point, line, etc), and at what stage of development that group is functioning.

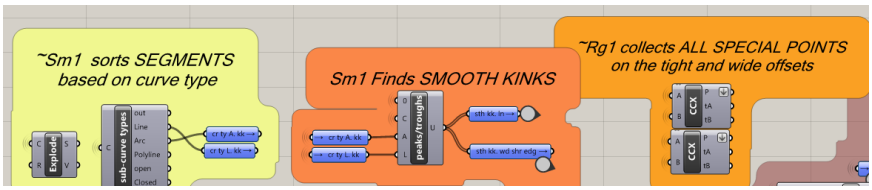

Figure 4.6: Sample codings, indicating a general function of the group

It is worth noting that since different groups can have more or less the same function and purpose, more than one group can share the same coding. As such, codes are not to serve as names for groups. Codings are listed in Table 4.1.

Based on the legend offered in Table 4.1, implications of the sample codings shown in Figure 4.6 are as shown in Table 4.2:

Table 4.1: Algorithm coding legend

Code	Code Description
Apx	apex
Vtx	vertex
Rg	regular
∼	prerequisite for
1	point
2	line
3	offset surface
4	extrusion
P	peripheral curve
Rh	fed from Rhinoceros 3D

Table 4.2: Description of the sample codings shown in Figure 4.6

Code	Code Description
∼Apx1	prerequisite for finding apexes
Apx1	finds apexes
∼Rg1	prerequisite for generating regular points

Group Names and Descriptions

A brief description of each group is given in its description balloon (See Figure 4.6). Group names are usually selected from descriptions and are put in capital letters. This is done to identify each group in the explanations given in Section 4.4 below.

4.4 Groups of Components and Their Functions

Below are explained characteristics of different groups of components existing in the model. Descriptions are titled by the name of the group followed by the relevant code in parentheses. A final product of the algorithm is already shown in Figure 4.1. Each of the following subsections elaborates on specific step of the production procedure

until the ultimate model is printable.

A flowchart summarizing the major stages of the algorithm is shown in Figure 4.7.

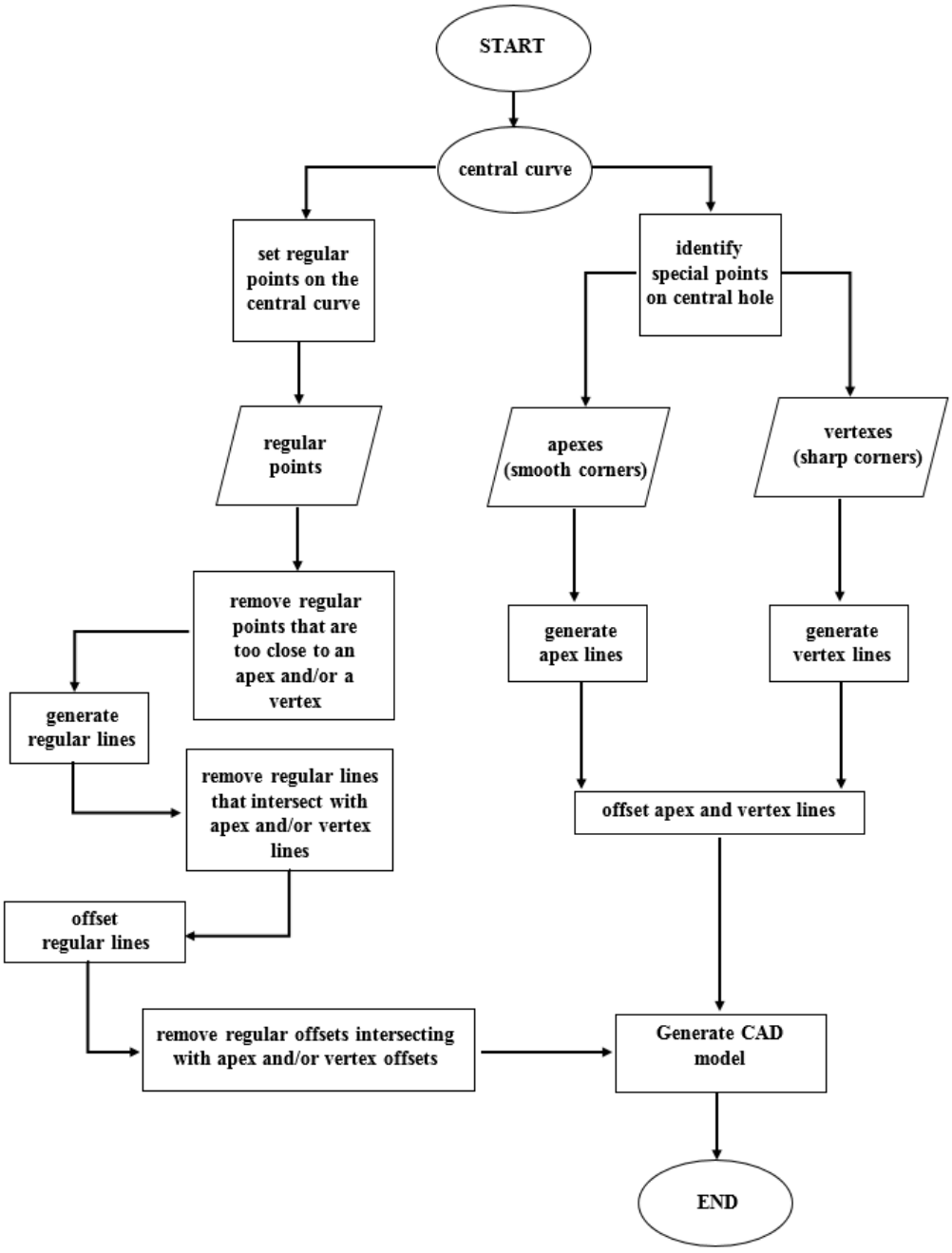

Figure 4.7: Flowchart of algorithm

4.4.1 Central Hole Curve or Original Curve (Rh)

The perimeter of the interior hole (See Figure 4.8), already produced in Rhinoceros 3D canvas, is referred to from the Grasshopper 3D environment, so that further operations can be carried out on the geometry in the plug-in environment.

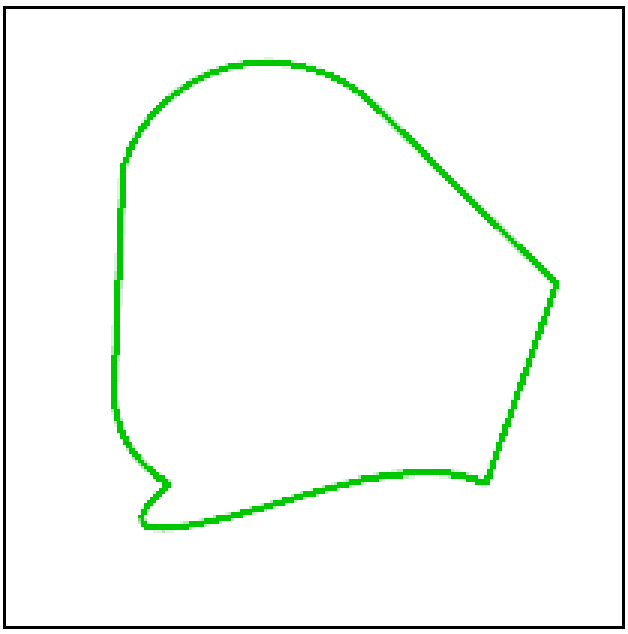

Figure 4.8: Central curve (in green) surrounded by the peripheral curve (black)

operates on 2D geometrical curve representing the central hole geometry existing in Rhinoceros 3D

generates corresponding geometrical curve workable from the Grasshopper 3D environment

4.4.2 Peripheral Curve (P)

The peripheral curve, in conjunction with its offset, composes the outer / peripheral wall of the printed part (See Figure 4.9).

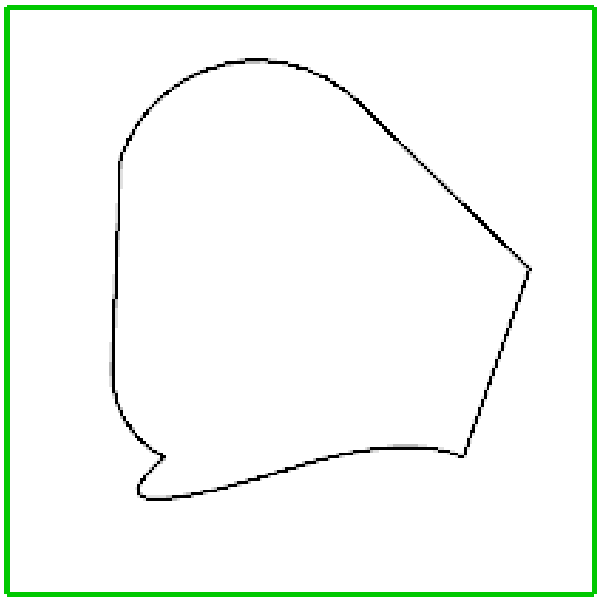

Figure 4.9: Peripheral curve (in green) surrounding the central hole (black)

operates on the curve representing the perimeter of the 2.5D model

generates corresponding geometrical curve workable from the Grasshopper 3D environment

4.4.3 Curve Classifier ($\sim$ Apx1)

This network of elements is designed to divide the original curve into its constituent segments based on geometrical types of each segment (See Figures 4.10 and 4.11). As far as this dissertation is considered, in particular, this is done to find the arcs and straight lines of the original geometry.

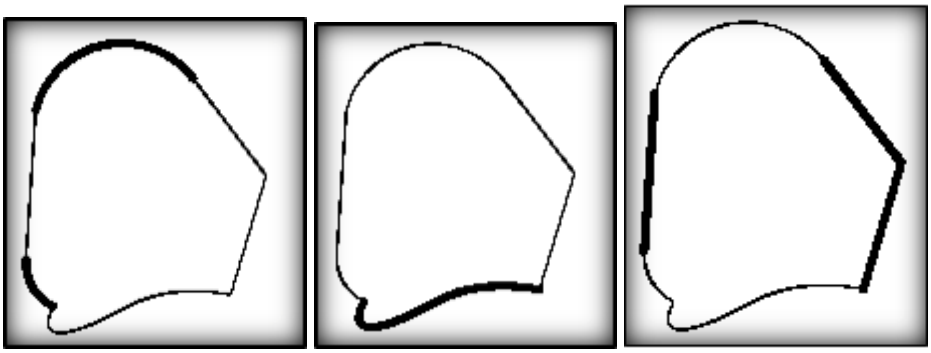

(a) Arcs (b) Curved lines (c) Straight lines

Figure 4.10: The interior curve is broken down to its sub-curve types

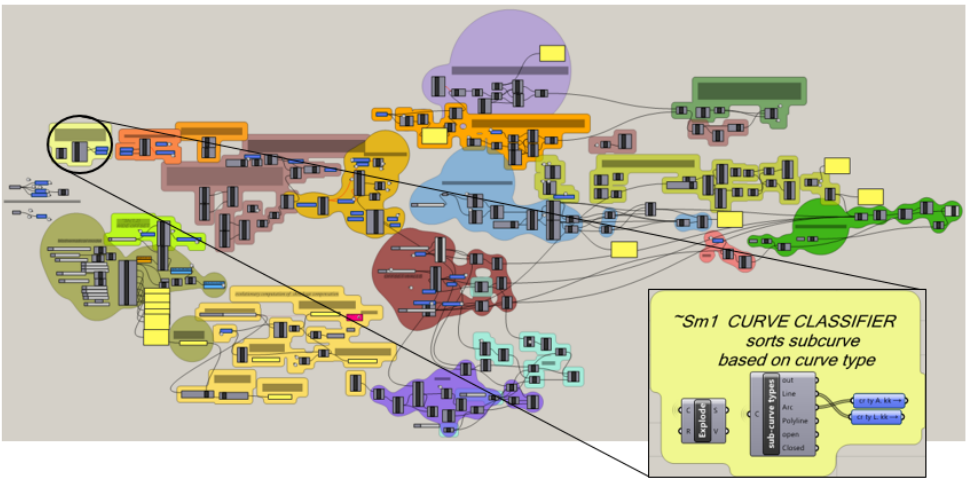

Figure 4.11: Location of the group in the definition

operates on the original curve

identifies segments of the curve based on their geometrical features (i.e. lines, arcs, curved lines)

contributes to removing of potentially fake peaks and troughs recognized on the original curve in the *apex finder*.

4.4.4 Apex Finder (Apx1)

This component finds the acute turns in the original curve, both concave and convex ones, as shown in Figures 4.12 and 4.13. These are determined using an algorithm inside the components cluster.

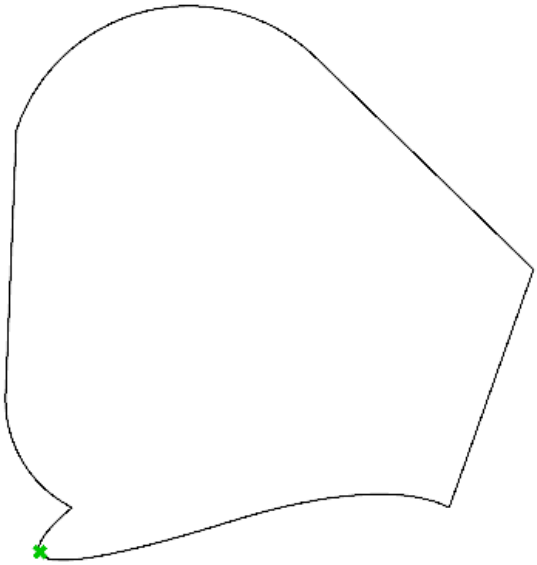

Figure 4.12: Apexes (green point) of interior hole are found, to make sure a line runs exactly from the apex point

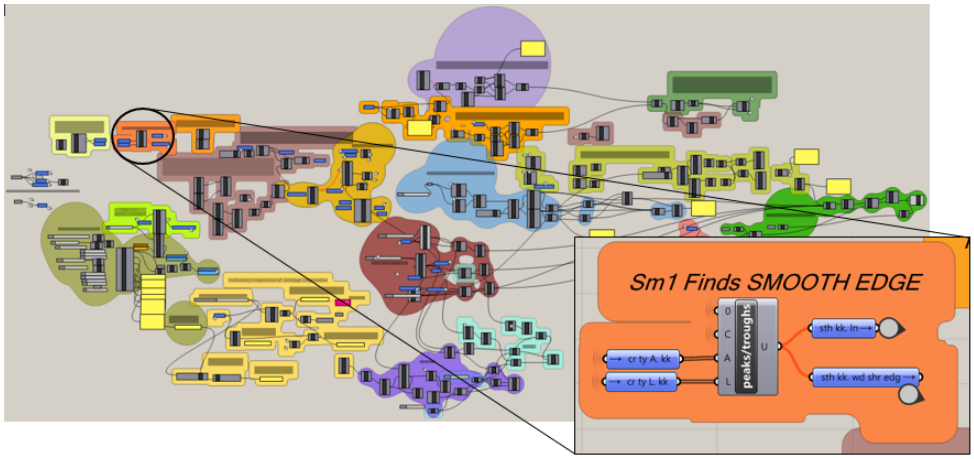

Figure 4.13: Location of the group in the definition

operates on the central curve

identifies peaks and valleys of the central curve

contributes to generation of lines running from apexes and locating corresponding apex points on the wide offset

4.4.5 Wide Offset (∼ Vtx (1,2))

The original curve is offset (See Figures 4.14 and 4.15). This is named a wide offset as it is farther from the interior hole curve compared to the tight offset.

operates on the original curve

generates wider offset of the curve

mainly contributes to trimming of vertex lines' offsets

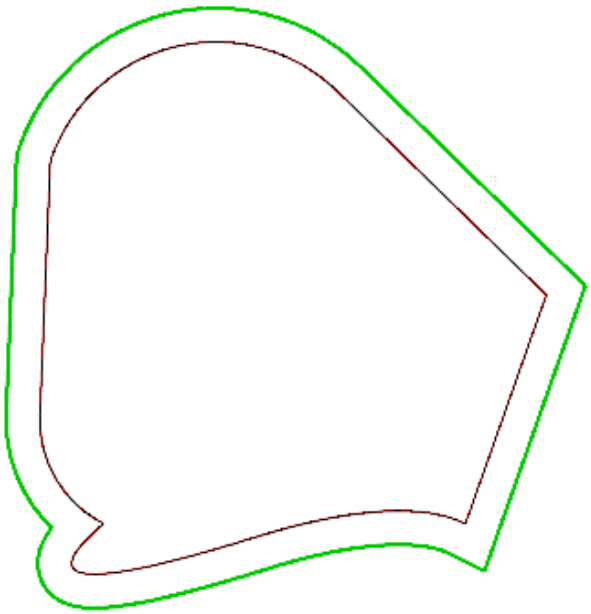

Figure 4.14: Wide offset of the interior hole

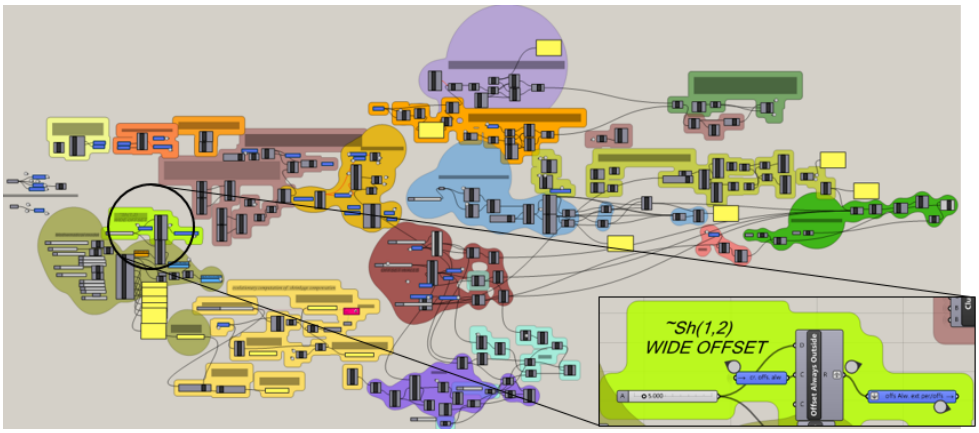

Figure 4.15: Location of the group in the definition

4.4.6 All Special Points (∼ Rg1)

generates special points on the original curve's tight and wide offsets, as shown in Figures 4.16 and 4.17. The tight offset is produced in the *offset walls* group.

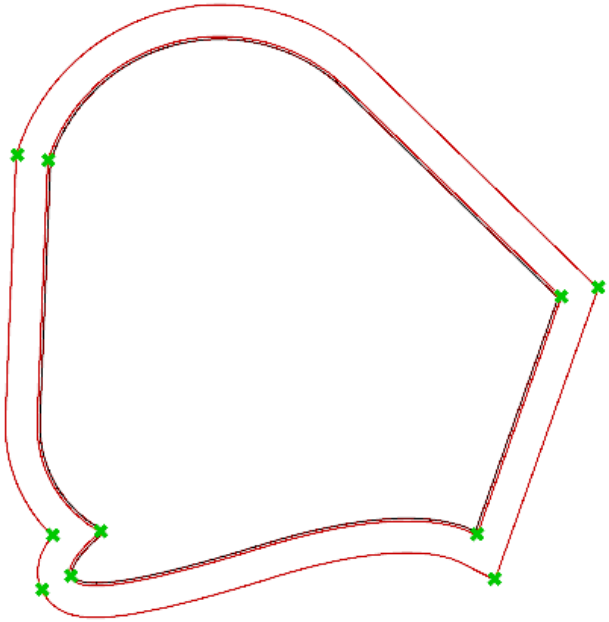

Figure 4.16: Special points are set on both offsets

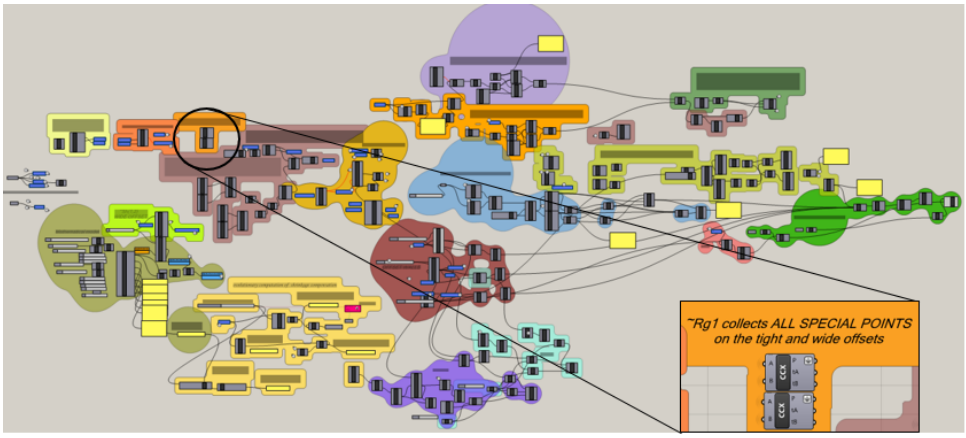

Figure 4.17: Location of the group in the definition

operates on apex and vertex lines and the corresponding offset of the original curve

identifies a collection of special points

contributes to refinement of regular points done in a *regular points filter* group.

These points include both vertices and the apexes.

4.4.7 Regular Points Refinement (Rg1)

A series of regular points are set on the tight offset at certain distance from each other using the group shown in Figure 4.21. The refinement of regular points is shown in Figure 4.18. This distance is defined primarily based on the supposed line offset distances. To elaborate, if each regular line is to have offset lines with a distance of d on either side, to avoid line offset intersection between offsets of such lines, a minimum distance of $2d$ between regular points is required. This is implemented in the algorithm.

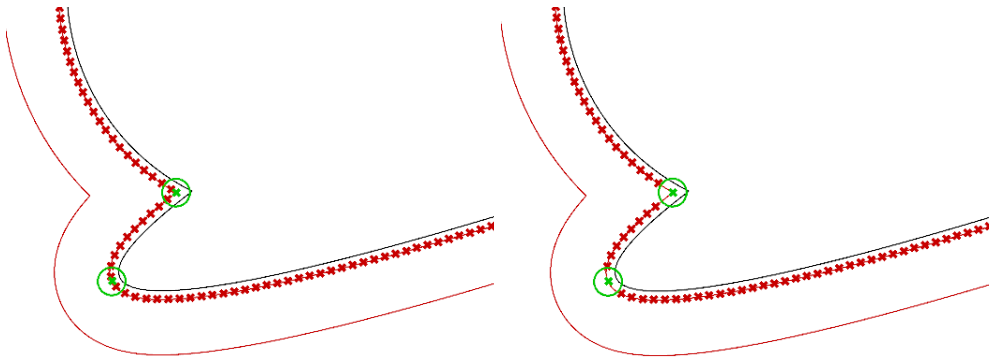

(a) Regular points (red) before refinement (b) Regular points after refinement

Figure 4.18: Regular points that fall within the circular areas (green) of special points are omitted

Since this arrangement of regular points is done with no regard to the location of the special points, some regular points happen to fall too close to the special spots, hence causing problematic line intersections or offset overlaps. To avoid this, and to satisfy the condition that special points should be maintained anyway, circles around special points are produced. These circles are used to omit all regular points that are too close, and thus fall within the circles. This process of filtering is carried out on the central curve's both tight and wide offsets. The criterion based on which a such circle's radius is defined can be explained according to Figure 4.19.

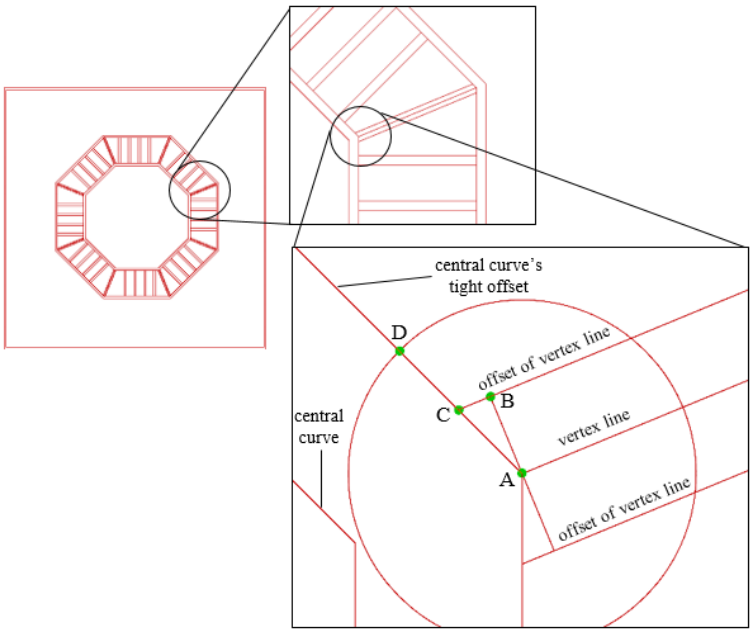

Figure 4.19: Geometrical method for determining radius of barring circles

Figure 4.20: A safety distance equal to a regular line's offset distance is added to the barring circle to avoid overlapping of offset areas.

Based on Figure 4.19, it is clear that point A represents a vertex, hence the center of the barring circle. Point C denotes the intersection spot of the offset of the vertex line and the central curve's tight offset. Point D denotes the intersection point of the barring circle and the tight offset of the central curve.

To obtain the radius of the circle, the distance between A and C, $\bar{AC}$, should be first calculated. This is done using the Pythagoras relationship. The distance between A and B, $\bar{AB}$, is already known, being equal to the vertex line's offset distance, which is manually defined in the algorithm ($0.4[mm]$ in all the specimens). As for $\bar{BC}$, the distance is obtained using the length component of the Grasshopper 3D. Thus $\bar{AC}$ is calculated. However, as is apparent from the figure, the radius is chosen to be larger than $\bar{AC}$ by a length equal to $\bar{CD}$. The distance $\bar{CD}$ is actually equal to a regular line's offset from the line itself (Similar to $\bar{AB}$ for the vertex line). The extra distance of $\bar{CD}$ is in place to ensure that a regular line's offset area will not overlap with that of a vertex line. Figure 4.20 depicts how a worst, yet allowable case would look like. It is evident from the mentioned figure that if the regular line, L_r, moved inside the barring circle, the offset of the regular line, L'_r would cross the vertex offset line, L_v. In such a case, the barring circle wipes out the relevant regular point, and the corresponding regular line and both its offsets are not generated. One important point to remember here is that this filtering method is geometry-adaptable. In other words, if the vertex angle changes, the BC distance would increase, and so does the AC length. This would result in corresponding change in the circle radius. For acuter angles, the barring circle's radius would be more larger than the $\bar{AC}$ length; for obtuser angles, the radius would come closer to the $\bar{AC}$ distance.

Since every regular line is made from connecting a regular point on the central curve's tight offset to its corresponding point on the wide offset, equal number of regular points should be set on each of the tight and the wide offsets. Obviously, however, the refinement system implemented by the omitting circles can leave different number of regular points on each offset, as a result of geometrical characteristics of the offset curves. This problem is tackled in the *regular lines refinement* group.

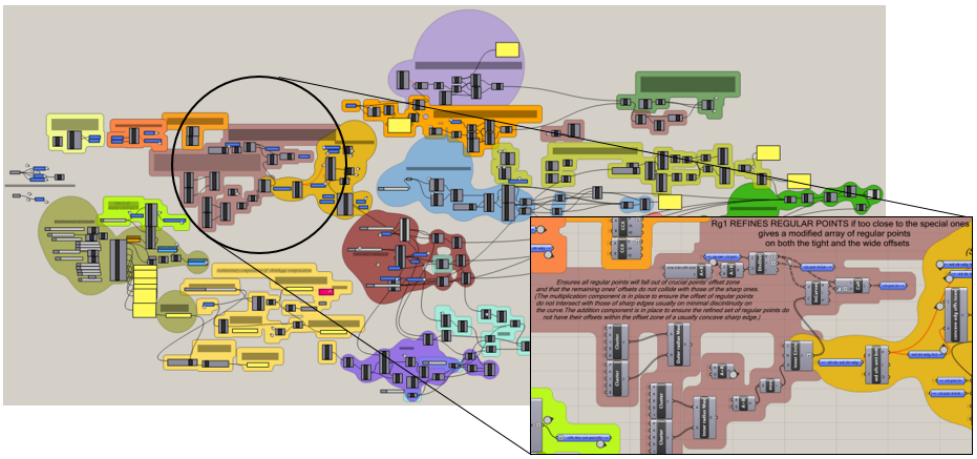

Figure 4.21: Location of the group in the definition

Apart from these two cases, other intersection types can also occur, which can be sorted out either by the circles in this group or via other refinement groups of components.

4.4.8 Lines ((Apx, Vtx)2 and (∼ Rg2))

With regard to the classification of points, three corresponding classes of lines running from regular points, apexes or vertices are consequently produced (Figures 4.22 and 4.23). This group of components thus

operates on points of a specific type

generates lines

contributes to refinement of regular offsets that have intersections with special offsets

It is noteworthy that the basis for regular line generation is the regular points distributed on the tight offset, not those on the wide one.

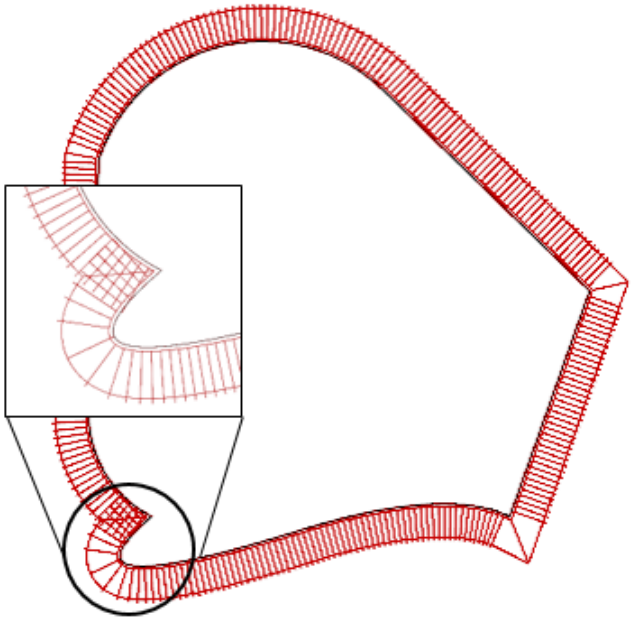

Figure 4.22: Lines of all types are generated. Since intersecting regular lines are not fully filtered, some make collisions at special corners.

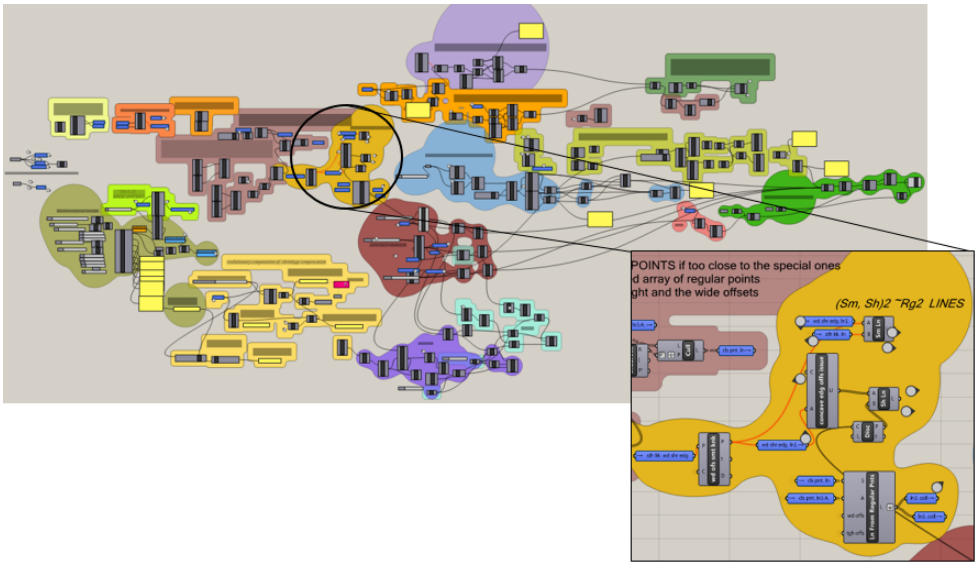

Figure 4.23: Location of the group in the definition

In Sections 4.4.9 and 4.4.10 groups in which regular lines have been refined against offset areas of apex and vertex lines are discussed, respectively.

4.4.9 Regular Line vs. Apex Offset Refinement (∼Rg2)

This group gives regular lines that do not cross apex offset regions. Since this set of regular lines are not tested against vertex offsets, there may be lines among them crossing offsets of vertex lines. An example of such refinement is depicted in Figure 4.24. In this figure, the curve is illustrated in black, and the tight and wide offsets in red. This group (shown in Figure 4.25) thus

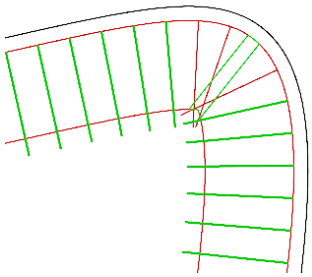

Figure 4.24: Regular lines filtered at apex corners; Desired lines (green) are maintained and colliding lines (red) are removed from the final set of regular lines.

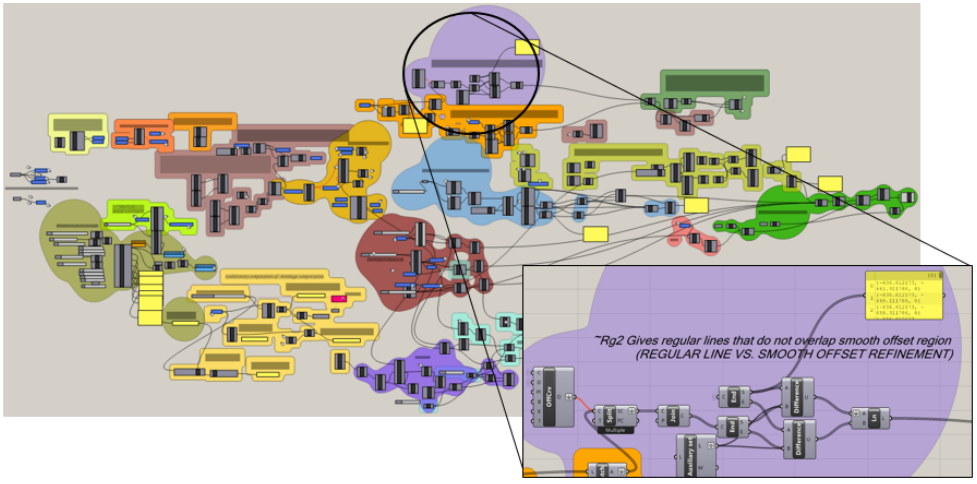

Figure 4.25: Location of the group in the definition

operates on regular lines and apex offsets

generates set of regular lines non-colliding with apex lines

contributes to refinement of regular offsets that have intersections with special offsets

4.4.10 Regular Line vs. Vertex Offset Refinement (∼Rg2)

This group gives regular lines whose offsets have no intersection with vertex lines or their offsets, as shown in Figures 4.26 and 4.27.

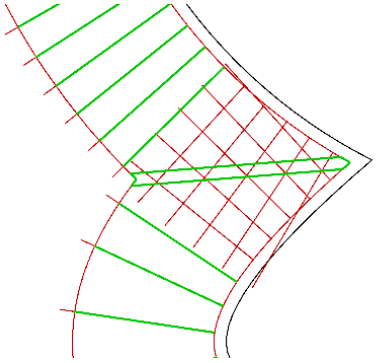

Figure 4.26: Regular lines filtered at vertex corners; Desired lines (in green) are maintained and others (in red) are removed from the final set of regular lines

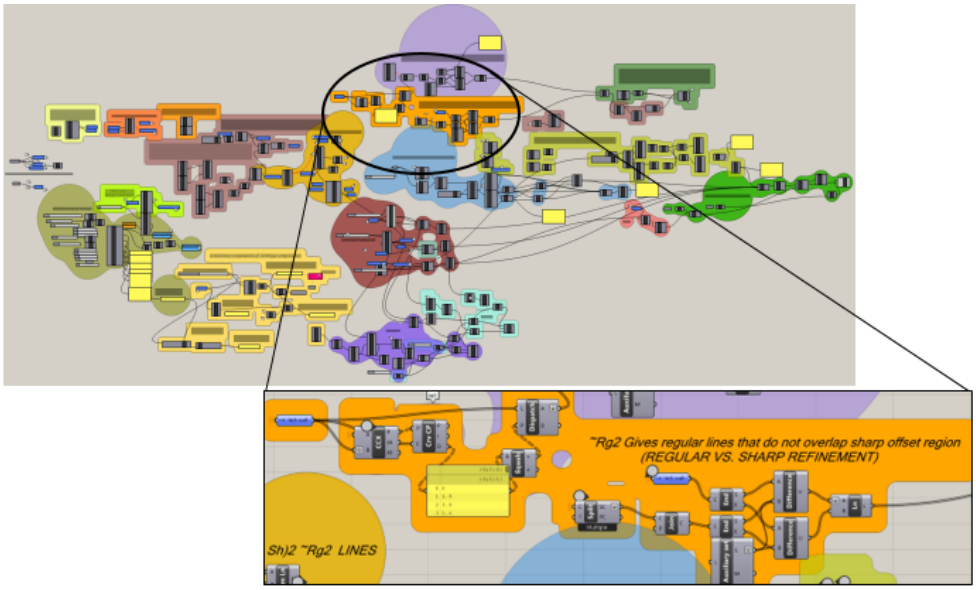

Figure 4.27: Location of the group in the definition

operates on regular lines and vertex offsets

generates set of regular lines non-colliding with vertex lines

contributes to forming a collection of regular lines that have no intersection with offset regions of special lines

4.4.11 Regular Line Filter on Wide Offset (Rg2)

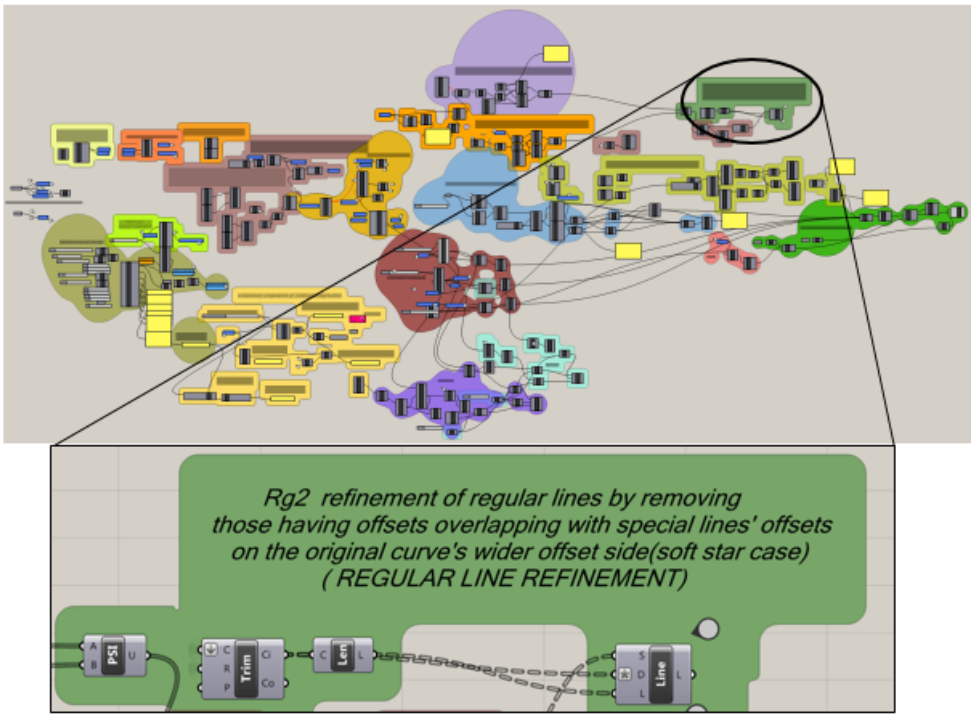

Figure 4.28: Location of the group in the definition

The collection of regular lines obtained from the previous refinement stages need to be further filtered in this stage. This is because in the earlier refinement stages, regular lines were drawn based on points on the tight offset only. Therefore, the generated regular lines are not still tested for intersection on the wide offset curve. In other words, although the possibility for these lines to interfere with offset regions is ruled out already, there can still arise cases wherein regular offsets can overlap with banned areas near the wide offset curve. This makes it necessary to cull regular lines a step further. This is done in the group shown in Figure 4.28, i.e *regular line refinement*, via the culling circles on the wide offset. A case in point can be seen in Figure 4.29 where the remaining regular lines still suffer from the prohibited overlaps. In the mentioned figure, the central curve is depicted in black. As is clear from the figure, the banned circular area on the vertex excludes one single line. The point worthy of attention here is that the line does not overlap with the vertex offset area, and therefore is not removed in the previous refining stages. However, since it falls within the circular banned area, it is needs to be removed.

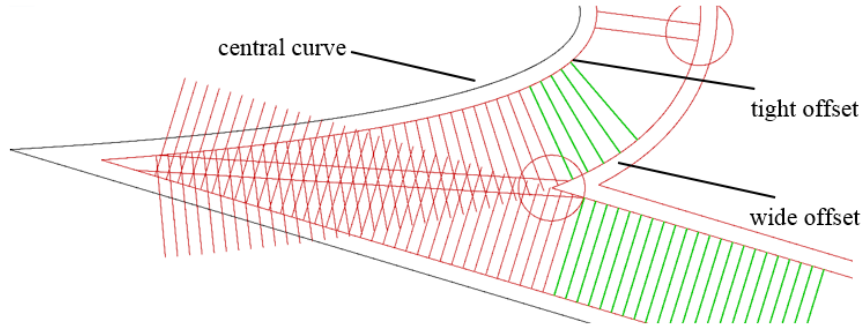

(a) Regular lines before refinement on the wide offset curve

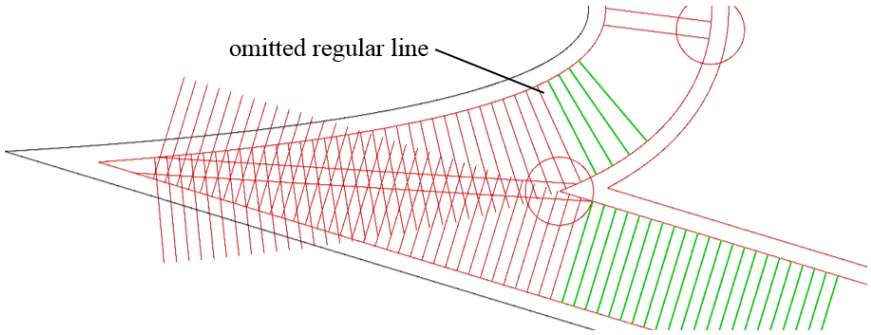

(b) Regular lines after refinement on the wide offset curve

Figure 4.29: Refinement of regular lines is completed by weeding out the problematic ones on the wider offset curve.

operates on the forbidden circular area of the wider offset and on the set of regular points that are partly refined already

generates set of regular lines non-colliding with vertex lines

contributes to offsetting of regular lines

4.4.12 Regular Offset Organizer (Rg3)

This group offsets regular lines. The offsetting mechanism makes sure that, firstly, the offsets are within the region between the interior curve and the widest offset, and hence do not come short or fall out of the desired region. Secondly, this array of components ensures that the final offset region takes the form of the surrounding curves on both its ends, as presented in Figure 4.30. This feature takes on added importance when regular lines are to connect a non-straight central curve to its offset. In such a case,

the regular line tips need to take a curved shape to adapt to the curve geometry. This group's location is seen in Figure 4.31.

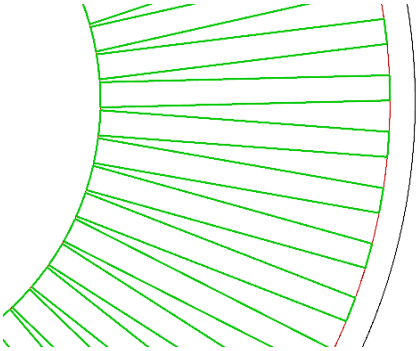

Figure 4.30: Each of the offsets areas of regular lines (shown as green rectangular-like areas) takes a curved form on its both width ends to fully adapt to the surrounding geometries.

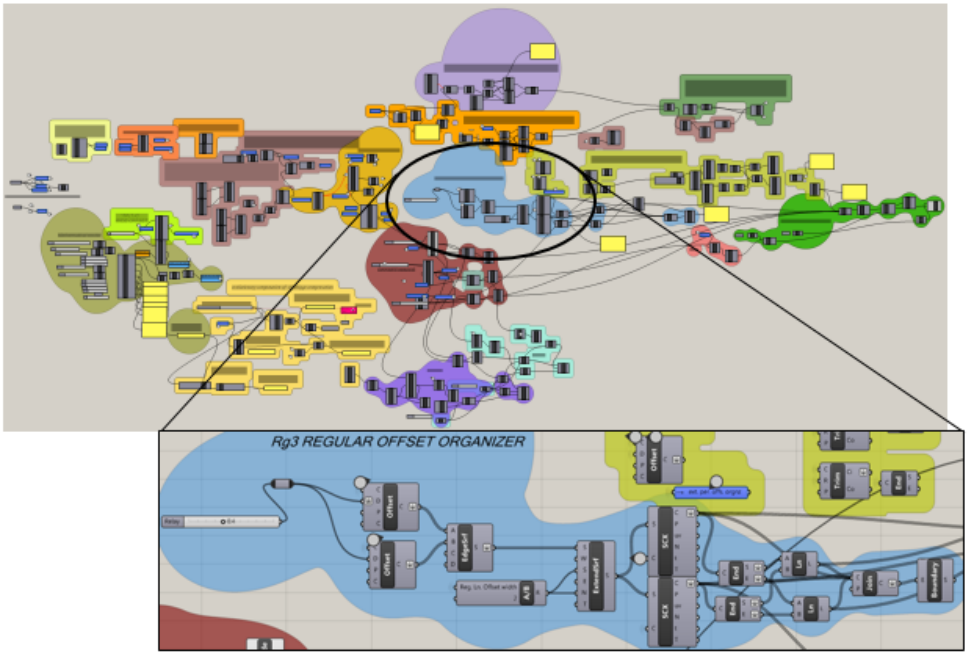

Figure 4.31: Location of the group in the definition

operates on the completely refined lines

generates offsets inscribed based on the curves geometrical features

contributes to extrusion of resulting offset surfaces

4.4.13 Special Offset Organizer((Apx, Vtx)3)

This group offsets special lines and ensures the produced offset regions are in geometrical coincidence at their width side with the tight and the wide offset curves (See Figure 4.32). Therefore, these offset regions are not plain rectangles, but are refined to coincide with the geometry of the tight and the wide offset curves. This group's location can be seen in Figure 4.33.

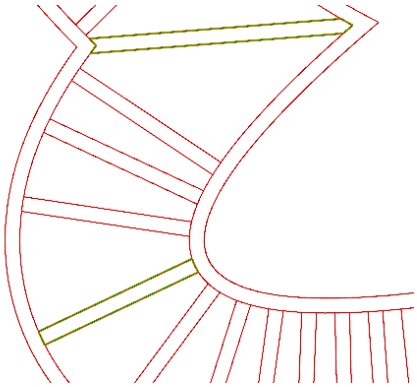

Figure 4.32: Special vertex and apex offset regions (green), are aligned with the interior curve offsets to coincide with the geometry of the surrounding curves.

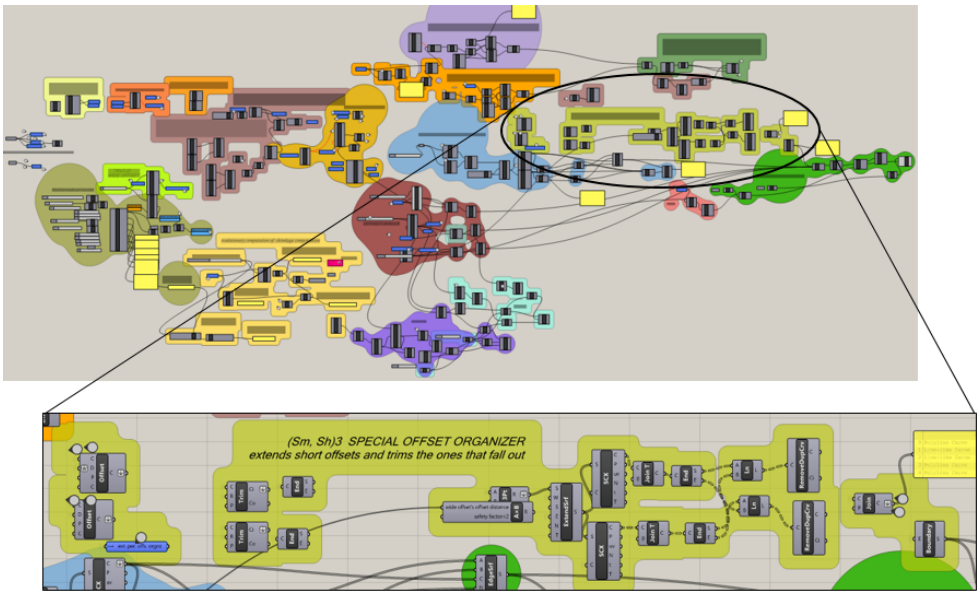

Figure 4.33: Location of the group in the definition

operates on vertex and apex lines

generates offsets in accordance with geometrical characteristics surrounding the offset

contributes to extrusion of resulting offset surfaces

4.4.14 Generation of Shrinkage Compensation Model ((Apx, Vtx, Rg)4)

This set of components (Figure 4.34) generates three surfaces. The first one is the surface between the original curve and its tight offset, the second being the region between the wide offset and its offset curve, and the third being the peripheral region. These surfaces actually represent the walls of the actual 2.5D model once extruded, as depicted in Figure 4.35.

Apart from the walls, a base surface is also extruded that covers the lowest part of the model except for the interior hole area. The base actually covers the bottom area between the interior hole walls and the peripheral wall.

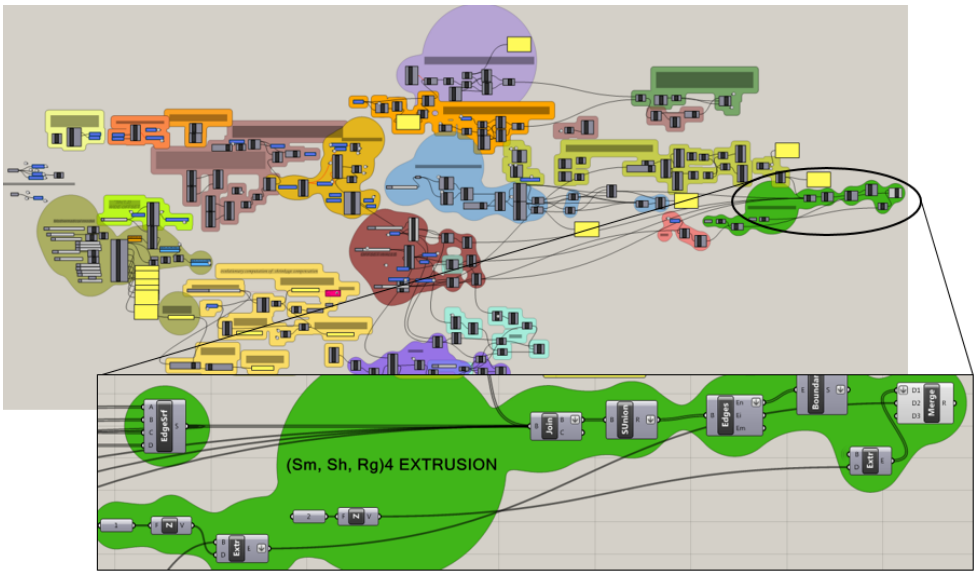

Figure 4.34: Location of the group in the definition

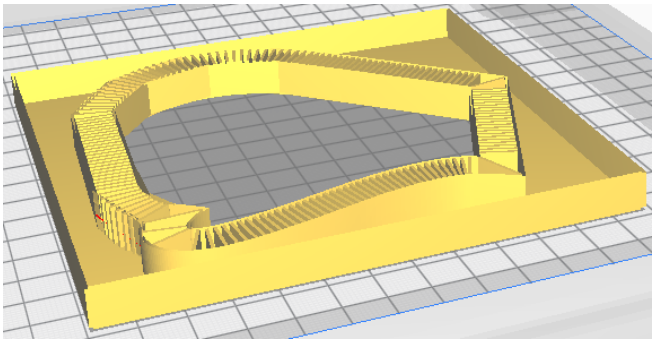

Figure 4.35: A sample final 2.5D specimen

4.4.15 Mathematical Model

The set of components in this group simulates the mathematical shrinkage expected from the polymer under certain set of circumstances. To that end, mathematical equations governing the shrinkage mechanism have been Python-coded in form of a group of building blocks (Figure 4.36). To obtain such equations, however, first, a look into the physics of the print process seems necessary.

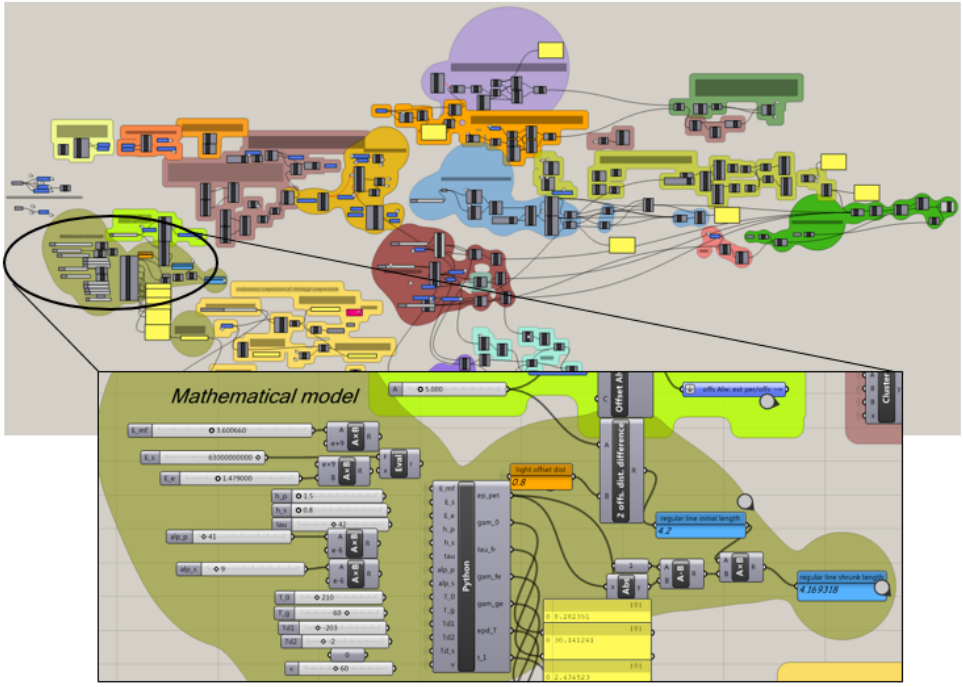

Figure 4.36: Location of the group in the definition

4.4.15.1 Physical Conditions and Assumptions

A few points on physical assumptions and experimental settings are necessary at this stage to mention as follows[60]:

a) As stated earlier in Section 3.4.2, the viscoelastic model used to simulate shrinkage mechanism of the polymer is the Zener model (See Figure 3.6 for the model).

b) The elastic modulus, E_e as well as the relaxation time τ_f of the filament is constant for temperatures over T_g. The elastic modulus E_e stands for the capacity of a material to store energy elastically, and applies to both the glassy and rubbery states, i.e. below and above transition temperature T_g.

c) The elastic modulus of the printer platform, E_s, is also constant for the entire temperature spectrum.

d) The strain internally stored in the print material due to the nozzle travel speed is taken as a constant value, ε_0

e) The printed part decreases in temperature with a constant rate of $\dot{T}_1$ for temperatures above T_g, and a constant rate of $\dot{T}_2$ for temperatures below.

f) Material of the build plate of the Ultimaker 3 Extended is tempered glass.

The ultimate goal of this section is to obtain a mathematical relationship that offers the total strain of the polymer after the specimen cools down to room temperature , T_r.

Apart from the assumptions cited above, no specific considerations regarding the model of the printer and/or filament manufacturer have been taken into account in organizing the equations.

Moreover, to approach the model from a quantitative viewpoint, it is reasonable to break down the process with respect to the temperature shifts discussed earlier[60]. There will be thus three temperature spectra:

First Cooling Phase: $T_g < T < T_0$

It is noteworthy that the filament extruded from the nozzle is of the temperature T_0 before it cools down to T_g, the glass transition temperature. As stated in the assumptions section, this temperature drop is assumed to take place linearly, i.e. at a constant rate, $\dot{T}_1$.

Equilibrium equations for the polymer-platform surface is governed by the equation[60]:

$$\sigma_p h_p = -\sigma_s h_s \tag{4.1}$$

where h_p and h_s are respectively the height of polymer strip and build tray thickness.

From the Zener model presented in Figure 3.6, the total stress, σ, is equally tolerated by either of the series parts. Thus, taking $\sigma = \sigma_p$:

$$\sigma_p = \sigma_e = \sigma_f + \sigma_\eta \tag{4.2}$$

Likewise, from the same figure, the total strain imposed on the entire model is distributed between the two series parts of the model. Therefore, the total strain is equal to the sum of the strains tolerated by the elastic spring, E_e, and the Voigt part:

$$\varepsilon_p = \varepsilon_{pe} + \varepsilon_{pf} = \varepsilon_{pe} + \varepsilon_\eta \tag{4.3}$$

Given the structure of the Zener model, the same strain is expected for parallel components, namely the spring E_f and the dashpot. Thus, in the Equation 4.3, $\varepsilon_{fp} = \varepsilon_\eta$.

On the other hand, the constitutive relations reveal:

$$\sigma_f = E_{mf}\varepsilon_{pf} \tag{4.4}$$

$$\sigma_\eta = \eta_m \dot{\varepsilon}_\eta \tag{4.5}$$

$$\sigma_e = E_e \varepsilon_{pe} \tag{4.6}$$

$$\sigma_s = E_s \varepsilon_s \tag{4.7}$$

The parameter E_{mf} in Equation 4.4 is the mean modulus of the spring E_f for temperatures above T_g, and is of the unit $[Pa]$. The need to determine a mean value is because the mentioned spring's modulus is a function of temperature, above T_g. The same is true for the mean viscosity of the dashpot, η_m, $[Pa.s]$, found in Equation 4.5. These two parameters will be drawn later using the cross-WLF equation.

The parameter E_e, $[Pa]$, found in Equation 4.6 is the modulus of the elastic spring above glass transition temperature, T_g, and is assumed to be constant for this temperature range.

The parameter E_s, $[Pa]$, seen in Equation 4.7, is also constant for the entire experiment temperatures.

As can be seen from Equations 4.4 to 4.7, ε_{pf} and ε_{pe} are still unknown. To obtain an equation for these, it is helpful to resort to the cross-WLF equation for a polymer above its T_g to first find η_m and E_{mf}, and accordingly define ε_{pf} and $\dot{\varepsilon}_\eta$. The Cross-WLF viscosity model explains the temperature, shear rate, and pressure dependency of the viscosity and can be arranged by the following equation :

$$\eta_{(T)} = \eta_{(T')} e^{\frac{-17.4(T-T')}{51.6+T-T'}} \tag{4.8}$$

where $\eta_{(T')}$ is the polymer viscosity at a reference temperature, T', and is supposed to be known. Numerical constants found in Equation 4.8 are obtained from the supplementary notes to the Reference study [60]. In the case in question, the reference temperature is taken as the glass transition temperature, T_g.

The mean value of viscosity, η_m is obtained as follows:

$$\eta_m = \frac{1}{t}\left(\int_0^t \eta_{(t')} dt'\right) = \frac{\eta_{(T_g)}}{\Delta T}\left(\int_{T_0}^{T_0+\Delta T} e^{\frac{-17.4(T-T_g)}{51.6+T-T_g}} dT\right) \tag{4.9}$$

Accordingly:

$$E_{mf} = \frac{\eta_m}{\tau_f} \tag{4.10}$$

where τ_f, $[s]$, is the corresponding stress relaxation time for temperatures above T_g.

Equation concerning contact surfaces between the built plate and the polymer at temperatures above glass transition temperature is given as:

$$\varepsilon_p + \alpha_p \dot{T}_1 t = \varepsilon_s + \alpha_s \dot{T}_s t \tag{4.11}$$

Up to this point, seven independent unknowns and seven equations are ascertained; The seven independent unknowns are σ_e, σ_f, σ_η, σ_s, ε_{pe},ε_{pf} and ε_s. The unknowns σ_p and ε_{pe} are dependent as Equations 4.2 and 4.3 suggest. The seven equations are Equations 4.1, 4.2, and 4.4 to 4.7 as well as Equation 4.11. Solving this set of equations for ε_{pe} and ε_{pf} will result in [60]:

$$\varepsilon_{pe}(t) = \dot{\varepsilon}_T [\frac{\gamma_f \gamma_0}{1-\gamma_0} \tau_{fr} (e^{\frac{-t}{\tau_{fr}}} - 1) - (1 + \gamma_{fe}) t] \tag{4.12}$$

$$\varepsilon_{pf}(t) = -\dot{\varepsilon}_T [\tau_{fr} (e^{\frac{-t}{\tau_{fr}}} - 1) + t] \tag{4.13}$$

where

$$\gamma_{fe} = \frac{E_{mf}}{E_e} \tag{4.14}$$

$$\kappa = \frac{\alpha_s \dot{T}_s}{\alpha_p \dot{T}_1} \tag{4.15}$$

$$\gamma_f = \frac{E_{mf} h_p}{E_e h_s} \tag{4.16}$$

$$\gamma_0 = \frac{1}{1 + \gamma_{fe} + \gamma_f} \tag{4.17}$$

$$\tau_{fr} = (1 - \gamma_0) \tau_f \tag{4.18}$$

$$\dot{\varepsilon}_T = \alpha_p \dot{T}_1 (1-\kappa)\gamma_0 \tag{4.19}$$

All parameters introduced in Equations 4.14 to 4.17, are unitless. The units corresponding to parameters τ_{fr} and $\dot{\varepsilon}_T$ found in Equations 4.18 and 4.19, respectively, are $[s]$ and $[\frac{1}{s}]$.

Equations 4.12 and 4.13 give respectively the elastic and internal strain amounts of the polymer as it cools down from nozzle temperature, T_o, to the PLA glass transition temperature, T_g.

Parameters introduced in Equation 4.14 to 4.19 are arbitrary parameters already found in Equations 4.12. and 4.13. Some of these can be viewed as having physical interpretations. For instance, γ_{fe} (in Equation 4.14), indicates the tendency of polymer to store strain in elastic form. The larger γ_{fe} is, the larger E_{mf} would be (or smaller would E_e be), and due to Equations 4.4 and 4.6, for a given amount of stress, smaller internal strain, and larger elastic strain would be stored. Therefore, from a physical perspective, larger γ_{fe} suggests more inclination of the polymer to take up deformation in the form of elastic strain.

By the same token, larger κ (Equation 4.15) suggests the ratio of build plate strain rate to that of the polymer.

Second Cooling Phase: $T_r < T < T_g$

Once the temperature falls lower than T_g, the printed polymer acts as an elastic material, hence is governed by Hooke's law. The corresponding equations would then be as follows[60]:

$$\varepsilon_{pe}(t) = -\alpha_p \dot{T}_2 t \frac{1-\kappa}{1+\gamma_{ge}} \tag{4.20}$$

$$\varepsilon_{pf}(t) = 0 \tag{4.21}$$

where

$$\gamma_{ge} = \frac{E_{ge} h_p}{E_s h_s} \tag{4.22}$$

and is unitless. In Equation 4.22, E_{ge}, having the unit $[Pa]$, is the elastic modulus of spring E_e below transition temperature.

No internal strain is stored in the filament body at this stage due to low temperature. This is because in temperatures lower than T_g, polymer chains are prevented from recovering.

Third Phase: elastic strain released after detachment Once the specimen is removed from the build tray, the elastic strain, which is reserved in the specimen body as a result of attachment force, is released.

4.4.15.2 Numerical Substitutions for Physical Parameters

Numerical values for parameters found in Section 4.4.15.1 are referenced and discussed in the next paragraphs. This is done according to the temperature phases already laid out in the mentioned section.

For the First Phase Wherein $T_g < T < T_0$

a) To obtain E_{mf}, according to Equation 4.10, it is necessary to first determine η_m. Based on Reference [56], polymer viscosity at $100[^0C]$, i.e. at $373.15[K]$, is [54–56, 87]:

$$\eta_{(T=373.15[K])} = 3.31719[GPa.s] \tag{4.23}$$

Therefore, by substituting $T = 373.15[K]$ and $T' = T_g$ in Equation 4.8:

$$3.31719(10^9) = \eta_{(T_g)}(0.0005)$$

Therefore:

$$\eta_{(T_g)} = 6.66[TPa.s] \tag{4.24}$$

By having $\eta_{(T_g)}$, and considering that

$$\Delta T = T_g - T_0 = 60 - 210 = -150[^0C]$$

the mean viscosity of PLA above transition temperature is thus derivable from Equation 4.9 as:

$$\eta_m = \frac{6.66.10^{12}}{-150} \int_{60+273.15}^{210+273.15} e^{\frac{-17.4(T-333.15)}{51.6+T-333.15}} dT \tag{4.25}$$

which gives

$$\eta_m = 150.286452[GPa.s] \tag{4.26}$$

Given that $\tau_f = 42[s]$ [60] and using Equation 4.10, the following value is obtained:

$$E_{mf} = 3.5783[GPa] \tag{4.27}$$

b) As for elastic modulus of the build plate, E_s, the corresponding figure for tempered glass is determined as $63[GPa]$[12, 56].

c) The elastic spring's modulus, E_e is rated as large as 1.479 [GPa] [13, 57].

d) Values for polymer height and build plate thickness are respectively 0.06 and $20[mm]$.

e) Polymer and plate thermal expansion coefficients, α_p and α_s respectively, are considered to be constant and respectively equal to $41e^{-6}$ and $9\,e^{-6}$ $[\frac{1}{^0C}]$ [58, 85].

f) The build plate temperature, T_s, is set on 60 $[^0C]$, and thus the polymer temperature drops from $210[^0C]$ (nozzle temperature), to just above transition temperature, i.e. $60[^0C]$, and does so in a fraction of a second. As a result, numerical value for the temperature drop from nozzle temperature to glass transition temperature, $\dot{T}_1$, is set equal to -200 $[\frac{K}{s}]$.

For the Second Phase Wherein $T_r < T < T_g$

Like mentioned before, once the print is over, an amount of elastic strain is induced in the specimen by further loss of thermal energy associated with drop of temperature below T_g.

a) For this phase, polymer temperature drop rate, $\dot{T}_2$, is equal to $-2[\frac{K}{s}]$. The build plate temperature is constant, i.e $\dot{T}_s = 0[\frac{K}{s}]$.

b) E_{ge} is determined to be equal to $3.5[MPa][71]$.

For the Third Phase Wherein the Specimen is Detached from the Plate

The sum of Equations 4.12 and 4.20 give the overall elastic strains that the polymer undergoes between T_o and T_r. Thus, using the numerical values introduced in the previous sections, the resulting strain, ε_{pe}, is calculated to be around 0.73 percent. This is the strain that is released after the printed body is detached from the plate.

$$\varepsilon_{pe} = 0.0073 \tag{4.28}$$

4.4.16 Evolutionary Solution to Locate Proactive Curves

Once the shrinkage rate for a straight strip of line is obtained from the mathematical model, it is applied to the length of the central hole curve to yield the corresponding shrunk curve. This is done under the assumption that the strain for a closed curve perimeter is identical to that of a straight line. A shrunk curve obtained this way will have a perimeter less than the initial curve (Figure 4.37), and hence, will take a distance from the original curve position. This very distance offers a measurable quantity that will stand for the shrinkage of the original geometry after cooling down. Relevant test cases are examined and discussed in the following chapter.

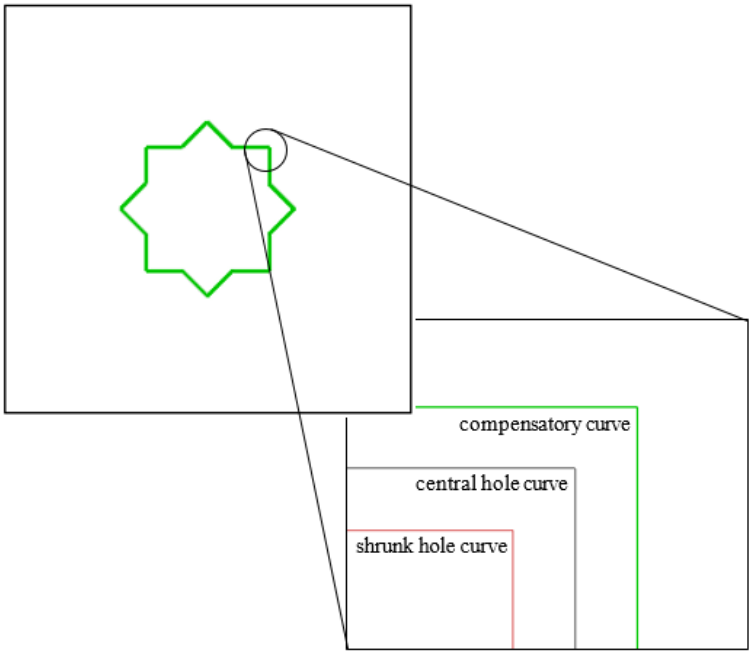

Figure 4.37: Central (black), shrunk (red) and compensatory (green) curves

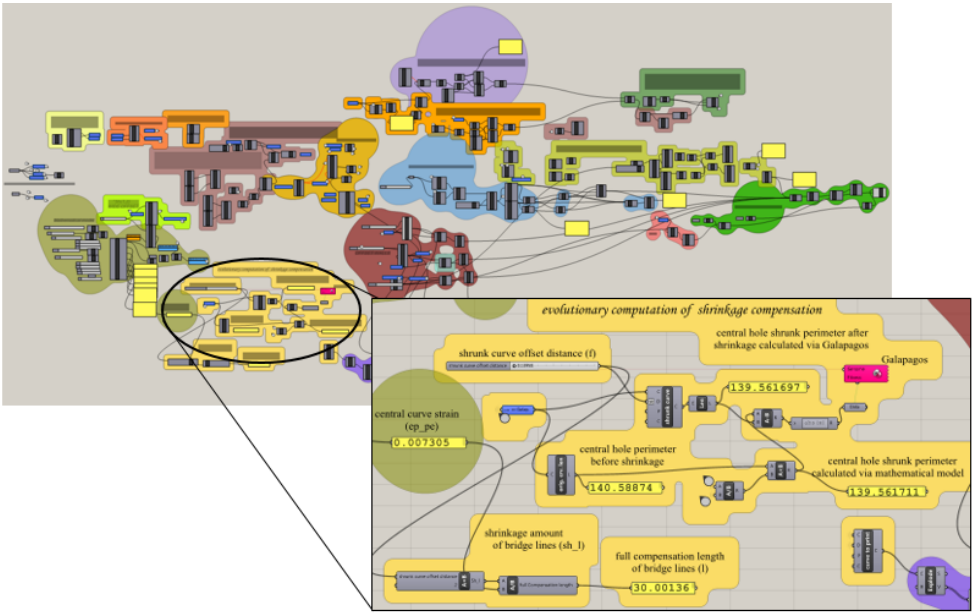

Figure 4.38: Location of the group in the definition

In an attempt to print a central hole curve that will shrink to desired dimensions (i.e. proactive curve), the strain rate mentioned above is inversely applied to the central curve perimeter to give the compensatory curve (Figure 4.37) perimeter.

What is known about the compensatory curve at this stage is its perimeter. The

distance at which this curve with its known perimeter stands from the central curve is derived via evolutionary calculation. This calculation is done by the Galapagos component (Figure 4.38). The working mechanism of this component is based on consecutive optimizations. For the case at hand, Galapagos tests a range of curves with different distances from the original central curve, and chooses the one that has minimum difference in perimeter from that of the original geometry. Related test cases are discussed in the following chapter.

Based on the classification of the algorithm explained so far, a general layout of the algorithm can be presented in Figure 4.39.

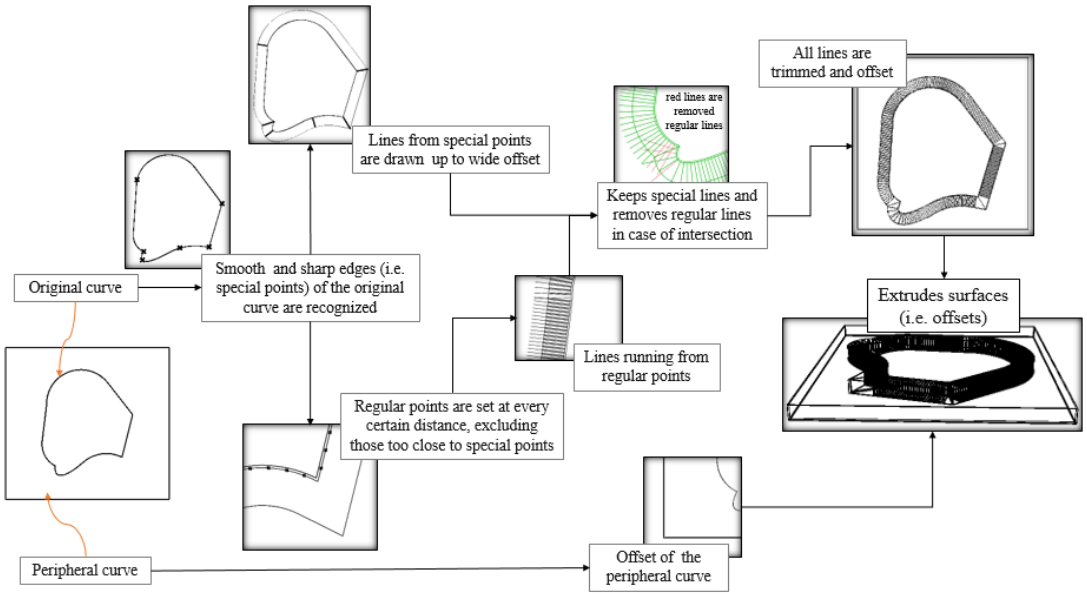

Figure 4.39: Schematic outline of development stages of the algorithm

4.5 Closure

A detailed outline of the shrinkage compensation structure generated via Grasshopper 3D was put forward in this chapter. The final strain rate obtained from the mathematical model was also calculated. In order to prove the models and calculations introduced in this chapter, test cases are designed for their internal hole shrinkages. It is worth paying attention that three types of test cases are to be examined in Chapter 5, two of which being those discussed under Section 4.4.16, and the third one being the shrinkage compensation structure previously discussed in Section 4.4.14. Test cases, test settings

and relevant results are discussed in more depth in the following chapter.

CHAPTER 5

TEST CASES

5.1 Introduction

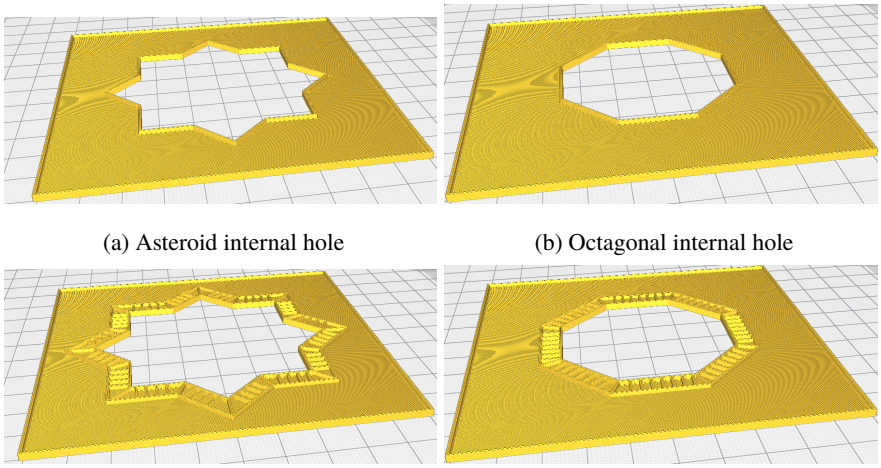

(a) Asteroid internal hole

(b) Octagonal internal hole

(c) Asteroid hole with bridge lines

(d) Octagonal hole with bridge lines

(e) Sample real asteroid specimen

(f) Sample real octagon specimen

Figure 5.1: General structure of sample test cases

To assess the validity of the method presented so far, two structures with an interior hole are printed. Geometrical characteristics of the central hole for the first case can be considered as two overlapping squares, as shown in Figure 5.1a, thus making an asteroid geometry, and for the second case, as a regular octagon (Figure 5.1b). Real images of the corresponding specimens are shown in Figures 5.1e and 5.1f. These two models are then set to be surrounded by auxiliary lines (Figure 5.1c and 5.1d) to make up the test cases of this thesis (For more detailed changes in test cases, see Section 5.6.1).

5.2 Experimental Settings and Anticipated Error Sources

The experimental settings under which all the parts are printed are presented in Table 5.1. These data are actually part of those introduced to the mathematical model.

Table 5.1: Experimental settings for printing test cases

experiment factor	**description**
filament material	white PLA
nozzle temperature	210 ^0C
build platform temperature	60 ^0C
print speed	60 mm/sec
infill rate	60%
specimen wall thickness	0.8 mm

Although the settings mentioned above are to theoretically yield the most accurate outcomes, there are a few known sources of imperfection that can potentially affect the final results. These are listed and briefly discussed below.

a) A major source of geometrical disparity can stem from the print G-codes. Accordingly, the G-codes, which define the nozzle travel path, would inevitably define the temperature gradients that are not evenly distributed all over a single layer in the course of printing. As a result, the temperature decline rate which is considered to be constant, is not exactly so in practice.

b) Measurements, not unlike any other geometrical analysis, are not ideally reproducible, in the sense that repeating the same measurement will most likely give slightly different outcome. This deviation, however, is supposed to be within an acceptable range.

c) Print quality is also another source of error, based on which the minor surface disparities can occur. Such sources of disparities can make themselves felt in the form of relatively large deviations from the average, in other words as outlying data. Such a source of error can take added significance when the measurement tool is unable to sit on the true surface of the model, which can be the case with the CMM probe.

d) Even in the ideal set of conditions wherein print-induced imperfections are absent, surface roughness can arise as a similar concern too, especially if no post-treatment of material is carried out on the specimen.

5.2.1 Considerations on Caliper Accuracy

A caliper is a device used to measure the distance between two opposing sides of an object. Many types of calipers permit reading out a measurement on a ruled scale, a dial, or a digital display.The tool used to measure test case dimensions is a digital caliper.

Regarding the precision measurement of a caliper, two accuracy indexes have been reported[89], called the *partial surface contact error*, E, and the *scale shift error*, S. The partial surface contact error, applies to any measurements made using the outside measuring faces, and the scale shift error applies to measurements using any other measuring faces available on the caliper, such as inside, step, and depth measurement In case of measurements performed in this thesis, the central holes' dimensions are measured using the inside jaws, and thus the scale shift error is pertinent. The uncertainty related to this jaw of caliper is reported to be ± 0.002[mm][91].

5.2.2 Considerations on CMM Accuracy

To determine axial accuracy of CMM machines with contact probing systems, the ISO 10360-2 standard is used. According to this standards system, the axial accuracy of a CMM machine follows the Equation below.

$$A = a + Lb \tag{5.1}$$

In the equation above, A, with $[\mu m]$ unit, represents the accuracy of the CMM machine, a and b are empirically defined constants, and L, being of $[mm]$ unit, denotes the measuring range that the machine is used for. In case of this thesis, the CMM machine used is the DEA GLOBAL STATUS 777. For CMM measurements carried out in this thesis, for example, the accuracy equation has been determined using standardization tests to be:

$$A = 2.5 + \frac{4L}{1000} \tag{5.2}$$

Therefore, for measurements ranging around 50 millimeters, an accuracy of

$$L = 2.5 + \frac{4(50)}{1000} = 2.7[\mu m] \tag{5.3}$$

is expected. As such, all the measurement results for a decagonal hole with $50[mm]$ of length, will have a tolerance of $2.7[\mu m]$. Similarly, the corresponding accuracy for measurements ranging around $40[mm]$ will be:

$$L = 2.5 + \frac{4(40)}{1000} = 2.66[\mu m] \tag{5.4}$$

As explained in Chapter 3, the mathematical model is developed for investigating shrinkage of straight strips of lines. For this reason, as a basal experiment, a number of straight lines are printed so that the validity of the shrinkage model is examined.

After investigating the straight line shrinkage, in the first set of experiments, two more complicated shapes are tested for their strain rate. In the second array of tests, proactive designs are fabricated and put to test, while in the final step, the shrinkage of lines has been used as a solution for the shrinkage problem of parts with internal holes. These three experiment arrangements, i.e. tests on strain of internal holes, proactive tests, and shrinkage compensation tests are presented in the following sections.

5.3 Measurements of Shrinkage for Straight Line

The strain rates that are observed in these basic specimens need to fall in the same range of magnitude as that obtained in the mathematical model is approved. Table 5.2 shows the pre- and post-shrinkage lengths of a number of straight lines printed under the experimental circumstances introduced in Table 5.1.

Table 5.2: Strain rate for straight line test cases

pre-shrinkage length $[mm]$	post-shrinkage length $[mm]$	calculated strain rate
20	19.89	0.0055
30	29.82	0.0060
40	39.75	0.0062
50	49.71	0.0058

As clear from the breakdown above, a reasonable concordance can be seen between the theoretical strain, namely $\varepsilon_{pe} = 0.007$, obtained from the mathematical model and those achieved in practice.

To carry the developed model over more complicated shapes, the structure illustrated in Figure 5.2 was proposed as two potential choices. For each artifact, an array of dimensional measurements have been designed as shown in the mentioned figure. Note that the measurement configurations shown are the same for specimens with the bridge lines.

One major concern, at this point, is the proper application of the strain rate on the central hole. Since the mathematical model explores linear shrinkage, common sense suggests that the resulting strain rate should be exercised on the perimeter of the internal structure. This has already been approved in the reference study [2] as well.

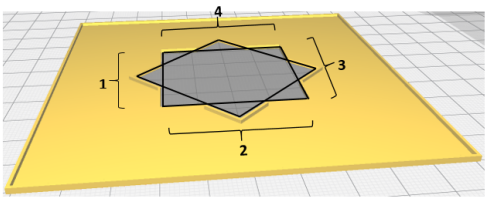

(a) First square (measurement directions 1 to 4)

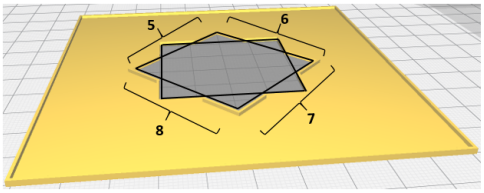

(b) Second square (measurement directions 5 to 8)

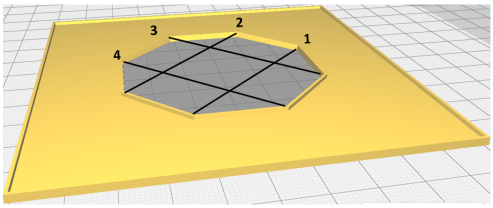

(c) Measurement directions 1 to 4

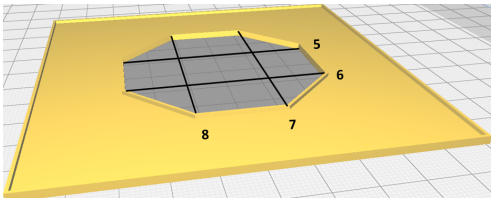

(d) Measurement directions 5 to 8

Figure 5.2: Measurement configuration (black lines) of the asteroid (a and b) and octagon (c and d) test cases.

5.4 First Test: Measurement of Strain for Central Hole Dimensions

Once the shrinkage is implemented on the internal curve perimeter, the shrunk perimeter is obtained. Like discussed in Chapter 4, in the software definition developed, the resulting shrunk curve can be reproduced by offsetting the original curve inwards and calculating the offset distance using the evolutionary solver, Galapagos. This offset curve represents the ultimate internal geometry that is supposed to be achieved in practice after shrinkage occurs.

As the first of the two test cases, the length of the overlapping square sides of the asteroid (See Figure 5.1a.) is measured to be contrasted with that obtained from the mathematical model. Table 5.3 shows corresponding figures for a number of asteroid specimens printed.

Table 5.3: Strain rates for square sides of the asteroid hole

pre-shrinkage	post-shrinkage side length $[mm]$								average
side length $[mm]$	side 1	side 2	side 3	side 4	side 5	side 6	side 7	side 8	strain
30	29.91	29.83	29.82	29.84	29.84	29.79	29.77	29.79	0.00558
35	34.77	34.80	34.76	34.82	34.79	34.79	34.77	34.76	0.00621
40	39.80	39.78	39.66	39.88	39.79	39.73	39.86	39.80	0.00531
45	44.76	44.77	44.74	44.86	44.79	44.86	44.63	44.83	0.00486
50	49.60	49.88	49.70	49.81	49.86	49.63	49.68	49.64	0.0055
55	54.60	54.85	54.70	54.74	54.80	54.69	54.63	54.68	0.00525

In a similar way, the corresponding figures for the second structure (Figure 5.1b) with an octagonal central hole are presented in Table 5.4.

Table 5.4: Strain rates for regular octagon cord

pre-shrinkage	post-shrinkage cord length $[mm]$								average
cord length $[mm]$	cord 1	cord 2	cord 3	cord 4	cord 5	cord 6	cord 7	cord 8	strain
30	29.70	29.57	29.95	29.80	29.57	29.66	29.75	29.87	0.0089
35	34.74	34.59	34.51	34.32	34.46	34.52	34.60	34.57	0.0132
40	39.83	39.78	39.61	39.54	39.83	39.59	39.80	39.68	0.0073
45	44.50	44.41	44.19	44.28	44.56	44.64	44.24	44.86	0.00514
50	49.43	49.45	49.58	49.64	49.42	49.60	49.47	49.46	0.0099
55	54.83	54.95	54.30	54.40	54.40	54.34	54.46	54.64	0.0084

As clear from Tables 5.3 and 5.4, the strain rate for square side lengths is in acceptable coincidence with those found for the straight line segments (See Table 5.2). This conformity is already reported in [2], for circles and rectangles.

5.5 Second Test: Proactive Test Cases; Theoretical vs. Experimental Results

As another way of proving the validity of the mathematical model, models similar to those depicted in Figures 5.1a and 5.1b, but with proactive internal hole sizes were designed (Refer to Section 4.4.16 for more details). Accordingly, the central hole was designed larger than the desired hole, in a way that after shrinkage, it takes the

predicted dimension. Tables 5.5 and 5.6 show results of measurements for artefacts with asteroid and octagonal holes.

Table 5.5: Predicted and actual side lengths of the asteroid model

predicted side	post-shrinkage side length $[mm]$								average actual
length $[mm]$	side 1	side 2	side 3	side 4	side 5	side 6	side 7	side 8	side length$[mm]$
30	30.08	29.99	30.07	30.02	29.98	30.04	30.04	30.08	30.037
35	35.07	34.94	35.10	35.04	35.02	35.01	35.02	34.97	35.016
40	40.07	40.04	39.98	39.89	40.04	40.05	40.00	40.05	40.015
45	44.96	45.00	44.85	45.08	44.92	44.94	45.09	45.03	44.984
50	49.90	50.02	49.86	50.05	50.01	49.85	50.12	49.90	49.962
55	55.00	54.98	55.07	54.93	54.90	54.90	54.84	55.12	54.967

Table 5.6: Predicted and actual cord lengths of the octagon model

predicted cord	post-shrinkage cord length $[mm]$								average actual
length $[mm]$	cord 1	cord 2	cord 3	cord 4	cord 5	cord 6	cord 7	cord 8	cord length $[mm]$
30	29.76	29.66	30.03	29.87	30.00	30.08	29.88	29.08	29.891
35	34.86	35.04	34.96	35.04	34.99	35.18	35.26	34.70	35.004
40	39.93	39.99	39.87	39.90	39.90	39.93	39.94	39.93	39.924
45	45.00	45.03	45.08	45.03	45.08	45.09	44.78	45.05	45.017
50	50.03	49.98	49.99	50.07	50.05	50.02	50.07	50.05	50.032
55	55.02	55.02	54.92	54.98	54.96	55.04	54.92	55.00	54.985

Test results for the proactive prints have been put to proof against theory in Figures 5.3 and 5.4. These figures show the deviation of each specimen after shrinkage process has fully occurred. The error bars indicate the standard deviation of eight cord lengths (n=8). Therefore, those tolerances that cover the zero deviation on the vertical axis can be taken as accurate predictions. As such, all the specimens except for octagons with theoretical cord lengths of 30 and $40[mm]$ are anticipated accurately enough.

The next step, involves investigating the effect of bridge lines' shrinkage on the internal hole shrinkage, alternatively known as shrinkage compensation approach.

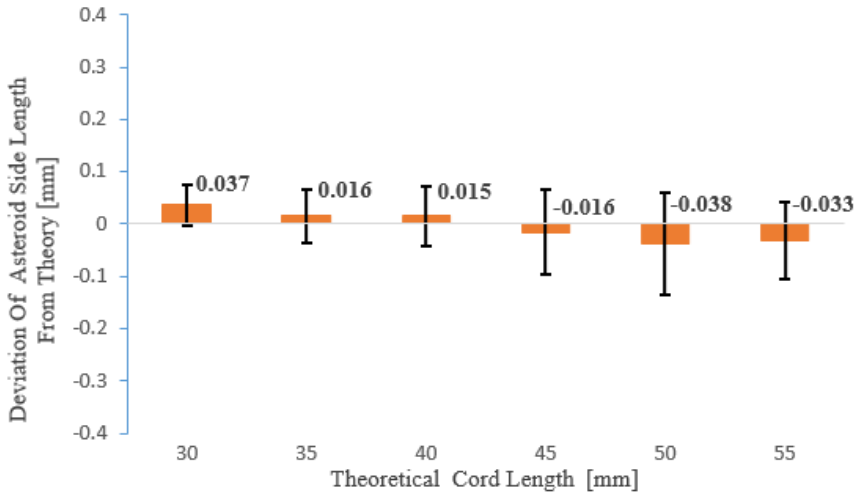

Figure 5.3: Deviation of experimental results from theory in specimens with asteroid holes. The error data are preesnted as mean ± SEM (n=8).

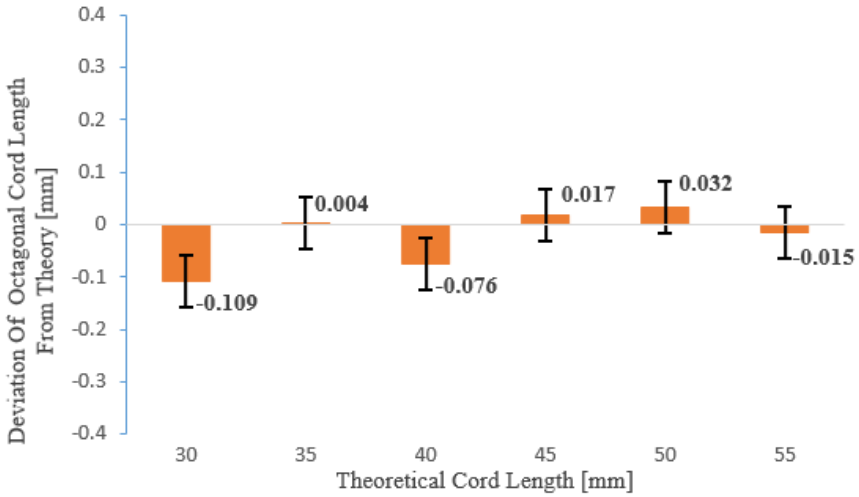

Figure 5.4: Deviation of experimental results from theory in specimens with octagonal holes. The error data are preesnted as mean ± SEM (n=8).

5.6 Third Test: Shrinkage Compensation Effect

According to the data provided in Reference [2], a straight line shrinks towards its center, hence, in a geometrical structure like that shown in Figure 5.5, the internal hole shrinkage is supposed to decrease as a result of the bridge lines shrinkage.

It appears necessary to recall that the longer the bridge lines are, the more compen-

sation is expected. For a complete compensation effect wherein the lines length is so that the central hole undergoes no shrinkage, the full compensation length for bridge lines needs to be calculated.

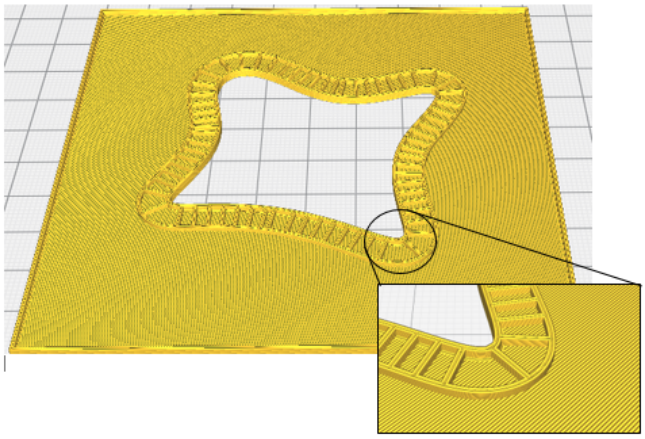

Figure 5.5: Shrinkage compensation structure for a sample specimen

5.6.1 Derivation of Bridge Line Length for a Full Compensation

In order to have a full compensation (i.e. no shrinkage of the central hole), the desired length of the bridge lines, and hence, the wide offset distance, needs to be calculated. The process through which the full compensation length of lines are calculated is depicted in Figure 5.6.

To cast light on the process introduced in the mentioned figure, a numerical example of how the shrinkage compensation approach works is offered below.

The strain for the original model was obtained from the mathematical model to be $\varepsilon = 0.00703$.

According to the Galapagos solution for the asteroid hole, the strain rate of 0.007 yields a shrunk central curve that would stand at a distance of $0.219[mm]$ from the original curve. The distance difference of 0.219 millimeters (f) needs to be balanced out by the bridging line shrinkage (The following calculations are done in the two lowest components shown in Figure 5.6b). Put another way:

$$f = \frac{\Delta l}{2} = \frac{\varepsilon l_{fc}}{2} \tag{5.5}$$

Therefore:

$$l_{fc} = \frac{2f}{\varepsilon} \tag{5.6}$$

where l_{fc}, Δl and f, respectively represent the length of bridge lines for full compensation, their shrinkage rate and the offset distance (i.e. the shrunk curve's distance from the original hole curve). The factor 2 is in place to account for the fact that a bridge line shrinks towards its center, and therefore, on its end connected to the central curve only half its total shrinkage is operating on the curve. By way of example for

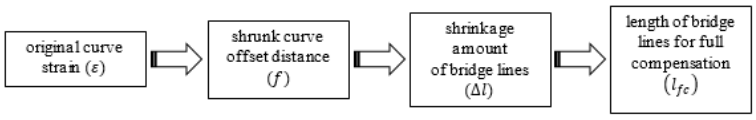

(a) Flow chart of bridge lines length determination for full compensation

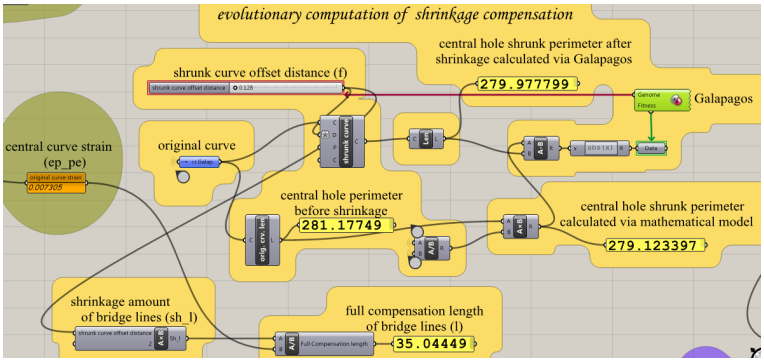

(b) Visual map of bridge lines length determination for full compensation

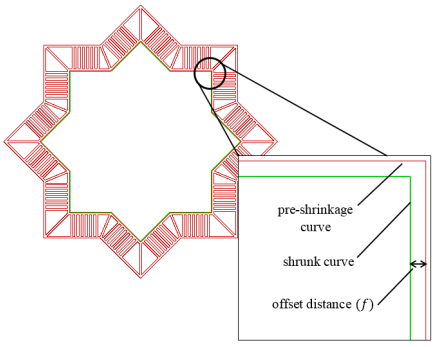

(c) Internal hole before and after shrinkage

Figure 5.6: Process of auxiliary line length calculation for full compensation

parts with 60 millimeter of square side length, based on the Galapagos results for f,

and on Equation 5.6:

$$l_{fc} = \frac{2(0.219)}{0.00730} \approx 60[mm] \tag{5.7}$$

This implies that to fully compensate for the shrinkage of the internal hole with squares sides of 60 millimeter, bridge lines of 60 millimeter are required.

It deserves attention that although a full compensation length is computable, geometrical restrictions can sometimes set a limit on the maximum length of bridge lines that can be obtained. This happens to be the case with the central asteroid geometry. The restriction can arise from the fact that longer stretching lines implies higher risk of these lines colliding with special lines around corners, and thus resulting in omission of more regular lines. This effect is illustrated in Figure 5.7. As appears from the mentioned figure, geometries with longer bridge lines tend to have fewer of such lines. On the contrary, a regular polygon seems not to suffer from this restriction. The central issue is that low density of bridge lines can cause compensation paradigm to not show its effect to a full extent. Therefore, the asteroid test case was replaced with a regular decagon.

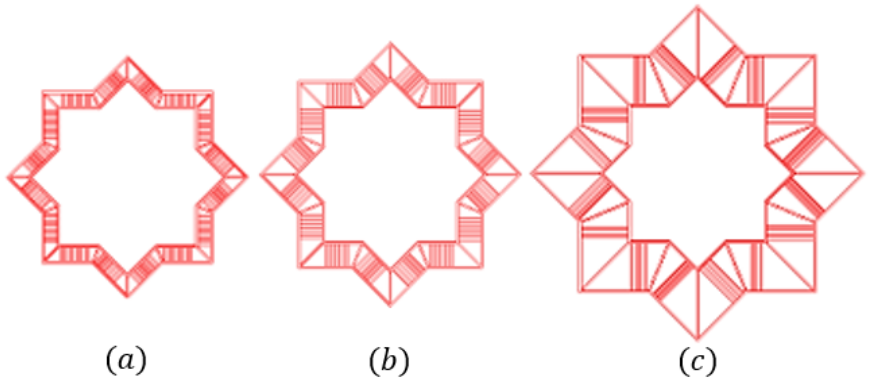

Figure 5.7: Due to specific geometry of the hole, the longer auxiliary lines grow, the fewer they count (auxiliary lines with 5 (a), 10 (b) and 15 (c) $[mm]$ lengths)

5.6.2 Effect of Bridge Lines Length on Shrinkage of the Central Hole (Partial Compensation Effect)

As stated in Section 5.6.1, investigating the full compensation scenario seems to be elusive for our first case. However, to set a basis to explore the effect of length

of bridge lines on the shrinkage rate of the inner curve, a series of specimens with theoretical square side of 60$[mm]$ were printed. This set of prints includes central structures surrounded with lines of different lengths as depicted in Figure 5.8. Figures 5.8a to 5.8h represent CAD and real octagonal artefacts, while Figures 5.8i to 5.8p show CAD and real decagonal specimens.

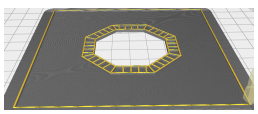

(a) CAD model of 5$[mm]$ octagonal hole

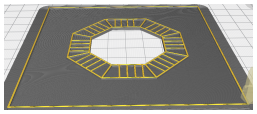

(b) CAD model of 10$[mm]$ octagonal hole

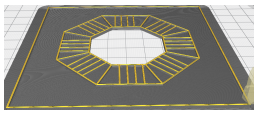

(c) CAD model of 15$[mm]$ octagonal hole

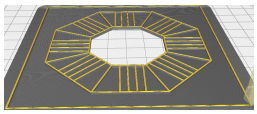

(d) CAD model of 20$[mm]$ octagonal hole

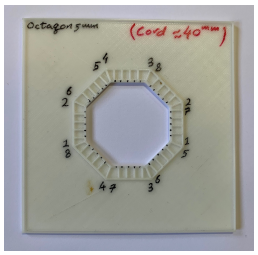

(e) Real octagon specimen (5$[m]$)

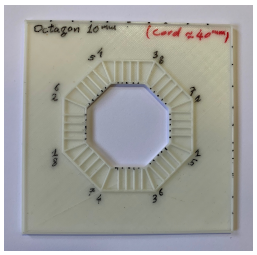

(f) Real octagon specimen (10$[m]$)

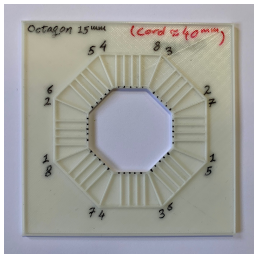

(g) Real octagon specimen (15$[m]$)

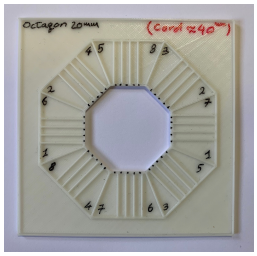

(h) Real octagon specimen (20$[m]$)

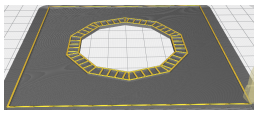

(i) CAD model of 5$[mm]$ decagonal hole

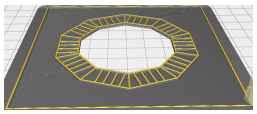

(j) CAD model of 10$[mm]$ decagonal hole

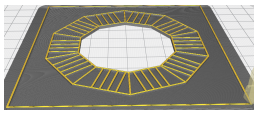

(k) CAD model of 15$[mm]$ decagonal hole

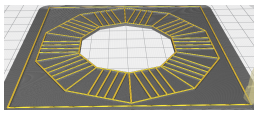

(l) CAD model of 20$[mm]$ decagonal hole

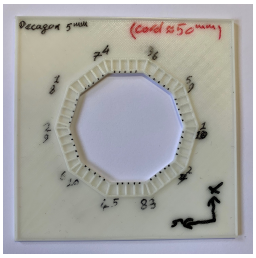

(m) Real decagon specimen (5$[m]$)

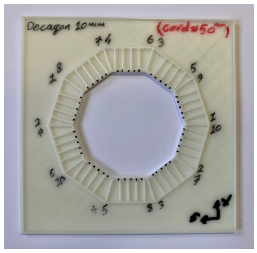

(n) Real decagon specimen (10$[m]$)

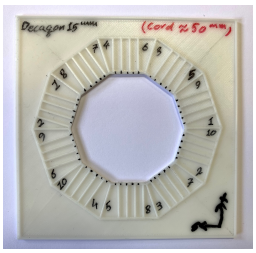

(o) Real decagon specimen (15$[m]$)

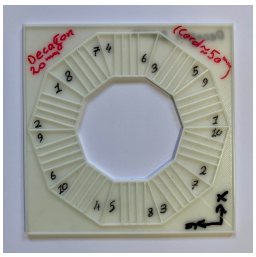

(p) Real decagon specimen (20$[m]$)

Figure 5.8: CAD and corresponding real test cases with octagon and decagon central hole having bridge lines of 5, 10, 15 and 20 $[mm]$ lengths

The measurement configuration for the octagon is the same as that shown in Figure 5.2. In a similar way, that of the decagon is shown in Figure 5.9. It is noteworthy that there will be ten measurement directions for the decagon.

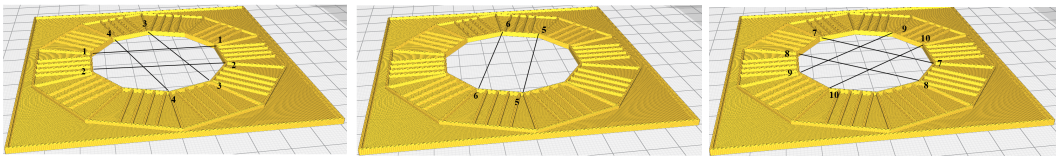

(a) Measurement directions 1 to 4 (b) Measurement directions 5 and 6 (c) Measurement directions 7 to 10

Figure 5.9: Measurement configuration for the decagon test case

It is expected for longer lines to have more compensating effect. The interplay between the shrinkage of the central hole and that of the lines for a full compensation was shown in Equation 5.5. Accordingly, for a partial compensation:

$$\Delta C = 2f - \Delta l \tag{5.8}$$

where ΔC represents the final offset distance that the hole stands at as a result of the line's compensation effect. It seems noteworthy at this point that the partial compensation distance, ΔC, is calculated for the entire cord distance, and not for half of it, which explains the existence of the factor 2 on the right hand side of the equation.

Based on Equation 5.8, the size of a hole with a cord length of $l_0[mm]$ is expected to decline to $l_0 - \Delta C$. Thus,

$$l_c = l_0 - 2f + \Delta l \tag{5.9}$$

where l_c denotes the compensated distance.

By way of example, for an octagon hole of $40[mm]$ cord length surrounded with $5[mm]$ long bridge lines, values for f and Δl are found from the Galapagos calculations and the mathematical model (See Figure 5.6) as follows:

$$f_{octagon} = 0.146[mm]$$

$$\Delta l_{|_{l_0=5[mm]}} = 5\varepsilon = 5(0.007305) = 0.036525[mm]$$

As per Equation 5.9, compensated distance for such a central hole can be obtained as

$$l_c = 40 - 2(0.146) + 0.036525 = 39.744[mm]$$

In the same way, for the decagonal hole, Galapagos results suggest that

$$f_{decagon} = 0.183[mm]$$

Therefore, the compensated distance for the two test cases can be predicted via Equation 5.9. Results of such partial compensations are calculated accordingly and displayed in Table 5.7.

Table 5.7: Expected compensation effect on octagonal and decagonal central holes with respectively $40[mm]$ and $50[mm]$ of cord lengths.

bridge line length $[mm]$	expected octagon cord length$[mm]$	expected decagon cord length$[mm]$
5	39.744	49.671
10	39.781	49.708
15	39.818	49.744
20	39.854	49.781

5.6.3 Theoretical vs. Experimental Results for Shrinkage Compensation Test Cases

As mentioned earlier, two types of artifacts are put to test to see the partial compensation effect. Breakdowns for measurements of the octagonal hole with bridge lines are presented in Table 5.8.

Table 5.8: Shrinkage of octagon with square sides of $40[mm]$; (See Figures 5.8a to 5.8d)

length of	post-shrinkage cord length $[mm]$								average side
lines $[mm]$	cord 1	cord 2	cord 3	cord 4	cord 5	cord 6	cord 7	cord 8	length $[mm]$
5	39.69	39.71	39.94	39.87	39.85	39.69	39.60	39.60	39.743
10	39.70	39.71	39.88	39.79	39.78	39.77	39.73	39.75	39.764
15	39.72	39.73	39.93	39.89	39.83	39.77	39.68	39.70	39.781
20	39.77	39.72	39.95	39.85	39.83	39.78	39.73	39.77	39.802

Likewise, result data for the measurement of the octagonal hole is offered in Table

5.8.

Table 5.9: Shrinkage of decagon with cord length of 50$[mm]$; (See Figures 5.8i to 5.8l)

length of lines $[mm]$	post-shrinkage cord length $[mm]$										average cord length $[mm]$
	cord 1	cord 2	cord 3	cord 4	cord 5	cord 6	cord 7	cord 8	cord 9	cord 10	
5	49.63	49.71	49.90	49.84	49.71	49.72	49.86	49.82	49.61	49.52	49.732
10	49.75	49.74	49.93	49.90	49.75	49.72	49.77	49.84	49.55	49.54	49.749
15	49.72	49.80	49.84	49.77	49.65	49.56	49.80	49.82	49.55	49.51	49.758
20	49.79	49.76	49.83	49.88	49.81	49.63	49.86	49.89	49.61	49.59	49.765

A comparison between theoretical cord lengths (from Table 5.7) and the average experimental results (from Tables 5.8 and 5.9) is pertinent here. Figures 5.10 and 5.11 put in contrast these two sets of outcomes. In Figure 5.10, the error bars represent the standard deviation of eight cord lengths presented in Table 5.8, used to define each specimens' cord length tolerances. The number $(n = 8)$ in the caption indicates this. The same can be stated for the decagonal hole with ten cord lengths presented in Table 5.9, hence the term $(n = 10)$. This is shown in Figure 5.11.

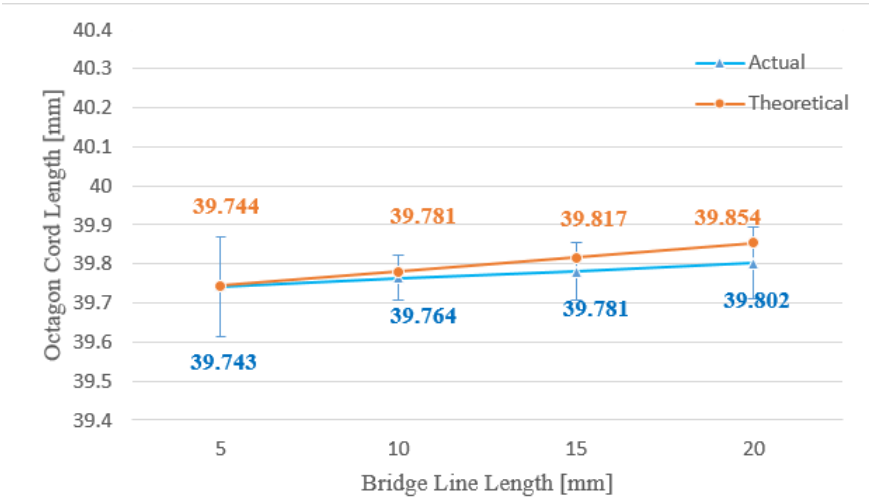

Figure 5.10: Comparison between theoretical and actual results of compensation effect in the octagonal specimen. The error data are presented as mean $\pm$ SEM (n=8).

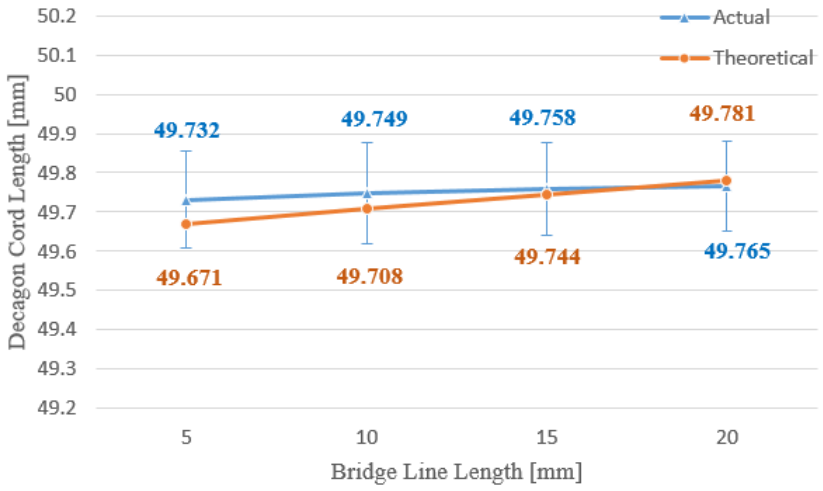

Figure 5.11: Comparison between theoretical and actual results of compensation effect in the decagonal specimen. The error data are presented as mean $\pm$ SEM (n=10).

As is obvious from Figures 5.10 and 5.11, similar compensation trends between the two sets of data suggest the validity of the theoretical work presented so far. Additionally, it is notable from the mentioned figures that the longer bridge lines grow, the more compensation effect is found to be at work. In general, these conformities bear evidence to the fact that shrinkage compensation method is reliably applicable to 2.5D artifacts with central holes.

5.7 Comparison between Caliper and CMM Measurements

To draw a comparison between caliper and CMM measurements, all specimens with bridge lines were measured using CMM, except the one with decagonal hole with $15[mm]$ bridge lines (Figure 5.18), for which CMM measurements could not be accomplished due to practical restrictions.

Comparison results for octagonal holes are shown in Figures 5.12 to 5.15, and for decagonal openings in Figures 5.16 to 5.19.

Each cord whether in a decagonal or an octagonal hole, has been measured three times, and the error bars shown on figures represent the standard deviations of those

three repetitions.

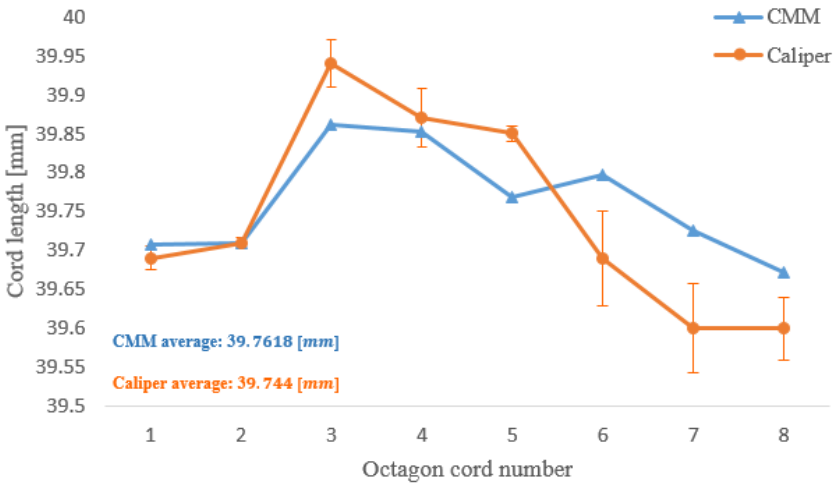

Figure 5.12: CMM vs. caliper measurement results for 40$[mm]$ octagonal hole with bridge lines of 5$[mm]$ length. The error data are presented as mean $\pm$ SEM (n=3).

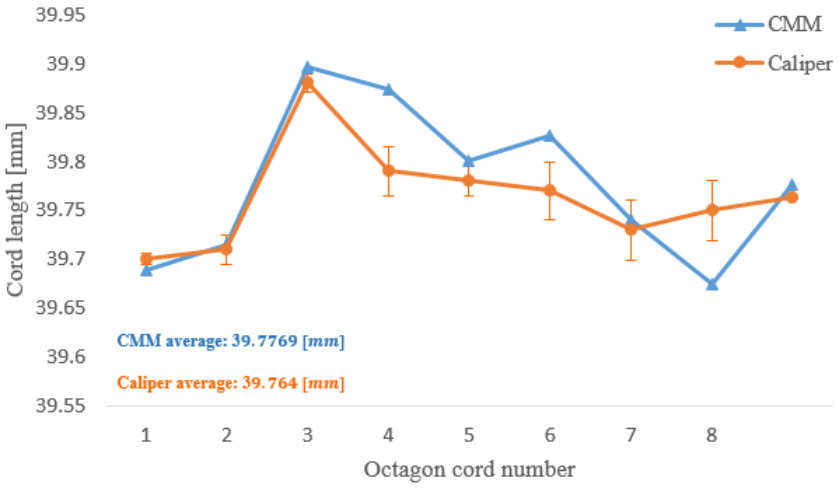

Figure 5.13: CMM vs. caliper measurement results for 40$[mm]$ octagonal hole with bridge lines of 10$[mm]$ length. The error data are presented as mean $\pm$ SEM (n=3).

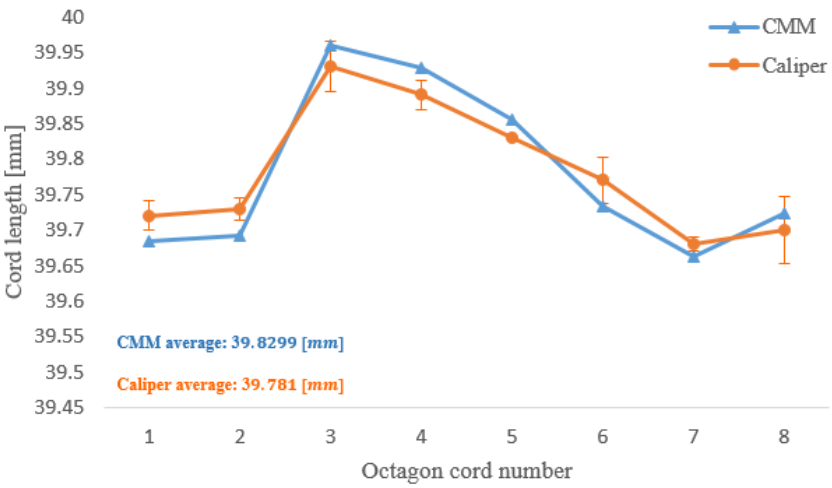

Figure 5.14: CMM vs. caliper measurement results for 40$[mm]$ octagonal hole with bridge lines of 15$[mm]$ length. The error data are presented as mean $\pm$ SEM (n=3).

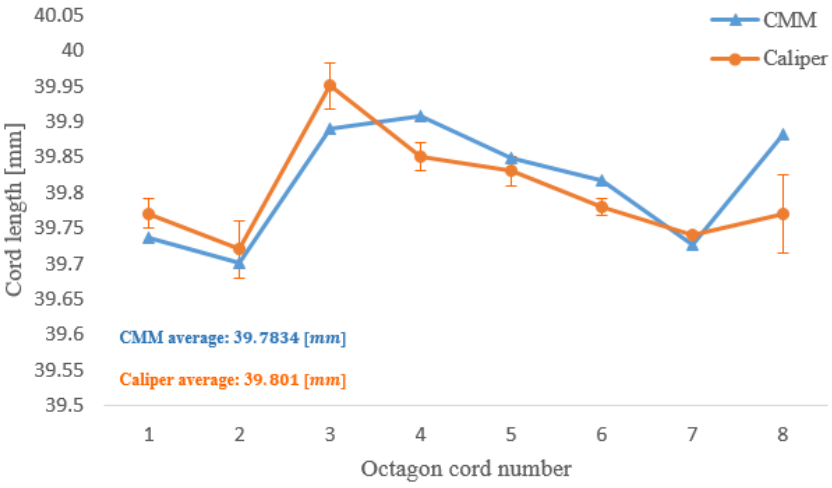

Figure 5.15: CMM measurement results for 40$[mm]$ octagonal hole with bridge lines of 20$[mm]$ length. The error data are presented as mean $\pm$ SEM (n=3).

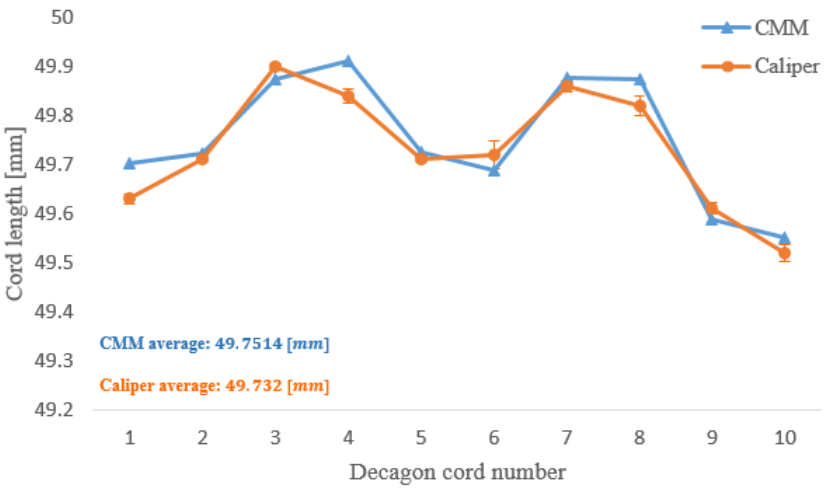

Figure 5.16: CMM measurement results for $50[mm]$ decagonal hole with bridge lines of $5[mm]$ length. The error data are presented as mean $\pm$ SEM (n=3).

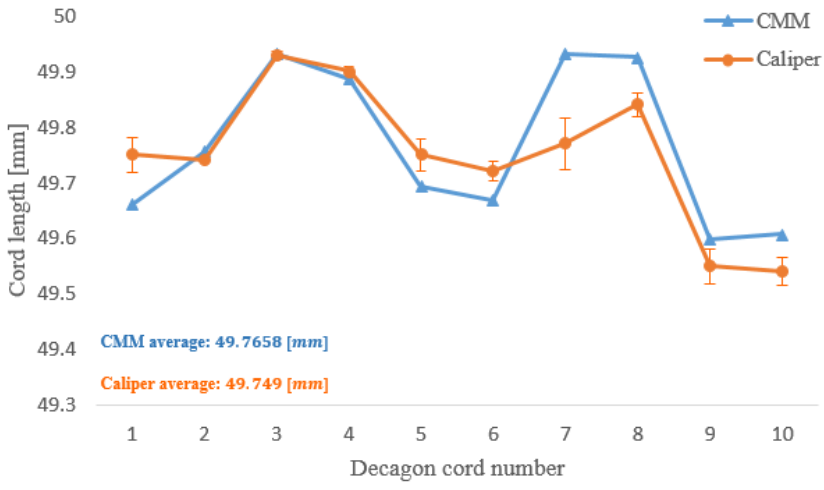

Figure 5.17: CMM measurement results for $50[mm]$ decagonal hole with bridge lines of $10[mm]$ length. The error data are presented as mean $\pm$ SEM (n=3).

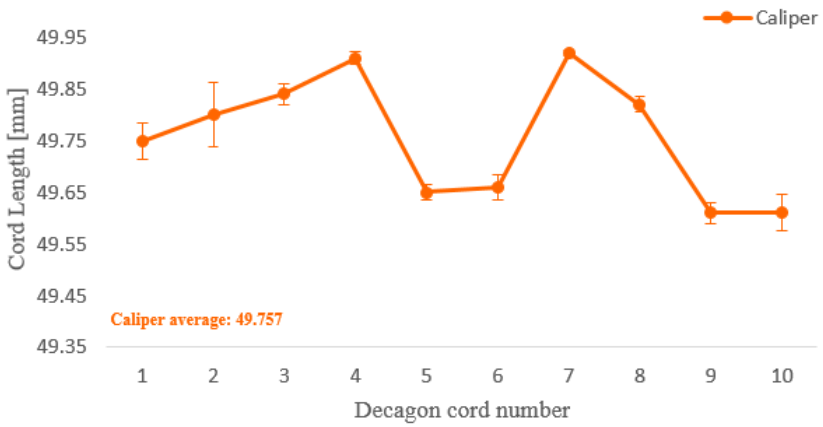

Figure 5.18: CMM measurement results for $50[mm]$ decagonal hole with bridge lines of $15[mm]$ length. The error data are presented as mean $\pm$ SEM (n=3).

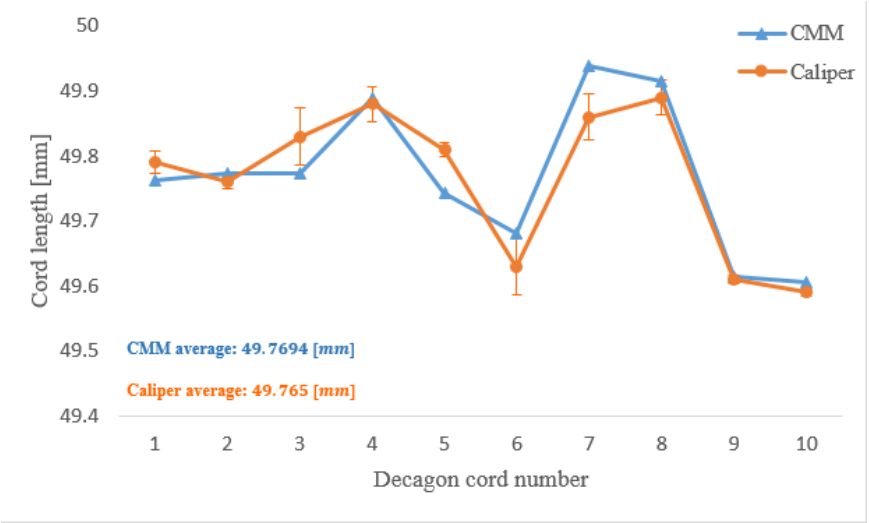

Figure 5.19: CMM vs. caliper measurement results for $50[mm]$ decagonal hole with bridge lines of $20[mm]$ length. The error data are presented as mean $\pm$ SEM (n=3).

5.8 Effect of Changes in Shrinkage Compensation Geometry

The purpose of this section is to explore any possible effects of geometrical changes in the shrinkage compensation structure on the central hole shrinkage. To this end,

three types of test cases are designed. In the first type, the base beneath the bridge lines is removed (Figure 5.20).

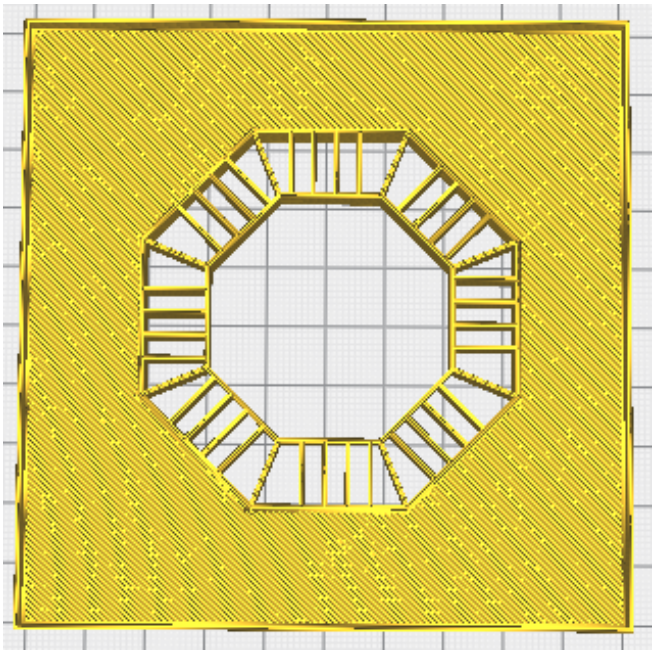

Figure 5.20: Test case with baseless bridge lines (top view)

In the second type, the distance between the wider offset wall and the peripheral wall is filled up (Figure 5.21). As for the third case, the original SC structure is maintained with the difference that the wider offset wall is removed (Figure 5.22).

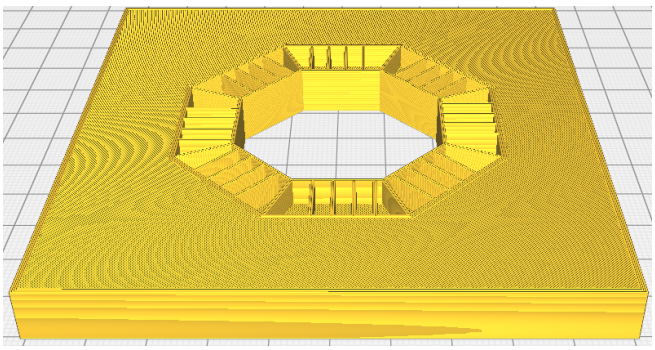

Figure 5.21: Test case with full-height base

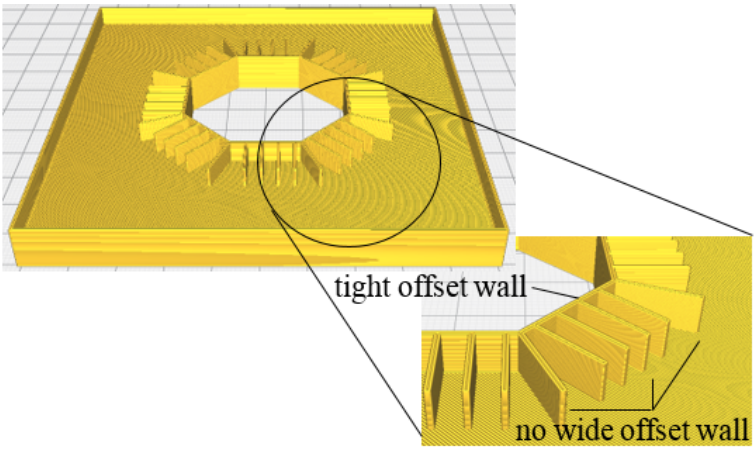

Figure 5.22: Test case without wide offset wall

Each of these types is printed with the overall height of $3[mm]$, like the original test cases, as well as with $10[mm]$. Since no $10[mm]$ specimen with *initial* geometry has been fabricated up to this point, one such a model is added to the recent set of models as well. All these seven new specimens have octagonal central hole of $40[mm]$ cord length. Their bridge line length is set to $10[mm]$ in all the seven specimens.

Tables 5.10 and 5.11 compare the relating information about these recent seven specimens. (Information for the initial model in Table 5.10 is provided from Table 5.8.)

Table 5.10: Shrinkage of octagon with cords of $40[mm]$, bridge lines of $10[mm]$ and overall height of $3[mm]$ with various geometrical features

model	post-shrinkage cord length $[mm]$								average cord
feature	cord 1	cord 2	cord 3	cord 4	cord 5	cord 6	cord 7	cord 8	length $[mm]$
initial model	39.70	39.71	39.88	39.79	39.78	39.77	39.73	39.75	39.764
baseless bridge lines	39.80	39.85	39.85	39.84	39.84	39.85	39.66	39.69	39.797
full-height base	39.78	39.78	39.89	39.89	39.72	39.82	39.80	39.83	39.814
without outer wall	39.81	39.90	39.81	39.82	39.88	39.81	39.79	39.83	39.831

Table 5.11: Shrinkage of octagon with cords of $40[mm]$, bridge lines of $10[mm]$ and $10[mm]$ of overall height with various geometrical features

model	post-shrinkage cord length $[mm]$								average cord
feature	cord 1	cord 2	cord 3	cord 4	cord 5	cord 6	cord 7	cord 8	length $[mm]$
initial model	39.85	39.84	39.90	39.91	39.92	39.92	39.88	39.90	39.890
baseless bridge lines	39.92	39.92	39.79	39.87	39.89	39.88	39.91	39.88	39.883
full-height base	39.79	39.85	39.83	39.87	39.82	39.83	39.82	39.83	39.83
without outer wall	39.85	39.85	39.82	39.85	39.85	39.83	39.83	39.83	39.875

In Table 5.10, a relative increase in compensation effect can be seen in the baseless artifact in comparison with the initial version. This can be attributed to the deterrent effect that the base can have on the shrinkage of bridge lines.

In the same table, the specimen with full-height base appears to be more shrinkage compensated. This is possibly because the displacement of the bridge lines occurs more on that end of these lines that is connected to the inner wall than on the end connected to the full-height base.

Despite similarities, some discrepancies can be seen between the two tables' trends as well. For example it appears that removing the bottom base of the bridge lines is minimal impact on the shrinkage of the hole in higher models, unlike the lower specimens. This difference can be rationalized based on the presumption that the influence of base is mitigated in higher layers of the model.

Comparing similar geometries from Tables 5.10 and 5.11 suggests that the central hole of higher models undergoes less shrinkage. This can be explained due to the fact that in higher specimens, greater height of bridge lines allows for more compensation effect in higher layers of these lines. Nevertheless, in lower-height specimens, the compensation effect of bridge lines is partly restricted by the base.

In both of the tables in question, no clear consistency is witnessed on specimens without outer wall.

Plots related to all the parts discussed in this section are shown in Figures 5.23 and 5.24.

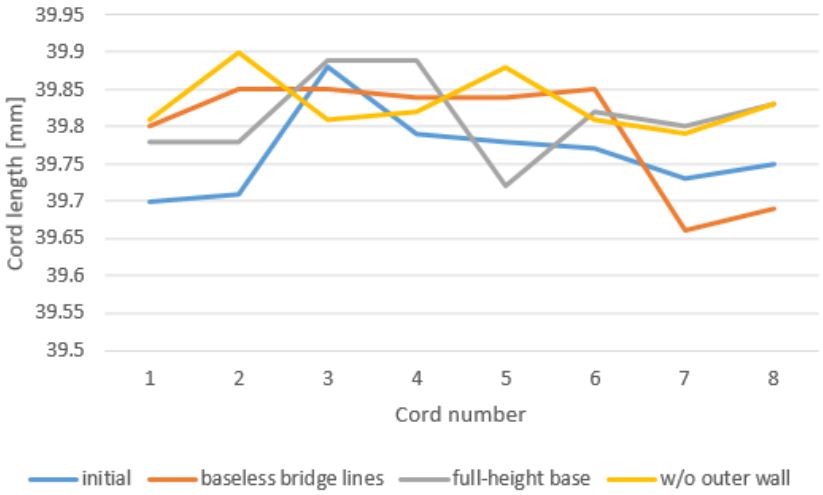

Figure 5.23: Shrinkage of octagon with cords of 40$[mm]$, bridge lines of 10$[mm]$ and 3$[mm]$ of overall height with various geometrical features

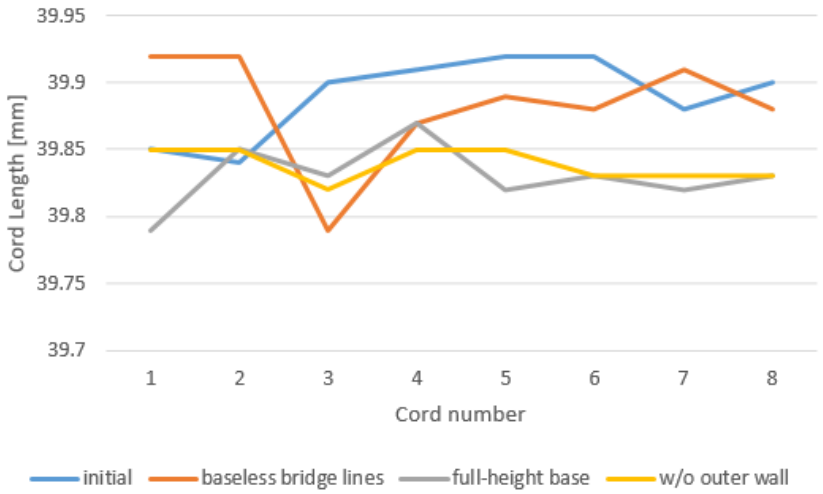

Figure 5.24: Shrinkage of octagon with cords of 40$[mm]$, bridge lines of 10$[mm]$ and 10$[mm]$ of overall height with various geometrical features

5.9 Closure

Analyses presented so far showcase a good coincidence between theoretical models (Chapter 4) and the experiment results (present chapter). Despite the initial affirmative results obtained, further expansions can be made on the design of specimens, especially on their internal hole geometry. Whether or not the compensation approach presented

in this thesis can be extended to three dimensional bodies seems a question deserving further investigation.

CHAPTER 6

CONCLUSIONS AND FURTHER INVESTIGATIONS

6.1 Closing Remarks

As it has been discussed already, this dissertation proposes, in the first place, an automated algorithm (Refer to Chapter 4) that generates 2.5D artifacts, geometrically compliant with the shrinkage compensation configuration. A mathematical model is also integrated into the algorithm. This model operates on the Zener model of viscoelasticity discussed in Section 3.4.2. In essence, the use of the mathematical model is to predict the overall strain of a straight strip of filament. The numerical value obtained for the a strip, however, can be safely carried over to more complicated geometries to predict the change in their central hole dimensions. With regard to this, three main series of tests are designed and conducted.

The first series attempts to verify the modelling results for central holes with asteroid and octagonal shapes. This is done in the absence of auxiliary lines. Test results support the mathematical model.

Very much similar to the first set, the second set of tests, uses the obtained strain rate to generate larger central holes (still without bridge lines) that after shrinkage would diminish to the desirable dimensions. These experiments are given the name *proactive/anticipatory tests*.

In the final array of tests, the shrinkage compensation method is brought into play. As such, octagonal and decagonal central holes encompassed by bridge lines are put to test. The mathematical model, along with the evolutionary solver, are used to predict the ultimate state of the central hole after completely cooling down to room

temperature. Different lengths for bridge lines are designed and looked into for their impact in these experiments. Test results well support the theoretical modellings, as discussed in Chapter 5.

6.2 Limitations of the Study

There are restrictions involved in this work, that need to be addressed in similar future works. Some of these restrictions are cited below:

a) An accurate value for the coefficient of thermal expansion (CTE) is not announced by the manufacturers of the filament used, and as a result, experiment results from various papers were taken into account.

b) Not all geometries for the central hole lend themselves to the proper application of the shrinkage compensation method.

c) Since print precision is the theme of this research work, high quality prints are essentially required. However, printed models are not processed for their surface accuracy once being produced.

d) In presence of surface coarseness, CMM measurements are prone to evaluate lengths smaller than the actual size. Hence, measurements give higher shrinkage rates.

6.3 Possible Next Steps

The work conducted in this dissertation proves that the shrinkage compensation approach is a promising workaround to the problem of FFF accuracy. However, there arise a number of problems from this research work, that can be further elaborated on in the future.

The algorithm developed in this dissertation operates on 2.5D geometries as seen before. However, it can be considered as a good starting point for expanding the work further on a similar three-dimensional work as well. A 3D version of specimens will

require approximation and optimization of curves along different layers of the third dimension to evolve a final shape with minimum shrinkage.

Another area worthy of further attention is that although the bridge lines' length effect on the accuracy of internal hole was introduced as a helpful approach, the influence of these lines' width on the central structure's shrinkage remained unspoken. This issue can take up added importance when the necessity of using wider bridge lines arises. Such necessity can come up in situations where a full compensation, hence longer bridge lines, are required. However, as we saw in Section 5.6, not always such a solution is viable. To overcome such a shortcoming, widening the auxiliary lines might count as a possible solution. Finding a model that would explain the impact of these lines' width on the strain is another question to explore.

Another unstated issue concerns geometrical traits of the central hole. Potential impacts of such traits as concavity and convexity of the central shape, curvedness or straightness of its sides and acuteness of the angles seem to remain as noteworthy questions. In other words, can more accurate results be achieved if the overall strain rate, ε, is applied to the hole perimeter with regard to such geometrical characteristics?

REFERENCES

[1] B. N. Turner and S. A. Gold, A review of melt extrusion additive manufacturing processes: II. Materials, dimensional accuracy, and surface roughness, Rapid Prototyp. J., vol. 21, no. 3, pp. 250261, 2015.

[2] https://www.additivemanufacturing.media/cdn/cms/7_families_print_version.pdf

[3] Cotteleer, Mark, Jonathan Holdowsky, and Monica Mahto. "The 3D opportunity primer: The basics of additive manufacturing.", 2013.

[4] https://www.3dnatives.com/en/3d-printing-vs-cnc-160320184/

[5] https://www.myminifactory.com/object/3d-print-all-in-one-3d-printer-test-65332

[6] M. Mahesh, Y. S. Wong, J. Y. H. Fuh, and H. T. Loh, Benchmarking for comparative evaluation of RP systems and processes, Rapid Prototyp. J., vol. 10, no. 2, pp. 123135, 2004.

[7] L. Rebaioli and I. Fassi, A review on benchmark artifacts for evaluating the geometrical performance of additive manufacturing processes, Int. J. Adv. Manuf. Technol., vol. 93, no. 58, pp. 25712598, 2017.

[8] Anhua, P. and Xingming, X., Investigation on reasons inducing error and measures improving accuracy in fused deposition modeling, Advances in Information Sciences and Service Sciences, Vol. 4 No. 1, pp. 149-157, 2012.

[9] S. L. Campanelli, G. Cardano, R. Giannoccaro, A. D. Ludovico, and E. L. J. Bohez, Statistical analysis of the stereolithographic process to improve the accuracy, CAD Comput. Aided Des., vol. 39, no. 1, pp. 8086, 2007.

[10] H. Bikas, P. Stavropoulos, and G. Chryssolouris, Additive manufacturing methods and modeling approaches: A critical review, Int. J. Adv. Manuf. Technol., vol. 83, no. 14, pp. 389405, 2016.

[11] G. Chryssolouris, J. Kotselis, P. Koutzampoikidis, S. Zannis, and D. Mourtzis, Dimensional accuracy modelling of stereolithography parts, Manuf. Syst., vol. 30, no. 2, pp. 170174, 2000.

[12] E. R. Khorasani and H. Baseri, Determination of optimum SLA process parameters of H-shaped parts, J. Mech. Sci. Technol., vol. 27, no. 3, pp. 857863, 2013.

[13] PerkinElmer Inc., Dynamic Mechanical Analysis (DMA) - A Beginners Guide, PerkinElmer, pp. 123, 2008.

[14] M. Vispute, N. Kumar, P. K. Jain, P. Tandon, and P. M. Pandey, Shrinkage compensation study for performing machining on additive manufactured parts, Mater. Today Proc., vol. 5, no. 9, pp. 1854418551, 2018.

[15] Y. M. Huang and H. Y. Lan, CAD/CAE/CAM integration for increasing the accuracy of mask rapid prototyping system, Comput. Ind., vol. 56, no. 5, pp. 442456, 2005.

[16] Y. M. Huang and H. Y. Lan, Dynamic reverse compensation to increase the accuracy of the rapid prototyping system, J. Mater. Process. Technol., vol. 167, no. 23, pp. 167176, 2005.

[17] S. M. Gaytan et al., Fabrication of barium titanate by binder jetting additive manufacturing technology, Ceram. Int., vol. 41, no. 5, pp. 66106619, 2015.

[18] Lee, Pil-Ho, Haseung Chung, Sang Won Lee, Jeongkon Yoo, and Jeonghan Ko. "Dimensional accuracy in additive manufacturing processes." In ASME 2014 International Manufacturing Science and Engineering Conference collocated with the JSME 2014 International Conference on Materials and Processing and the 42nd North American Manufacturing Research Conference, pp. V001T04A045-V001T04A045. American Society of Mechanical Engineers, 2014.

[19] R. M. Taft, S. Kondor, and G. T. Grant, Accuracy of rapid prototype models for head and neck reconstruction, J. Prosthet. Dent., vol. 106, no. 6, pp. 399408, 2011.

[20] D. Dimitrov, W. Van Wijck, K. Schreve, and N. De Beer, Investigating the achievable accuracy of three dimensional printing, Rapid Prototyp. J., vol. 12, no. 1, pp. 4252, 2006.

[21] D. Bourell, Rapid Prototyping Journal: Editorial, Rapid Prototyp. J., vol. 10, no. 1, pp. 56, 2004.

[22] M. Vaezi and C. K. Chua, Effects of layer thickness and binder saturation level parameters on 3D printing process, Int. J. Adv. Manuf. Technol., vol. 53, no. 14, pp. 275284, 2011.

[23] S. Stopp, T. Wolff, F. Irlinger, and T. Lueth, A new method for printer calibration and contour accuracy manufacturing with 3D-print technology, Rapid Prototyp. J., vol. 14, no. 3, pp. 167172, 2008.

[24] . Liu, L. Zhang, J. Mo, and B. Qian, New method of improving parts accuracy by adding heat balance support in selective laser sintering, J. Zhejiang Univ. A, vol. 10, no. 3, pp. 361369, 2009.

[25] Rong-Ji, L. Xin-Hua, W. Qing-Ding, and W. Lingling, Optimizing process parameters for selective laser sintering based on neural network and genetic algorithm, Int. J. Adv. Manuf. Technol., vol. 42, no. 1112, pp. 10351042, 2009.

[26] Chung and S. Das, Processing and properties of glass bead particulate-filled functionally graded Nylon-11 composites produced by selective laser sintering, Mater. Sci. Eng. A, vol. 437, no. 2, pp. 226234, 2006.

[27] S. Hinduja, L. Li, J. Atkinson, R. Heinemann, K.Kontis, P. Mativenga, J. Methven, A. Pinkerton, M. Sheikh, Z. Wang, Proceedings of the 36th International Matador Conference, 2010.

[28] G. Zhou and Z. He, Rapid pattern based powder sintering technique and related shrinkage control, Mater. Des., vol. 19, no. 56, pp. 241248, 2002.

[29] Q. Dao et al., Calculation of Shrinkage Compensation Factors for Rapid Prototyping (FDM 1650), Comput. Appl. Eng. Educ., vol. 7, no. 3, pp. 186195, 1999.

[30] Galantucci, L.M. and Lavecchia, F., Direct digital manufacturing of ABS parts: an experimental study on effectiveness of proprietary software for shrinkage compensation, International Journal of Digital Content Technology and its Applications, Vol. 6 No. 1, pp. 546-555, 2012.

[31] N. S. A. Bakar, M. R. Alkahari, and H. Boejang, Analysis on fused deposition modelling performance, J. Zhejiang Univ. A, vol. 11, no. 12, pp. 972977, 2010.

[32] R. Bansal, Improving dimensional accuracy of fused deposition modelling (FDM) parts using response surface methodology, p. 32, 2011.

[33] T. M. Wang, J. T. Xi, and Y. Jin, A model research for prototype warp deformation in the FDM process, Int. J. Adv. Manuf. Technol., vol. 33, no. 1112, pp. 10871096, 2007.

[34] P. K. Gurrala and S. P. Regalla, DOE Based Parametric Study of Volumetric Change of FDM Parts, Procedia Mater. Sci., vol. 6, no. Icmpc, pp. 354360, 2014.

[35] A. Gregorian, B. Elliott, R. Navarro, F. Ochoa, H. Singh, E. Monge, "ACCURACY IMPROVEMENT IN RAPID PROTOTYPING MACHINE (FDM-1650)", 2001.

[36] U. M. Dilberoglu, S. Simsek, and U. Yaman, ScienceDirect Comprehensive Analysis of the Shrinkage Compensation Approach Proposed for the FDM process, vol. 00, pp. 19, 2018.

[37] N. Volpato, J. A. Foggiatto, and D. C. Schwarz, The influence of support base on FDM accuracy in Z, Rapid Prototyp. J., vol. 20, no. 3, pp. 182191, 2014.

[38] D. Ferri, A. Perolo, M. Nodari, C. Buonerba, S. A. Versalis, and V. G. Taliercio, Cross-WLF parameters to predict rheological properties of polylactic acid, vol. 25, 2017.

[39] Q. Sun, G. M. Rizvi, C. T. Bellehumeur, and P. Gu, Effect of processing conditions on the bonding quality of FDM polymer filaments, Rapid Prototyp. J., vol. 14, no. 2, pp. 7280, 2008.

[40] Georges M. Fadel and Chuck Kirschman, Accuracy issues in CAD to RP translations Rapid Prototyp. J., vol. 10, no. 1, pp. 56, 2004.

[41] R. Jones et al., RepRap the replicating rapid prototyper, Robotica, vol. 29, no. 1, pp. 177191, 2011.

[42] A. Bellini, S. Guceri, and M. Bertoldi, Liquefier Dynamics in Fused Deposition, J. Manuf. Sci. Eng., vol. 126, no. 2, p. 237, 2004.

[43] M. Bertoldi, M. A. Yardimci, C. M. Pistor, S. I. Guyeri, and G. Sala, Quantitative Mapping of Cerebral Blood Flow with Alternate Ascending / Descending Directional Navigation (ALADDIN), Knowl. Creat. Diffus. Util., vol. 20, p. 3492, 2012.

[44] O. Sigmund and S. Torquato, Composites with extremal thermal expansion coefficients, Appl. Phys. Lett., vol. 69, no. 21, pp. 32033205, 1996.

[45] S. O. and T. S., Design of materials with extreme thermal-expansion using a 3-phase topology optimization method, J. Mech. Phys. Solids, vol. 45, no. 6, pp. 10371067, 1997.

[46] D. Y. Chang and B. H. Huang, Studies on profile error and extruding aperture for the RP parts using the fused deposition modeling process, Int. J. Adv. Manuf. Technol., vol. 53, no. 912, pp. 10271037, 2011.

[47] S. Saqib and R. J. Urbanic, An Experimental Study to Determine Geometric and Dimensional Accuracy Impact Factors for Fused Deposition Modelled Parts Enabling Manuf. Compet. Econ. Sustain., no. February 2015, pp. 39, 2013.

[48] M. Mahesh, Y. S. Wong, J. Y. H. Fuh, and H. T. Loh, A Six-sigma approach for benchmarking of RPM processes, Int. J. Adv. Manuf. Technol., vol. 31, no. 34, pp. 374387, 2006.

[49] H. G. Lemu and S. Kurtovic, 3D Printing for Rapid Manufacturing :, pp. 470479, 2012.

[50] T. Brajlih, B. Valentan, J. Balic, and I. Drstvensek, Speed and accuracy evaluation of additive manufacturing machines, Rapid Prototyp. J., vol. 17, no. 1, pp. 6475, 2011.

[51] P. A. X. X. -, Investigation on Reasons Inducing Error and Measures Improving

Accuracy in Fused Deposition Modeling, Int. J. Adv. Inf. Sci. Serv. Sci., vol. 4, no. 5, pp. 149157, 2012.

[52] https://3dmakers.com.cy/products/ultimaker/ultimaker-3

[53] K. Cho, Soonja; Chemical Engineering, Inha University, Inchon 402-751, Rheological Properties of Polymers, vol. 1, no. 1, pp. 129, 2011.

[54] A. Frank, Viscoelasticity and dynamic mechanical testing A., TA Instruments, Appl. notes, vol. AN004, no. 1, pp. 13, 1993.

[55] A. M. Asiri, Improved Photochromic and Fatigue Performance furylethylidene) -succinicanhydride Doped in Polyurethane Thin Film, Polym. Eng. Sci., pp. 15, 2011.

[56] Moldflow Plastics Labs, Moldflow Material Testing Report MAT2238, NatureWorks LLC. pp. 134, 2007.

[57] A. Shakoor, R. Muhammad, N. L. Thomas, and V. V. Silberschmidt, Mechanical and thermal characterisation of poly (l-lactide) composites reinforced with hemp fibres, J. Phys. Conf. Ser., vol. 451, no. 1, 2013.

[58] Pilkington North America Inc., Properties of Soda-Lime Silica Float Glass, NSG Gr. Tech. Bull., pp. 13, 2013.

[59] https://www.azom.com/properties.aspx?ArticleID=89

[60] Q. Zhang, D. Yan, K. Zhang, and G. Hu, Pattern Transformation of Heat-Shrinkable Polymer by Three-Dimensional (3D) Printing Technique, Sci. Rep., vol. 5, pp. 2427, 2015.

[61] P. Database, The Universal Selection Source : Plastics Elastomers Young s Modulus How to calculate modulus of elasticity ? Factors Affecting Young s Modulus, 2012.

[62] C. Gershenson, Artificial Neural Networks for Beginners, arXiv, no. April, p. 8, 2013.

[63] T. Osswald and N. Rudolph, Polymer Rheology. Fundamentals and Applications, vol. 37. 2015.

[64] F. Wittel, "Mechanics of Building Materials", [??].

[65] I. S. Bayer, Thermomechanical properties of polylactic acid-graphene composites: A state-of-the-art review for biomedical applications, Materials (Basel)., vol. 10, no. 7, 2017.

[66] O. Yousefzade, J. Jeddi, E. Vazirinasab, and H. Garmabi, Poly(lactic acid) phase transitions in the presence of nano calcium carbonate: Opposing effect of nanofiller on static and dynamic measurements, J. Thermoplast. Compos. Mater., vol. 32, no. 3, pp. 312327, 2019.

[67] J. P. Mofokeng, A. S. Luyt, T. Tábi, and J. Kovács, Comparison of injection moulded, natural fibre-reinforced composites with PP and PLA as matrices, J. Thermoplast. Compos. Mater., vol. 25, no. 8, pp. 927948, 2012.

[68] A. Shakoor, R. Muhammad, N. L. Thomas, and V. V. Silberschmidt, Mechanical and thermal characterisation of poly (l-lactide) composites reinforced with hemp fibres, J. Phys. Conf. Ser., vol. 451, no. 1, 2013.

[69] Moldflow Plastics Labs, Moldflow Material Testing Report MAT2238, NatureWorks LLC, pp. 134, 2007.

[70] K. P. K. Golicha, DETERMINATION OF GLASS TRANSITION TEMPERATURE AND MODULUS OF PLA FILMS USING DYNAMIC MECHANICAL ANALYSIS AT 50oC AND AMPLITUDE OF 10 m, vol. 3, no. March, pp. 1219, 2014.

[71] Moldflow Plastics Labs, Moldflow Material Testing Report MAT2238, NatureWorks LLC, pp. 134, 2007.

[72] A. S. J. Suiker, Mechanical performance of wall structures in 3D printing processes: Theory, design tools and experiments, Int. J. Mech. Sci., vol. 137, no. January, pp. 145170, 2018.

[73] http : / / www . lboro . ac . uk / research / amrg / about / the7categoriesofadditivemanufacturing/

[74] U. Yaman, Shrinkage compensation of holes via shrinkage of interior structure

in FDM process, Int. J. Adv. Manuf. Technol., vol. 94, no. 58, pp. 21872197, 2018.

[75] https://all3dp.com/1/ultimaker-3-review/

[76] https://www.think3d.in/ultimaker-3-extended-review/

[77] https://ultimaker.com/en/resources/23111-print-core-installation

[78] https://ultimaker.com/en/products/ultimaker-3/specifications

[79] https://www.tomsguide.com/us/ultimaker-3-3d-printer,review-4131.html

[80] https://www.3dhubs.com/3d-printers/ultimaker-3-extended

[81] http://wiki.bk.tudelft.nl/toi-pedia/Getting_Started_with_Grasshopper

[82] https://fabrisonic.com/technology/

[83] Y. Muhuo, Dynamic Mechanical Properties and Thermal Stability of Poly(lactic Acid) and Poly(butylene Succinate) Blends Composites, J. Fiber Bioeng. Informatics, vol. 6, no. 1, pp. 8594, 2013.

[84] Y. S. Wong, Y. H. Fuh, H. T. Loh, and M. Mahesh, Rapid prototyping and manufacturing benchmarking, Sofwtare Solut. RP, vol. 1, pp. 5794, 2002.

[85] Y. Tang et al., Accuracy analysis and improvement for direct laser sintering (Singapore National University- MIT alliance), vol. 1, 2004.

[86] https://www.engineering.com/AdvancedManufacturing/ArticleID/15253/The-Age-of-Additive-Manufacturing.aspx

[87] E. Umaras and M. S. G. Tsuzuki, Additive Manufacturing - Considerations on Geometric Accuracy and Factors of Influence, IFAC-PapersOnLine, vol. 50, no. 1, pp. 1494014945, 2017.

[88] P. D. Paul A. Lagace, Effects of the environment, MIT notes, 2001.

[89] P. A. Kelly, Solid Mechanics: Viscoelasticity, p. 342, 2015.

[90] M. Fundamentals and M. A. Corporation, Accuracy and Calibration of Calipers, 2018.

[91] M. Fundamentals and M. A. Corporation, Accuracy and Calibration of Calipers. 2018.

[92] https://ecatalog.mitutoyo.com/